

UNCLASSIFIED

AD NUMBER
AD803695
NEW LIMITATION CHANGE
TO Approved for public release, distribution unlimited
FROM Distribution authorized to U.S. Gov't. agencies and their contractors; Administrative/Operational Use; NOV 1966. Other requests shall be referred to Air Force Weapons Laboratory, Attn: WLRP, Kirtland AFB, NM 87117.
AUTHORITY
AFWL ltr, 30 Nov 1971

THIS PAGE IS UNCLASSIFIED

AFWL-TR-65-136

AFWL-TR
65-136

803695



INVESTIGATION OF RESPONSE OF SIMPLIFIED ICBM-TYPE STRUCTURES TO IMPULSIVE LOADING

G. R. Abrahamson
A. L. Florence
H. E. Lindberg

Poulter Laboratories
Stanford Research Institute
Menlo Park, California
Contract AF29(601)-6360

TECHNICAL REPORT NO. AFWL-TR-65-136

November 1966

AIR FORCE WEAPONS LABORATORY
Research and Technology Division
Air Force Systems Command
Kirtland Air Force Base
New Mexico

AFWL-TR-65-136

INVESTIGATION OF RESPONSE OF SIMPLIFIED ICBM-TYPE
STRUCTURES TO IMPULSIVE LOADING

G. R. Abrahamson

A. L. Florence

H. E. Lindberg

Poulter Laboratories
Stanford Research Institute
Menlo Park, California
Contract AF29(601)-6360

TECHNICAL REPORT NO. AFWL-TR-65-136

This document is subject to special export controls and each transmittal to foreign governments or foreign nationals may be made only with prior approval of AFWL (WLRP), Kirtland AFB, N.M. Distribution of this document is limited because of the technology discussed.

FOREWORD

This report was prepared by Stanford Research Institute, Menlo Park, California, under Contract AF29(601)-6330. The research was performed under Program Element 7.60.06.01.D, Project 5710, Subtask 15.029, and was funded by the Defense Atomic Support Agency (DASA).

Inclusive dates of research were 16 March 1964 to 15 March 1965. The report was submitted 26 October 1966 by the AFWL Project Officer, Lt Walter D. Dittmer, (WLRP). Former Project Officer was Lt Richard C. Brightman, (WLRP).

Many members of the staff of Poulter Laboratories contributed to the work reported herein. M. Kanninen assisted on the work reported in Section 2. J. N. Goodier contributed the theory described in Section 3. R. Herbert performed the analysis in Section 4. Calculations for Sections 2 and 5 were carried out by B. Bain. L. Dary, L. Parker, and W. Zietzke assisted with the experimental work. These contributions, and those of the report production staff, are gratefully acknowledged.

This report has been reviewed and is approved.

Walter D. Dittmer

WALTER D. DITTMER
Lt, USAF
Project Officer

Edgar M. Munyon

EDGAR M. MUNYON
Colonel, USAF
Chief, Physics Branch

Claude K. Stambaugh

CLAUDE K. STAMBAUGH
Colonel, USAF
Chief, Research Division

ABSTRACT

Theoretical and experimental structural response investigations of space-vehicle-type structures under suddenly applied external surface loads are described. The simulation of a simultaneous impulsive load by a traveling load such as produced by an explosive is analyzed for the string and membrane. Three dynamic buckling problems are investigated: (1) dynamic plastic-flow buckling of flat plates due to in-plane flow, (2) dynamic elastic buckling of a thin cylindrical shell under axial impact, and (3) dynamic buckling of cylindrical shells of a strain-rate sensitive material. A scheme for correlating the results of structural response investigations concerned with dynamic failure loads of structures is presented and a brief review of available results is given.

This page intentionally left blank.

CONTENTS

1.	INTRODUCTION	1
2.	SIMULATION OF SIMULTANEOUS IMPULSIVE LOADS ON STRINGS AND MEMBRANES WITH EXPLOSIVES . . .	5
2.1	Introduction	5
2.2	String Theory	6
2.3	Membrane Theory	11
2.4	Conclusions	19
3.	DYNAMIC BUCKLING OF RECTANGULAR PLATES IN SUSTAINED PLASTIC COMPRESSIVE FLOW.	23
3.1	Introduction	23
3.2	Principal Features of the Problem	23
3.3	Adaptation of a Strain-Hardening Law	27
3.4	Equations of Motion	32
3.5	The Simply Supported Rectangular Plate	34
3.6	Comparison with Experiment	39
4.	DYNAMIC BUCKLING OF A THIN CYLINDRICAL SHELL UNDER AXIAL IMPACT.	51
4.1	Introduction	51
4.2	Response of the Normal Modes	53
4.3	Buckling from Random Imperfections	59
4.4	Experiments	65
5.	DYNAMIC BUCKLING OF A CYLINDRICAL SHELL OF A STRAIN-RATE SENSITIVE MATERIAL	77
5.1	Introduction	77
5.2	Dynamic Flow Buckling	78
5.3	Equations of Motion	80
5.4	Solution	81
5.5	Strain Reversal	83
5.6	Random Velocity Perturbations	84
5.7	Numerical Analysis and Experimental Results . . .	86
5.8	Experimental Techniques	94
5.9	Conclusions	97

CONTENTS (Concluded)

6.	CORRELATION OF STRUCTURAL RESPONSE INFORMATION	99
6.1	Introduction	99
6.2	Scheme for Correlating the Results of Structural Response Investigations	99
6.3	Correlation of the Results of Structural Response Investigations	104
6.4	Conclusions	107
7.	OTHER INVESTIGATIONS	109
7.1	Interaction of Shock Effects and Structural Effects	109
7.2	Prediction of Accelerations from Shock Loading. . .	110
	DISTRIBUTION	112

ILLUSTRATIONS

Fig. 2.1	String Problem	5
Fig. 2.2	Membrane Problem	6
Fig. 2.3	Velocities and Displacements of String	10
Fig. 2.4	Velocities and Displacements of Membrane	17
Fig. 2.5	Velocity Distribution on Membrane $\beta = V/c = 5$	18
Fig. 3.1	Notation	23
Fig. 3.2	1/16-Inch Wall by 5/8-Inch-Square Aluminum Tubing Buckled by Axial Impact with a Massive Steel Plate at the Indicated Velocities	39
Fig. 3.3	1/16-Inch Wall by 7/8-Inch-Square Aluminum Tubing Buckled by Axial Impact with a Massive Steel Plate at the Indicated Velocities	40
Fig. 3.4	1/16-Inch Wall by 5/8-Inch-Square Aluminum Tubing, with Two Opposite Corners Cut, Buckled by Axial Impact with a Massive Steel Plate at the Indicated Velocities	41
Fig. 3.5	1/16-Inch Wall by 7/8-Inch-Square Aluminum Tubing, with Two Opposite Corners Cut, Buckled by Axial Impact with a Massive Steel Plate at the Indicated Velocities	41
Fig. 3.6	1/16-Inch Wall by 5/8-Inch-Square Aluminum Tubing, with Four Corners Cut, Buckled by Axial Impact with a Massive Steel Plate at the Indicated Velocities	42
Fig. 3.7	1/16-Inch Wall by 7/8-Inch-Square Aluminum Tubing, with Four Corners Cut, Buckled by Axial Impact with a Massive Steel Plate at the Indicated Velocities	4

ILLUSTRATIONS (Continued)

Fig. 3.8	1/8-Inch Wall by 3/4-Inch-Square Aluminum Tubing Buckled by Axial Impact with a Massive Steel Plate at the Indicated Velocities	44
Fig. 3.9	1/8-Inch Wall by 1-Inch-Square Aluminum Tubing Buckled by Axial Impact with a Massive Steel Plate at the Indicated Velocities	45
Fig. 3.10	Stress-Strain Curve for Tubing Material (Aluminum 6063-T5)	48
Fig. 4.1	Coordinates and Shell Nomenclature	54
Fig. 4.2	Amplification Function g vs. Axial and Circum- ferential Wave Numbers α and β for $\sigma/\sigma_{cl}=2.5$. . .	58
Fig. 4.3	Growth of Maximum Amplification with Time	59
Fig. 4.4	Axial and Circumferential Mean Wavelengths vs. Time	64
Fig. 4.5	Experimental Arrangement	67
Fig. 4.6	Axially Impacted Cylindrical Shell (Time is from initial impact at lower end)	69
Fig. 4.7	Permanent Buckles from Axial Impact (Opposite end was free)	71
Fig. 4.8	Static Buckling of an Identical Shell	72
Fig. 4.9	Histogram of Observed Aspect Ratios	73
Fig. 4.10	Buckling with a Heavy Mass on Both Ends, $\sigma/\sigma_{cl} = 1.56$ at Initial Impact	74
Fig. 5.1	Typical Buckled Shape of Circular Cylindrical Shell of Fully Annealed 1015 Steel—Cylinder No. 1b. . .	77
Fig. 5.2	Idealized Stress, Strain-Rate Law.	79
Fig. 5.3	Notation. Element of Shell in Motion	80

ILLUSTRATIONS (Continued)

Fig. 5.4	Static Stress-Strain Diagram for Fully Annealed 1015 Steel	87
Fig. 5.5	Strain-Rate Laws	88
Fig. 5.6	Amplification Function for Cylinder 3a	90
Fig. 5.7	Amplification Function for Cylinder 4a	90
Fig. 5.8	Response of Cylinder 3a to White Noise Velocity Perturbations (a) Initial velocity perturbation, (b) Buckled form after 28 μ sec, (c) Buckled form after 42 μ sec, and (d) Buckled form after 56 μ sec	91
Fig. 5.9	Response of Cylinder 4a to White Noise Velocity Perturbations (a) Initial velocity perturbation, (b) Buckled form after 28.5 μ sec, (c) Buckled form after 42.75 μ sec, and (d) Buckled form after 57 μ sec	93
Fig. 5.10	Buckled Form of Cylinder 3a	94
Fig. 5.11	Buckled Form of Cylinder 4a	94
Fig. 5.12	Result of Harmonic Analysis on Cylinder 3a	95
Fig. 5.13	Result of Harmonic Analysis on Cylinder 4a	95
Fig. 5.14	Experimental Arrangement	96
Fig. 6.1	Amplitude-Impulse Diagram for a Linear Oscillator Loaded with a Rectangular Pulse	100
Fig. 6.2	Amplitude-Impulse Diagram for a One-Degree-of-Freedom System of a Rigid, Perfectly-Plastic Material	102
Fig. 6.3	Schematic Amplitude-Impulse Diagram for a Thin Cylindrical Shell Contained Within a Close-Fitting Sleeve Loaded on the Exterior	103

ILLUSTRATIONS (Concluded)

- Fig. 6.4 Schematic Amplitude-Impulse Diagram for Rectangular Pulses to Produce Cracking (from hoop tension) of a Thin Cylindrical Shell by Rebound from an Internal Mandrel 104
- Fig. 6.5 Bounding Curves on Suddenly Applied External Surface Loads of Smoothly Varying Distribution to Produce 10 Percent Deformation of a Cylindrical Shell 106

TABLES

Table 2.1	Membrane —Maximum and Minimum Values of y_t/v	19
Table 3.1	Observed Half-Wavelengths for 1/16-Inch-Thick Plates	46
Table 3.2	Observed Half-Wavelengths for 1/16-Inch-Thick Plates with One Free Edge	46
Table 3.3	Observed Half-Wavelengths for 1/16-Inch-Thick Plates with Two Free Edges	47
Table 3.4	Observed Half-Wavelengths for 1/8-Inch-Thick Plates	47
Table 3.5	Calculated Half-Wavelengths	49
Table 5.1	Theoretical and Experimental Results	89

AFWL-TR-65-136

This page intentionally left blank.

1. INTRODUCTION

The work covered in this report is an extension of that described in [1.1]^{*} and [1.2]. The specific motivation for the investigations is discussed in Volume I of [1.1].

The work reported here falls in three major parts: simulation of simultaneous loads by traveling loads, investigations of dynamic buckling of structures, and correlation of structural response information.

Simulation of simultaneous loads by traveling loads is of considerable interest because of the relative ease of using explosives to obtain impulsive loads. In Section 2, the response of the string and the membrane to traveling loads, as a function of load velocity, is investigated. It is found that detonation velocities are sufficiently high to give a good approximation to a simultaneous load.

Buckling has been found to be a significant response mode for space vehicles under suddenly applied external surface loads. In the past year three dynamic buckling problems have been investigated. These are reported in Sections 3, 4, and 5. Section 3 describes dynamic plastic-flow buckling of a plate due to in-plane flow. Section 4 describes dynamic elastic buckling of a thin cylindrical shell under axial impact. Section 5 describes dynamic buckling of a cylindrical shell of a strain-rate sensitive material.

Correlation of structural response information related to failure loads of space-vehicle-type structures is desirable to make

^{*}Numbers in brackets indicate the references listed at the end of each section.

the results more accessible and to indicate areas where additional work is required. In Section 6 it is shown that for dynamic loads, the amplitude-impulse plane is a convenient and meaningful way to present failure loads. Using this format, a brief summary of available results is given.

In Section 7 some comments are made on the separation of the response of space vehicles to suddenly applied surface loads into shock response and structural response, and on prediction of accelerations transmitted to internal components.

REFERENCES

- 1.1 Abrahamson, G. R. and A. L. Florence, "Investigation of Response of Simplified ICBM-Type Structures to Impulsive Loading (U)," Volumes I and II, AFSWC-TDR-62-94, Contract AF 29(601)-4329, November 1962 (SRD) and December 1962 (Unclassified).
- 1.2 Abrahamson, G. R., A. L. Florence and H. E. Lindberg, "Investigation of Response of Simplified ICBM-Type Structures to Impulsive Loading (U)," Stanford Research Institute Final Report, AFWL-TDR-64-22, Contract AF 29(601)-4329, July 1964.

AFWL-TR-65-136

This page intentionally left blank.

2. SIMULATION OF SIMULTANEOUS IMPULSIVE LOADS ON STRINGS AND MEMBRANES WITH EXPLOSIVES

2.1 INTRODUCTION

Explosives are a convenient means of simulating simultaneous impulsive loads on structures. The explosive imparts an impulse by means of a high-pressure pulse acting within a narrow reaction zone at the detonation front which travels over the surface away from the initiation point at the detonation velocity. Consequently, elements of the structure receive impulsive velocities successively and not simultaneously as desired. Good simulation of a simultaneously applied impulse over an area can be expected if the detonation velocity is sufficiently large, but some criterion is required to decide when this velocity is large enough.

In this section the responses of a stretched infinite string and a stretched infinite membrane to traveling concentrated forces representing a detonation front are investigated. The string has a concentrated force of magnitude $2P$ suddenly applied to it which is supposed to separate immediately into two equal forces of magnitude P and travel in opposite directions each at velocity V (Fig. 2.1). The

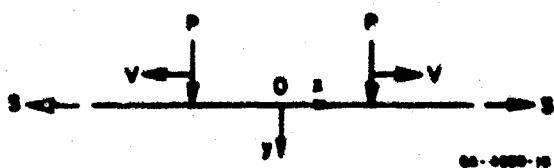


FIG. 2.1 STRING PROBLEM

membrane has applied to it a circular ring load of magnitude P per unit length the radius of which increases at a constant velocity V (Fig. 2.2). Of particular interest are the displacement and velocity distributions imparted to the string and

membrane when the loads are moving supersonically relative to the wave velocities. The velocity distributions are compared with the

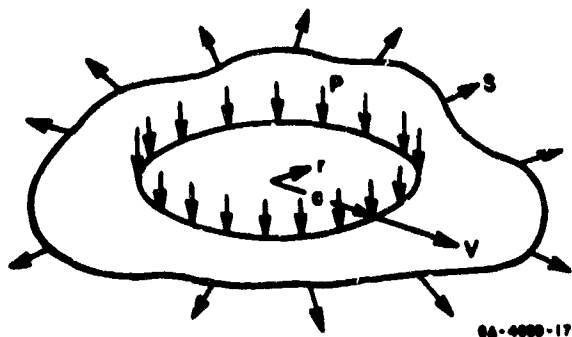


FIG. 2.2 MEMBRANE PROBLEM

constant velocity distribution resulting from the whole impulse being applied uniformly over the length or area traversed by the load.

Past studies originated with a treatment by Goodier [2.1] of a stretched semi-infinite string subjected to a concentrated force which runs on to it at the support and travels at a constant velocity.

It was shown that the velocity distribution approaches that due to an ideal impulse covering the portion of the string traversed by the load as the velocity of the force becomes large. Florence [2.2] treated the corresponding problem for the beam and included the problem corresponding to the string problem studied here. A similar conclusion was drawn but additionally the velocity distribution was found much more uniform when initiation was away from a fixed support. This permitted very uniform distributions of velocity with practical values of beam wave velocities and detonation velocities. Also, it was found desirable to have a detonation velocity supersonic relative to the beam wave velocities.

It is shown here that with central initiation and with practical values of wave and detonation velocities, a uniform velocity distribution on the string and membrane is achieved. Also, results are presented to describe the distributions.

2.2 STRING THEORY

Let the two constant loads P originate at time $t = 0$ at the origin $0(x, y)$ (Fig. 2.1) and separate, each with a constant velocity V . Let the string have mass m per unit length, be stretched by a force s and be at rest at time $t = 0$. Then the differential equation

of motion, the initial conditions, and boundary conditions are

$$\frac{\partial^2 y}{\partial x^2} - \frac{1}{c^2} \frac{\partial^2 y}{\partial t^2} = - \frac{P}{mc^2} \delta(x - Vt) \quad x > 0 \quad (2.1)$$

$$y(x, 0) = \frac{\partial y}{\partial t}(x, 0) = 0 \quad (2.2)$$

and

$$\frac{\partial y}{\partial x}(0, t) = 0 \quad \lim_{x \rightarrow \infty} y(x, t) = 0 \quad (2.3)$$

where $c = (s/m)^{1/2}$ is the string wave velocity, and δ is the Dirac delta function.

Applying the Laplace transformation to (2.1) and (2.3), and making use of (2.2) gives

$$\frac{d^2 \bar{y}}{dx^2} - (p/c)^2 \bar{y} = - \frac{P}{mc^2 V} e^{-px/V} \quad (2.4)$$

$$\frac{d\bar{y}}{dx}(0, p) = 0 \quad \lim_{x \rightarrow \infty} \bar{y}(x, p) = 0 \quad (2.5)$$

The solution of (2.4) satisfying (2.5) is

$$\bar{y}(x, p) = \frac{P}{m} \frac{1}{V^2 - c^2} (ce^{-px/c} - Ve^{-px/V}) \frac{1}{p^2} \quad (2.6)$$

Inverting the transform (2.6), noting that the only singularity is a simple pole at the origin of the p plane, yields

$$y(x, t) = \left\{ \begin{array}{ll} \frac{P}{m} \cdot \frac{(V-c)t}{V^2-c^2} & 0 < x < ct \\ \frac{P}{m} \cdot \frac{(Vt-x)}{V^2-c^2} & ct < x < Vt \\ 0 & Vt < x \end{array} \right\} \quad 0 < c < V \quad (2.7)$$

$$y(x, t) = \left\{ \begin{array}{ll} \frac{P}{m} \cdot \frac{(c-V)t}{c^2-V^2} & 0 < x < Vt \\ \frac{P}{m} \cdot \frac{(ct-x)}{c^2-V^2} & Vt < x < ct \\ 0 & ct < x \end{array} \right\} \quad 0 < V < c \quad (2.8)$$

From (2.7) and (2.8) the velocities are readily found to be

$$\frac{\partial y}{\partial t} = \left\{ \begin{array}{ll} \frac{P}{m} \cdot \frac{(V-c)}{V^2-c^2} & 0 < x < ct \\ \frac{P}{m} \cdot \frac{V}{V^2-c^2} & ct < x < Vt \\ 0 & Vt < x \end{array} \right\} \quad 0 < c < V \quad (2.9)$$

$$\frac{\partial y}{\partial t} = \left\{ \begin{array}{ll} \frac{P}{m} \cdot \frac{(c-V)}{c^2 - V^2} & 0 < x < Vt \\ \frac{P}{m} \cdot \frac{c}{c^2 - V^2} & Vt < x < ct \\ 0 & ct < x \end{array} \right\} \quad 0 < V < c \quad (2.10)$$

An isolated string element of length Δx with a force P traveling over it in a time Δt receives an impulse $P\Delta t$. Let the velocity acquired be v . Then the momentum acquired is $m\Delta x v = P\Delta t$. Since $\Delta t = \Delta x/V$, the velocity of the isolated element is $v = P/mV$. Hence the impulse delivered is P/V . If P increases proportionately with V , i.e., $P/V = I$ where I is a constant, a series of these elements will approximate a finite length of string subjected to an impulse I per unit length which imparts a velocity v . One requirement for good simulation is therefore that y_t/v should be approximately unit ($y_t = \partial y / \partial t$).

Figures 2.3(a) and 2.3(b) show the velocity and displacement distributions along the string according to (2.9) and (2.7) with $V = nc$ ($n > 1$). The force is moving supersonically relative to the string wave velocity. To illustrate the degree of simulation consider the value $n = 19$. From Fig. 2.3(a) it is seen that the normal velocity of the string over one-nineteenth of the distance traversed by the load is 5 percent less than that due to the same impulse uniformly distributed. Over the remaining distance it is about 0.3 percent greater.

Good simulation also requires small displacements. Figure 2.3(b) shows the displacements with a maximum of $y = vtn/(n+1)$ or $y/x = (v/V)n/(n+1) = y_t/V$ where x is the load position. Hence the

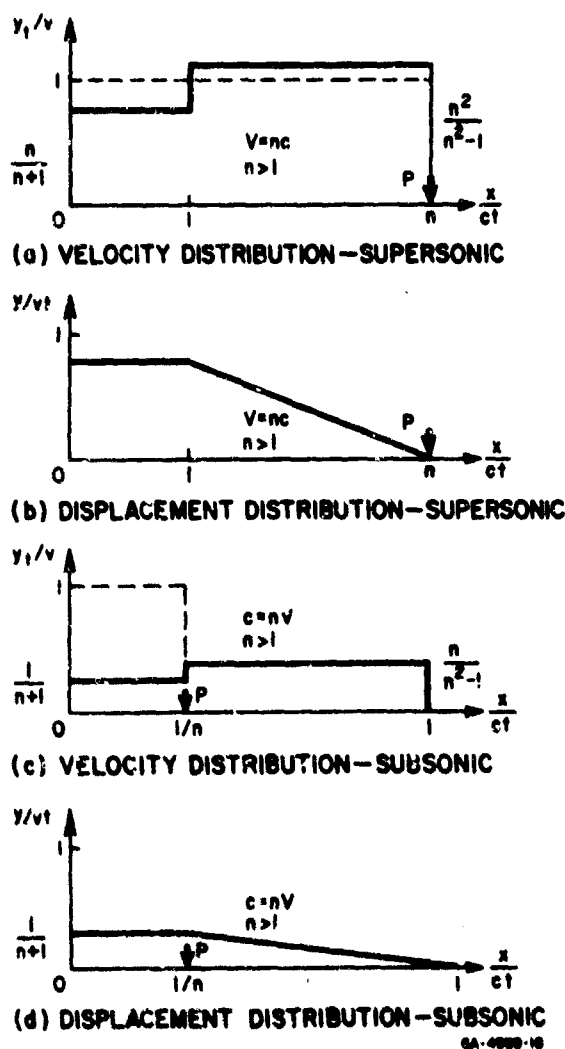


FIG. 2.3 VELOCITIES AND DISPLACEMENTS OF STRING

of $\epsilon = 0.08$ the ratio $v/V = 0.045$. Hence the maximum displacement is approximately $y = 0.045x$, where x is the load position, or about 5 percent of the distance traveled by the load. Using the sheet explosive FL 506D with a detonation velocity of 7 mm/ μ sec this relation becomes $y = 0.019x$ and $\beta_y \approx 20$.

ratio y_t/V or v/V should be small. In order to estimate reasonable values of the ratio v/V one can equate the kinetic energy imparted to the plastic work done, assuming this to be much larger than the elastic strain-energy capacity. If the final strain is ϵ , the yield stress is σ_y , and the cross-sectional area is A , the energy equation is $mv^2/2 = \sigma_y \epsilon A$. Now $m = \rho A$, and $c_y = (\sigma_y/\rho)^{1/2}$ is the maximum wave velocity of the string, ρ being the mass density. Thus $v = c_y \sqrt{2\epsilon}$ and $v/V = \sqrt{2\epsilon}/\beta_y$ where $\beta_y = V/c_y$. As a practical example consider an aluminum string stretched almost to yielding at $\sigma_y = 50,000$ lb/in². With a mass density $\rho = 0.00025$ lb-sec²/in⁴ the wave velocity is about $c_y = 0.355$ mm/ μ sec. As an example of an explosive with one of the slower detonation velocities, oxy-acetylene gas (50/50 mixture by volume) has $V = 3$ mm/ μ sec so that $\beta \approx 9$. Taking a large strain

Figures 2.3(c) and 2.3(d) show the velocity and displacement distributions along the string according to (2.10) and (2.8) with $c = nV$ ($n > 1$). For no value of n is the line $y_t/v = 1$ approximated for $0 \leq x/ct \leq 1/n$ so that simulation is not possible when the load moves subsonically relative to the string wave velocity.

2.3 MEMBRANE THEORY

An infinite stretched membrane is subjected to a ring load of magnitude P per unit length of circumference (Fig. 2.2). The radius of the ring increases at a constant velocity V . Choosing the origin of the radial coordinate r at the starting or detonation point when the time is $t = 0$, the equation of motion, initial conditions and boundary conditions are

$$\frac{\partial^2 y}{\partial r^2} + \frac{1}{r} \frac{\partial y}{\partial r} - \frac{1}{c^2} \frac{\partial^2 y}{\partial t^2} = \frac{P}{mc^2} \cdot \delta(r - Vt) \quad (2.11)$$

$$y(r, 0) = \frac{\partial y}{\partial t}(r, 0) = 0 \quad (2.12)$$

$$\frac{\partial y}{\partial r}(0, t) = 0 \quad \lim_{r \rightarrow \infty} y(r, t) = 0 \quad (2.13)$$

$$r \rightarrow \infty$$

where y is the deflection, m the mass per unit area of membrane and $c = (S/m)^{1/2}$ is the membrane wave velocity. S is the tension per unit edge length.

Let $\bar{y}(\lambda, t)$ be the Hankel transform of order zero of the function $y(r, t)$. Then applying such a transformation to Eqs. (2.11) and (2.12) gives, with the aid of (2.13)

$$\frac{d^2 \bar{y}}{dt^2} + c^2 \lambda^2 \bar{y} = \frac{PVt}{m} J_0(\lambda Vt) \quad (2.14)$$

$$\bar{y}(\lambda, 0) = \frac{d\bar{y}}{dt}(\lambda, 0) = 0 \quad (2.15)$$

The solution of Eq. (2.14) satisfying conditions (2.15) is

$$\bar{y}(\lambda, t) = \frac{PV}{mc\lambda} \int_0^t \eta \sin c\lambda (t-\eta) J_0(\lambda V\eta) d\eta \quad (2.16)$$

and the inverse Hankel transform of (2.16) is

$$y(r, t) = \frac{PV}{mc} \int_0^\infty J_0(r\lambda) \int_0^t \eta \sin c\lambda (t-\eta) J_0(\lambda V\eta) d\eta d\lambda \quad (2.17)$$

Reversing the order of integration in (2.17) and setting $x = ct\lambda$ ($dx = ctd\lambda$), $\mu = \eta/t$, $\alpha = r/ct$ and $\beta = V/c$ yields

$$z(\alpha, \beta) = \int_0^1 \mu d\mu \int_0^\infty J_0(\alpha x) J_0(\beta \mu x) \sin x (1-\mu) dx \quad (2.18)$$

with

$$z = ymc^2/PVt$$

In [2.3] may be found the following results:

$$\int_0^\infty J_0(ax) J_0(bx) \sin yx dx = \begin{cases} 0 & 0 < y < b-a \\ \frac{1}{2(ab)^{1/2}} P_{-1/2}(A) & b-a < y < b+a \\ \frac{1}{\pi(ab)^{1/2}} Q_{-1/2}(-A) & b+a < y < \infty \end{cases} \quad (2.19)$$

where $0 < a < b$ and

$$A = (b^2 + a^2 - y^2)/2ab \quad (2.20)$$

In (2.19) $P_{-1/2}$ and $Q_{-1/2}$ are associated Legendre functions of the first and second kind and they are related to complete elliptic integrals of the first kind through the following relations.

$$P_{-1/2}(A) = {}_2F_1(1/2, 1/2; 1; (1-A)/2) = 2/\pi K(\sqrt{(1-A)/2}) \quad -1 < A < 1$$

$$Q_{-1/2}(-A) = \pi/\sqrt{-2A} \cdot {}_2F_1(1/4, 3/4; 1; 1/A^2) = \quad (2.21)$$

$$\sqrt{2/(1-A)} K(\sqrt{2/(1-A)}) \quad -\infty < A < -1$$

where ${}_2F_1$ is a hypergeometric function.

Before applying the result (2.19) to evaluate (2.18) the latter should be rewritten in the form

$$z(\alpha, \beta) = \left[\int_0^{\alpha/\beta} \mu d\mu + \int_{\alpha/\beta}^1 \mu d\mu \right] \int_0^\infty J_0(\alpha x) J_0(\beta \mu x) \sin x (1-\mu) dx \quad (2.22)$$

In the first double integral of (2.22) $0 \leq \beta \mu \leq \alpha$, while in the second, $\alpha \leq \beta \mu \leq \beta$. Making use of the relation (2.21), the result (2.19) becomes

$$\int_0^\infty J_0(\alpha x) J_0(\beta \mu x) \sin(1-\mu)x dx = \begin{cases} 0 & \begin{cases} 0 < 1-\mu < \beta \mu - \alpha & 0 < \alpha < \beta \mu \\ 0 < 1-\mu < \alpha - \beta \mu & 0 < \beta \mu < \alpha \end{cases} \\ \frac{1}{\pi(\alpha \beta \mu)^{1/2}} K(k_1) & \begin{cases} \beta \mu - \alpha < 1-\mu < \beta \mu + \alpha & 0 < \alpha < \beta \mu \\ \alpha - \beta \mu < 1-\mu < \alpha + \beta \mu & 0 < \beta \mu < \alpha \end{cases} \\ \frac{1}{\pi(\alpha \beta \mu)^{1/2}} k_2 K(k_2) & \alpha + \beta \mu < 1-\mu < \infty \end{cases} \quad (2.23)$$

where the moduli of the complete elliptic integrals K are

$$k_1 = [(1-A)/2]^{1/2}$$

and

$$k_2 = [2(1-A)]^{1/2}$$

in which

$$A = [\alpha^2 + \beta^2 \mu^2 - (1-\mu)^2] / 2\alpha\beta\mu$$

from (2.20).

Substituting the appropriate result from (2.23) in the integrals (2.22) leads to the following results

$$1 < \alpha < \beta \quad \pi(\alpha\beta)^{1/2} z = I_1 \left(\frac{\alpha+1}{\beta+1} \right) - I_1 \left(\frac{\alpha-1}{\beta-1} \right)$$

$$\begin{matrix} 0 < \alpha < 1 < \beta \\ 0 < \alpha < \beta < 1 \end{matrix} \quad \pi(\alpha\beta)^{1/2} z = I_1 \left(\frac{1+\alpha}{1+\beta} \right) - I_1 \left(\frac{1-\alpha}{1+\beta} \right) + I_2 \left(\frac{1-\alpha}{1+\beta} \right) \quad (2.24)$$

$$0 < \beta < \alpha < 1 \quad \pi(\alpha\beta)^{1/2} z = I_1 \left(\frac{1-\alpha}{1-\beta} \right) - I_1 \left(\frac{1-\alpha}{1+\beta} \right) + I_2 \left(\frac{1-\alpha}{1+\beta} \right)$$

where

$$I_1(\mu) = \int_0^\mu \mu K(k_1) d\mu$$

$$I_2(\mu) = \int_0^\mu \mu k_2 K(k_2) d\mu$$

From the deflection expressions (2.24) the velocity distribution is readily obtained. In fact, differentiation of $y = PVt z/mc^2$ gives

$$\frac{\partial y}{\partial t} = \frac{PV}{mc^2} (z - \alpha \frac{\partial z}{\partial \alpha}) \quad (2.25)$$

and so expressions (2.24) have to be differentiated with respect to α . Singularities arise in this operation but are combined to be eliminated by considering all limiting processes in the Cauchy principal value sense. Substitution of (2.24) in (2.25) then yields the velocity distribution in the form

$$\begin{aligned} 1 < \alpha < \beta \quad \frac{mc^2}{PV} \frac{\partial y}{\partial t} &= \frac{3z}{2} - \frac{1}{\pi} \left(\frac{\alpha}{\beta} \right)^{1/2} \left[I_3 \left(\frac{\alpha+1}{\beta+1} \right) - I_3 \left(\frac{\alpha-1}{\beta-1} \right) + \frac{\pi(\alpha+1)^{1/2}}{2(\beta+1)^{3/2}} \right. \\ &\quad \left. - \frac{\pi(\alpha-1)^{1/2}}{2(\beta-1)^{3/2}} \right] \\ 0 < \alpha < 1 < \beta \quad \frac{mc^2}{PV} \frac{\partial y}{\partial t} &= \frac{3z}{2} - \frac{1}{\pi} \left(\frac{\alpha}{\beta} \right)^{1/2} \left[I_3 \left(\frac{1+\alpha}{1+\beta} \right) - I_3 \left(\frac{1-\alpha}{1+\beta} \right) + I_4 \left(\frac{1-\alpha}{1+\beta} \right) \right. \\ &\quad \left. + \frac{\pi(1+\alpha)^{1/2}}{2(1+\beta)^{3/2}} \right] \\ 0 < \beta < \alpha < 1 \quad \frac{mc^2}{PV} \frac{\partial y}{\partial t} &= \frac{3z}{2} - \frac{1}{\pi} \left(\frac{\alpha}{\beta} \right)^{1/2} \left[I_3 \left(\frac{1-\alpha}{1-\beta} \right) - I_3 \left(\frac{1-\alpha}{1+\beta} \right) + I_4 \left(\frac{1-\alpha}{1+\beta} \right) \right. \\ &\quad \left. - \frac{\pi(1-\alpha)^{1/2}}{2(1-\beta)^{3/2}} \right] \end{aligned} \quad (2.26)$$

where

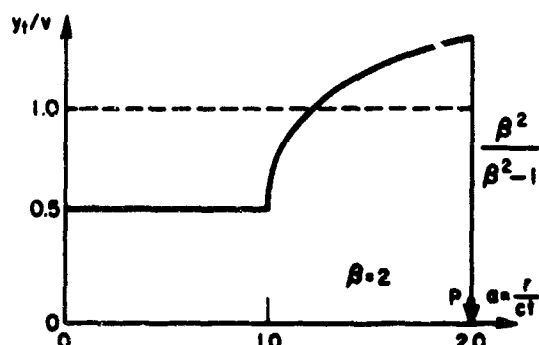
$$\begin{aligned} I_3(\mu) &= \int_0^\mu \mu \frac{\partial}{\partial \alpha} \{ K(k_1) \} d\mu \\ I_4(\mu) &= \int_0^\mu \mu \frac{\partial}{\partial \alpha} \{ k_2 K(k_2) \} d\mu \end{aligned}$$

It is of interest to give the velocity expressions for the center of the membrane since they can be obtained explicitly. Setting $r = 0$ in (2.17) and continuing the derivations as before leads to

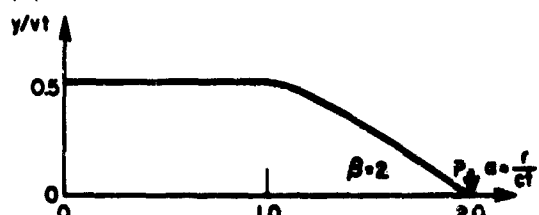
$$\frac{mc^2}{PV} \frac{\partial y}{\partial t}(0, t) = \begin{cases} [1 - \{\pi/2 - \sin^{-1}(1/\beta)\} / (\beta^2 - 1)^{1/2}] / (\beta^2 - 1) & \beta > 1 \\ 1/3 & \beta = 1 \\ [\{\cosh^{-1}(1/\beta)\} / (1 - \beta^2)^{1/2} - 1] / (1 - \beta^2) & \beta < 1 \end{cases} \quad (2.27)$$

Figures 2.4(a) and 2.4(b) show the velocity displacement distributions over the membrane according to (2.24) and (2.26) when the force is moving supersonically relative to the membrane wave velocity. The diagrams have been drawn for the case $V = 2c$ ($\beta = 2$) but the forms are similar for all the supersonic cases ($\beta > 1$); the higher the value of β , the flatter the velocity curve. Figure 2.5 shows the velocity for $\beta = 5$. As in the representation of velocity and displacement distributions for the string (Fig. 2.3) the velocity v used to render results dimensionless is the velocity that would be acquired by all the elements if they were disconnected from each other, that is, $v = P/mV$. Hence good simulation of impulse applied instantaneously over the circular area swept out by the detonation front is obtained if the curve y_t/v approximates the line $y_t/v = 1$ ($y_t = \partial y / \partial t$). Additionally, for good simulation the displacements acquired while the load is acting should be very small.

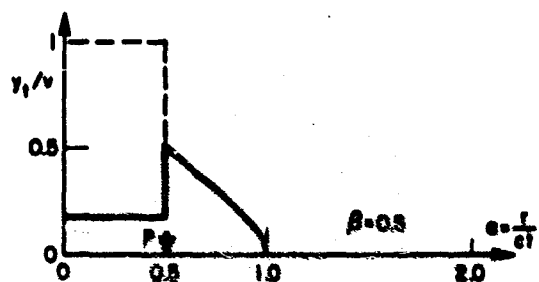
Figures 2.4(c) and 2.4(d) show the velocity and displacement distributions over the membrane according to (2.24) and (2.27) when the force is moving subsonically relative to the membrane wave velocity. The diagrams have been drawn for the case $V = c/2$ ($\beta = 1/2$) but the forms are similar for all the subsonic cases ($\beta < 1$). Because of the significant disturbances running ahead of the load, good simulation is never possible with subsonic loads. Figure 2.4(c) shows that the line $y_t/v = 1$ is not approximated.



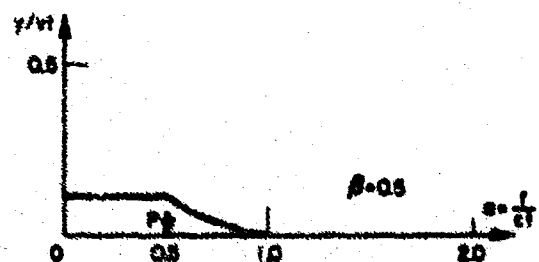
(a) VELOCITY DISTRIBUTION—SUPERSONIC



(b) DISPLACEMENT DISTRIBUTION—SUPERSONIC



(c) VELOCITY DISTRIBUTION—SUBSONIC



(d) DISPLACEMENT DISTRIBUTION—SUBSONIC

FIG. 2.4 VELOCITIES AND DISPLACEMENTS OF MEMBRANE

In all supersonic cases the maximum velocity occurs under the load at $r = Vt$ and the minimum velocity is the velocity in the region $0 < r < ct$. The maximum and minimum values of the ratio y_t/v are respectively

$$\beta^2 / (\beta^2 - 1)$$

and

$$\left[1 - \left\{ \pi/2 - \sin^{-1}(1/\beta) \right\} / (\beta^2 - 1)^{1/2} \right] \beta^2 / (\beta^2 - 1)$$

Table 2.1 lists values of y_t/v for several values of β and shows the extent of the simulation. Although the minimum values of y_t/v require high values of β before they approximate unity, the radius of the central portion of membrane moving at this velocity is $1/\beta$ times the radius of the loading circle.

As a practical example consider an aluminum membrane with a mass density $\rho = 0.00025$ lb-sec²/in⁴ stretched to a stress of $\sigma = 50,000$ lb/in². The wave velocity $c = (S/m)^{1/2} = (\sigma/\rho)^{1/2}$

is then about 14,000 in/sec or about 0.355 mm/ μ sec. The detonation velocities of oxyacetylene gas (50/50 mixture by volume) and sheet explosive EL 506D are approximately 3 mm/ μ sec and 7 mm/ μ sec

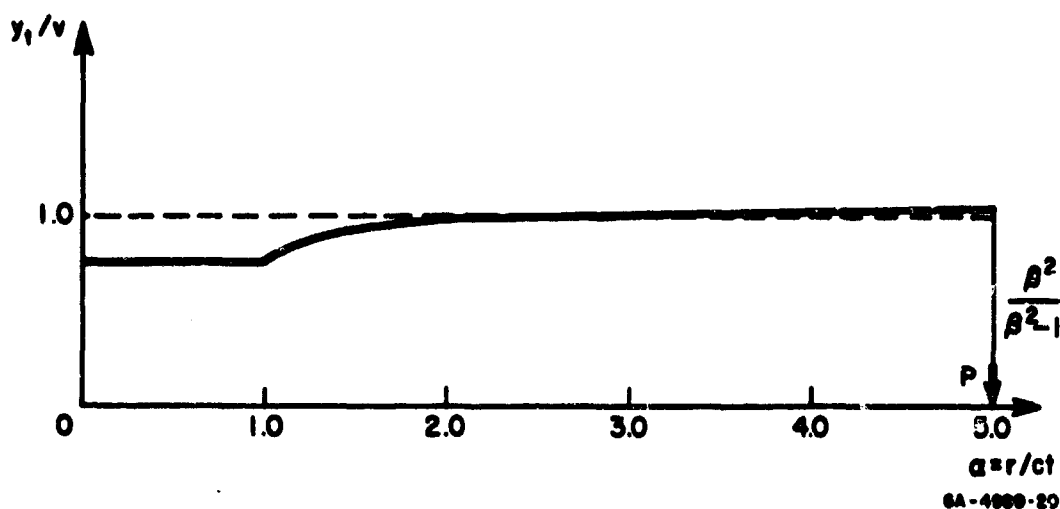


FIG. 2.5 VELOCITY DISTRIBUTION ON MEMBRANE $\beta = V/c = 5$

giving values for $\beta = V/c$ of about 9 and 20 respectively. From Table 2.1 the minimum values of y_t/v corresponding to $\beta = 10$ and 20 are low by about 14 percent and 7 percent, but exist only in central circles of radii 1/9th and 1/20th of the loading circle. The less the initial stretching of a membrane (or string) the higher is the value of β , for a given explosive, and hence the better is simulation.

To estimate the deflections which may exist while the load is still acting on the structure the initial kinetic energy is equated to the final plastic work, assuming the latter much greater than the elastic strain-energy capacity of the membrane. If each element has a final symmetric strain of ϵ , the yield stress is σ_y and the membrane depth is d , then the energy equation is approximately $mv^2/2 = 2\sigma_y \epsilon d$. Now $m = \rho d$, and $c_y = (\sigma_y/\rho)^{1/2}$ is the maximum wave velocity in the membrane, so $v = c_y \sqrt{4\epsilon}$ and $v/V = \sqrt{4\epsilon}/\beta_y$ where $\beta_y = V/c_y$. For a strain of 4 percent and $\beta_y = 9$ the ratio $v/V = 0.045$ so that, approximately, the deflection is $y = 0.045 r$ where r is the radius of the loading circle. The larger the value of β_y the smaller the initial deflections and hence the better the simulation.

Table 2.1
MEMBRANE—MAXIMUM AND MINIMUM VALUES OF y_t/v

$\beta = V/c$ $\beta > 1$	$(y_t/v)_{\max}$ $= \beta^2/(\beta^2-1)$ $\alpha = \beta$	$(y_t/v)_{\min}$ $0 < \alpha < 1$
2	1.333	0.527
5	1.042	0.751
10	1.010	0.861
20	1.003	0.926
50	1.000	0.969
100	"	0.985
200	"	0.992
500	"	0.997
1000	"	0.998

2.4 CONCLUSIONS

It can be concluded from the results of the above analyses for strings and membranes that, for good simulation of distributed impulses with explosives, the detonation velocities V must be greater than the wave velocities c . The higher the velocity ratio V/c , the better is the simulation. For both the string and membrane values of V/c greater than 20 give very uniform "initial" velocity distributions and, provided the required final plastic strains are not too large, gives small "initial" displacements. Values of V/c greater than 20 are certainly quite practical.

The actual uniformity of the initial velocity distribution can be seen in Fig. 2.3(a) for the string and in Table 2.1 (with aid of Figs. 2.4(a) and 2.5) for the membrane. Displacements of the string and membrane acquired during loading may be estimated by the

formulas $y = 2\epsilon x/\beta_y$ and $y = 4\epsilon r/\beta_y$ respectively where ϵ is the final strain, x and r are the load positions, and $\beta_y = V/c_y$ is the maximum wave velocity.

The results in [2.1] and [2.2] indicate that it is desirable to detonate explosives away from supports to minimize their influence while the load is being applied.

REFERENCES

- 2.1 Goodier, J. N., "Motion of a Stretched String Induced by a Traveling Force," Stanford Research Institute, Poulter Laboratories Internal Report No. 014-60, August 3, 1960.
- 2.2 Florence, A. L., "Traveling Force on a Timoshenko Beam," J. of Appl. Mech., June 1965, (Paper No. 64-WA/APM-26).
- 2.3 Erdelyi, A., Tables of Integral Transforms, Vol. 1, p. 102, McGraw-Hill Book Co., Inc., 1954.

AFWL-TR-65-136

This page intentionally left blank.

3. DYNAMIC BUCKLING OF RECTANGULAR PLATES IN SUSTAINED PLASTIC COMPRESSIVE FLOW

3.1 INTRODUCTION

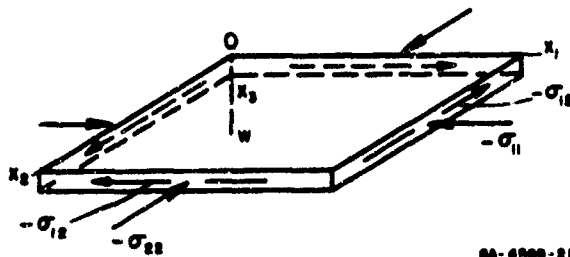
Dynamic buckling during sustained plastic flow has been described previously for cylindrical shells [3.1] under inward radial impulse and for rods under axial impact [3.2]. In this section an analysis is presented for rectangular plates under sustained in-plane flow, and the predicted wavelength is shown to be in reasonable agreement with experimental results.

3.2 PRINCIPAL FEATURES OF THE PROBLEM

A simple rectangular plate, flat or nearly so, is made to flow plastically for a short time by sufficiently large, uniform, in-plane stress, with three components σ_{11} , σ_{22} , σ_{12} (Fig. 3.1). There are non-zero plastic strain rates, related to the stress through the Prandtl-Reuss equations ([3.3], p 39)

$$\dot{\epsilon}_{11}^P = \dot{\lambda} \sigma'_{11}, \quad \dot{\epsilon}_{22}^P = \dot{\lambda} \sigma'_{22}, \quad \dot{\epsilon}_{12}^P = \dot{\lambda} \sigma'_{12} \quad (3.1)$$

elastic deformations being ignored. Primes denote deviatoric components throughout.



GA-4999-21

FIG. 3.1 NOTATION

While this in-plane flow is proceeding, there may also be small flexural motion in the transverse (x_3) direction, resulting in a plastically buckled form. This flexure alters the strain rates, except on the middle surface. But it is postulated that it does not cause reversal of strain-rate, so we are concerned with loading only, in the sense of plasticity theory. This is the type of flexural buckling envisaged by Shanley [3.4] for the column, and considered for the plate under uniaxial compression by Pearson [3.5].

In particular the transverse motion of the plate introduces differences between the strains, and strain rates, of a point on the upper face of the plate and the point below it on the lower face. Then the strain-increment vector of the flow rule is not the same for the two points, and in general the directions will be different. The representative points on the appropriate current yield surfaces must then be such that the normals are correspondingly different, implying a stress difference which can appear even if strain hardening is absent. This can not occur for the one-dimensional stress of the column. If there is no strain hardening, flexure of the column can occur without inducing bending moment. In the plate the stress-differences imply bending moments and also, in general, twisting moments.

The strain rate for a lower-face point may be expressed by $\dot{\epsilon}_{ij}^P + \Delta\dot{\epsilon}_{ij}^P$, and for the upper-face point by $\dot{\epsilon}_{ij}^P - \Delta\dot{\epsilon}_{ij}^P$. The plastic parameter is $\dot{\lambda}$ for the middle surface, but $\dot{\lambda} + \Delta\dot{\lambda}$ for the lower-face point and $\dot{\lambda} - \Delta\dot{\lambda}$ for the upper-face point. With a similar notation for stress, the Prandtl-Reuss equations for the lower face are

$$\dot{\epsilon}_{ij}^P + \Delta\dot{\epsilon}_{ij}^P = (\dot{\lambda} + \Delta\dot{\lambda})(\sigma'_{ij} + \Delta\sigma'_{ij})$$

and for the upper face are

(3.2)

$$\dot{\epsilon}_{ij}^P - \Delta\dot{\epsilon}_{ij}^P = (\dot{\lambda} - \Delta\dot{\lambda})(\sigma'_{ij} - \Delta\sigma'_{ij})$$

We take these for the in-plane directions only ($i, j = 1, 2$). Eliminating $\dot{\epsilon}_{ij}^P$ we have

$$2\Delta\dot{\epsilon}_{ij}^P = (\dot{\lambda} + \Delta\dot{\lambda})(\sigma'_{ij} + \Delta\sigma'_{ij}) - (\dot{\lambda} - \Delta\dot{\lambda})(\sigma'_{ij} - \Delta\sigma'_{ij})$$

The difference quantities however are to be small, corresponding to small flexure, which must prevail at least in the earlier stage of the motion of a nearly flat plate. These relations will accordingly be linearized to

$$\Delta\dot{\epsilon}_{ij}^P = \dot{\lambda}\Delta\sigma'_{ij} + \sigma'_{ij}\Delta\dot{\lambda}$$

Thus the relations consist of

$$\Delta\dot{\epsilon}_{11}^P = \dot{\lambda}\Delta\sigma'_{11} + \sigma'_{11}\Delta\dot{\lambda} \quad (3.3)$$

$$\Delta\dot{\epsilon}_{22}^P = \dot{\lambda}\Delta\sigma'_{22} + \sigma'_{22}\Delta\dot{\lambda} \quad (3.4)$$

$$\Delta\dot{\epsilon}_{12}^P = \dot{\lambda}\Delta\sigma'_{12} + \sigma'_{12}\Delta\dot{\lambda} \quad (3.5)$$

By elimination of $\Delta\dot{\lambda}$, (3.3) and (3.4) yield

$$\frac{\Delta\dot{\epsilon}_{11}^P}{\Delta\sigma'_{11}} - \frac{\Delta\dot{\epsilon}_{22}^P}{\Delta\sigma'_{22}} = \dot{\lambda} \left(\frac{\Delta\sigma'_{11}}{\sigma'_{11}} - \frac{\Delta\sigma'_{22}}{\sigma'_{22}} \right) \quad (3.6)$$

Adding (3.3) and (3.4), we obtain a symmetric equation. Combining this with (3.5) to eliminate $\Delta\dot{\lambda}$, we have

$$\frac{\Delta\dot{\epsilon}_{11}^P + \Delta\dot{\epsilon}_{22}^P}{\sigma'_{11} + \sigma'_{22}} - \frac{\Delta\dot{\epsilon}_{12}^P}{\sigma'_{12}} = \dot{\lambda} \left(\frac{\Delta\sigma'_{11} + \Delta\sigma'_{22}}{\sigma'_{11} + \sigma'_{22}} - \frac{\Delta\sigma'_{12}}{\sigma'_{12}} \right) \quad (3.7)$$

The unperturbed flow is regarded as given. This means that the strain rates in (3.1) are given, as well as the stress, and therefore $\dot{\lambda}$ is given. It will be evident that the effects of strain rates introduced by some buckling deflection $w(x_1, x_2, t)$ on strain-increment vector directions will differ according as the original strain rate is large or small. The original strain rate is therefore a necessary part of the specification of the state from which buckling occurs.

Now (3.6) and (3.7) provide two linear equations relating the unknown stress differences $\Delta\sigma'_{11}$, $\Delta\sigma'_{22}$, $\Delta\sigma'_{12}$, to the strain-rate differences $\Delta\dot{\epsilon}_{11}^P$, $\Delta\dot{\epsilon}_{22}^P$, $\Delta\dot{\epsilon}_{12}^P$.

In the next section we obtain a third linear equation from the strain-hardening law. The three equations will then play a part similar to that of moment-curvature relations in elastic plate theory. Combination with the equations of motion of the plate element then results in a differential equation for the deflection w alone.

Experimental results reported later in this paper, and interpreted by means of the present theory, are all such that the observable deformation is predominantly plastic. For this reason, and to minimize complications, we now assume that elastic deformation can be entirely neglected. Then the superscript p can be dropped in (3.1) through (3.7), and we can further write

$$\Delta\dot{\epsilon}_{11} = -\frac{h}{2} \frac{\partial^2 \dot{w}}{\partial x_1^2}, \quad \Delta\dot{\epsilon}_{22} = -\frac{h}{2} \frac{\partial^2 \dot{w}}{\partial x_2^2}, \quad \Delta\dot{\epsilon}_{12} = -\frac{h}{2} \frac{\partial^2 \dot{w}}{\partial x_1 \partial x_2} \quad (3.8)$$

If the plate is not initially flat, the initial ordinate of the mid-surface will be denoted by $w_0(x_1)$, and then w means the observable deflection, the additional ordinate, at time t .

3.3 ADAPTATION OF A STRAIN-HARDENING LAW

The strain-hardening law to be employed here is

$$\sigma = H \left(\int d\epsilon \right) \quad (3.9)$$

where

$$\sigma = \sqrt{\frac{3}{2} (\sigma'_{ij} \sigma'_{ij})} \quad , \quad d\epsilon = \sqrt{\frac{2}{3} (d\epsilon_{ij} d\epsilon_{ij})} \quad ; i, j = 1, 2, 3 \quad (3.10)$$

define the positive "equivalent stress" and "equivalent strain increment" corresponding to [3.3] p 26 Eq. (14), and p 30 Eq. (16), except that the present notation omits bars. The integral in (3.8) is path-dependent, and the strain paths are not the same for different elements of material on the same thickness line.

In the present problem we regard the transverse shear strains ϵ_{23} , ϵ_{31} as negligibly small, supposing that thickness lines remain normal to the middle surface and straight, as commonly done in thin plate and shell theory. Then, in view of plastic incompressibility, we can write from the second of (3.10),

$$(d\epsilon)^2 = \frac{4}{3} [(d\epsilon_{11})^2 + (d\epsilon_{22})^2 + d\epsilon_1 \cdot d\epsilon_2 + (d\epsilon_{12})^2] \quad (3.11)$$

The differentials in (3.10) are now taken specifically as those pertinent to the midsurface, and occurring in a time increment dt .

For the lower surface the corresponding strain increments are

$$d\epsilon_{11} = \frac{h}{2} \dot{\kappa}_{11} dt \quad , \quad d\epsilon_{22} = \frac{h}{2} \dot{\kappa}_{22} dt \quad , \quad d\epsilon_{12} = \frac{h}{2} \dot{\kappa}_{12} dt \quad (3.12)$$

where

$$\dot{\kappa}_{11} = \partial^2 \dot{w} / \partial x_1^2 \quad , \quad \dot{\kappa}_{22} = \partial^2 \dot{w} / \partial x_2^2 \quad , \quad \dot{\kappa}_{12} = \partial^2 \dot{w} / \partial x_1 \partial x_2 \quad (3.13)$$

Writing $d\epsilon_l$ for the equivalent strain increment at the lower surface, we may evaluate $(d\epsilon_l)^2$ from (3.11) by introducing the replacements (3.12).

We have already, in deriving (3.3), (3.4) and (3.5), treated the difference terms introduced by the flexure as small in comparison with the terms of the dominating flow. Correspondingly in (3.12) the flexural w terms will be supposed small compared with the midsurface terms. Then the squares and products from (3.12) can be linearized with respect to w . We find

$$(d\epsilon_l)^2 = (d\epsilon)^2 - \frac{4}{3}h dt \left[d\epsilon_{11}(\dot{\kappa}_{11} + \frac{1}{2}\dot{\kappa}_{22}) + d\epsilon_{22}(\dot{\kappa}_{22} + \frac{1}{2}\dot{\kappa}_{11}) + d\epsilon_{12}\dot{\kappa}_{12} \right] \quad (3.14)$$

For the upper surface $(d\epsilon_u)^2$ is obtained by changing the $-$ to $+$.

We apply the law (3.9) separately to the lower and the upper surfaces, and wish to obtain the difference

$$2\Delta\epsilon = \int d\epsilon_l - \int d\epsilon_u \quad (3.15)$$

which defines $\Delta\epsilon$. From (3.14) and the companion expression for $(d\epsilon_u)^2$, we have

$$\begin{aligned} (d\epsilon_l)^2 - (d\epsilon_u)^2 &= (d\epsilon_l + d\epsilon_u)(d\epsilon_l - d\epsilon_u) \\ &= -\frac{8}{3}h dt \left[d\epsilon_{11}(\dot{\kappa}_{11} + \frac{1}{2}\dot{\kappa}_{22}) + \dots \right] \end{aligned} \quad (3.16)$$

But

$$d\epsilon_l + d\epsilon_u = 2d\epsilon \quad (3.17)$$

Introducing this in (3.16), and converting to rates by inserting dt as required, we find

$$d\epsilon_l - d\epsilon_u = -\frac{4}{3}h dt \cdot \frac{1}{\dot{\epsilon}} \left[\dot{\epsilon}_{11}(\dot{\kappa}_{11} + \frac{1}{2}\dot{\kappa}_{22}) + \dot{\epsilon}_{22}(\dot{\kappa}_{22} + \frac{1}{2}\dot{\kappa}_{11}) + \dot{\epsilon}_{12}\dot{\kappa}_{12} \right] \quad (3.18)$$

and now (3.15) can be written as

$$\Delta\epsilon = -\frac{2}{3}h \int_0^t \frac{1}{\dot{\epsilon}} \left[\dot{\epsilon}_{11}(\dot{\kappa}_{11} + \frac{1}{2}\dot{\kappa}_{22}) + \dot{\epsilon}_{22}(\dot{\kappa}_{22} + \frac{1}{2}\dot{\kappa}_{11}) + \dot{\epsilon}_{12}\dot{\kappa}_{12} \right] dt \quad (3.19)$$

This becomes much simpler if the ratios $\dot{\epsilon}_{11}/\dot{\epsilon}$, $\dot{\epsilon}_{22}/\dot{\epsilon}$, $\dot{\epsilon}_{12}/\dot{\epsilon}$, pertaining to the midsurface flow, are independent of t throughout the motion. In general the Levy-Mises relations, to which (3.1) now reduce, imply

$$\frac{\dot{\epsilon}_{ij}}{\dot{\epsilon}} = \frac{3\sigma'_{ij}}{2\sigma} \quad (3.20)$$

We now suppose that the imposed stress components σ_{11} , σ_{22} are maintained in constant ratio throughout the motion. This implies constancy of the right-hand side of (3.20). Then the ratios $\dot{\epsilon}_{11}/\dot{\epsilon}$ etc. in (3.19) are in fact constants, and the integration can be effected by removing the dots on the κ 's. Thus (3.19) becomes

$$\Delta\epsilon = -h \left[\alpha(\kappa_{11} + \frac{1}{2}\kappa_{22}) + \beta(\kappa_{22} + \frac{1}{2}\kappa_{11}) + \gamma\kappa_{12} \right] \quad (3.21)$$

where

$$\alpha = \frac{2\dot{\epsilon}_{11}}{3\dot{\epsilon}} = \frac{\sigma'_{11}}{\sigma}; \quad \beta = \frac{2\dot{\epsilon}_{22}}{3\dot{\epsilon}} = \frac{\sigma'_{22}}{\sigma}; \quad \gamma = \frac{2\dot{\epsilon}_{12}}{3\dot{\epsilon}} = \frac{\sigma'_{12}}{\sigma}; \quad (3.22)$$

$$\kappa_{11} = \partial^2 w / \partial x_1^2, \text{ etc.}$$

and

$$\sigma = \sqrt{(\sigma_{11}^2 + \sigma_{22}^2 - \sigma_{11}\sigma_{22} + \frac{3}{2}\sigma_{12}^2)} \quad (3.23)$$

The quantity $2\Delta\epsilon$, expressed by (3.21) in terms of w , shows how much further along the equivalent-stress--equivalent-strain curve (3.9) the point for the lower surface is in advance of the point for the upper surface. The difference in the values of σ for the two surfaces is given by the differential form of (3.9),

$$2\Delta\sigma = 2H' \Delta\epsilon \quad (3.24)$$

and we shall take H' to be constant.

Again with reference to the experimental results we seek to explain, and for brevity, we now restrict the analysis to the case $\sigma_{12} = 0$. Then the first of (3.10) yields

$$2\sigma \Delta\sigma = (2\sigma_{11} - \sigma_{22})\Delta\sigma_{11} + (2\sigma_{22} - \sigma_{11})\Delta\sigma_{22} \quad (3.25)$$

Now (3.24) becomes, with (3.25) and (3.21)

$$\begin{aligned} (2\sigma_{11} - \sigma_{22})\Delta\sigma_{11} + (2\sigma_{22} - \sigma_{11})\Delta\sigma_{22} = -2H' \sigma h \left[\alpha \left(\kappa_{11} + \frac{1}{2} \kappa_{22} \right) \right. \\ \left. + \beta \left(\kappa_{22} + \frac{1}{2} \kappa_{11} \right) \right] \end{aligned} \quad (3.26)$$

This, and (3.6) (3.7), form a set of three equations, which are linear relations between the stress differences $\Delta\sigma_{11}$, $\Delta\sigma_{22}$, $\Delta\sigma_{12}$, and the derivatives of w [in view of (3.8)].

Since we contemplate small stress differences occupying only a small segment of the line represented by (3.9), and there is no unloading, the variation of stress through the thickness may be taken as linear. Then the moments per unit run M_{11} , M_{22} , M_{12} are given by

$$h^2 \Delta\sigma_{11} = 6M_{11} \quad , \quad h^2 \Delta\sigma_{22} = 6M_{22} \quad , \quad h^2 \Delta\sigma_{12} = 6M_{12} \quad (3.27)$$

We rewrite (3.6), (3.7) and (3.26) using these, and (3.8). Then (3.6) becomes

$$M_{12} = -\frac{h^3}{12\dot{\lambda}} \dot{\kappa}_{12} \quad (3.28)$$

(3.7) becomes

$$\sigma_{22}M_{11} - \sigma_{11}M_{22} = -\frac{h^3}{12\dot{\lambda}} [(2\sigma_{22} - \sigma_{11})\dot{\kappa}_{11} - (2\sigma_{11} - \sigma_{22})\dot{\kappa}_{22}] \quad (3.29)$$

and (3.26) becomes

$$(2\sigma_{11} - \sigma_{22})M_{11} + (2\sigma_{22} - \sigma_{11})M_{22} = -\frac{1}{3}H'\sigma h^3 [\alpha(\kappa_{11} + \frac{1}{2}\kappa_{22}) + \beta(\kappa_{22} + \frac{1}{2}\kappa_{11})] \quad (3.30)$$

In (3.30) we can put $H' = 0$ for a perfectly plastic material, and still obtain non-zero M_{11} , M_{22} from (3.29) and (3.30). These represent the stress differences induced by movement of the stress points on the now unchanging yield surface, referred to in Section 3.1, and depending on the curvature rates.

The solutions of (3.29), (3.30), for M_{11} , M_{22} , are

$$\begin{bmatrix} M_{11} \\ M_{22} \end{bmatrix} = -\frac{h^3}{24\dot{\lambda}\sigma} [(2\sigma_{22} - \sigma_{11})\dot{\kappa}_{11} - (2\sigma_{11} - \sigma_{22})\dot{\kappa}_{22}] \begin{bmatrix} (2\sigma_{22} - \sigma_{11}) \\ (2\sigma_{11} - \sigma_{22}) \end{bmatrix} - \frac{H'h^3}{6\sigma} [\alpha(\kappa_{11} + \frac{1}{2}\kappa_{22}) + \beta(\kappa_{22} + \frac{1}{2}\kappa_{11})] \begin{bmatrix} \sigma_{11} \\ \sigma_{22} \end{bmatrix} \quad (3.31)$$

We shall refer to the terms of the 1st line, having the factor $1/\dot{\lambda}$, as the "directional" moments, and to the terms of the 2nd line, proportional to H' , as the strain-hardening moments.

3.4 EQUATIONS OF MOTION

A plate element $dx dy$ is subjected to uniform stress σ_{11} , σ_{22} , together with the moments M_{11} , M_{22} , M_{12} , and transverse shear forces per unit run Q_1 , Q_2 necessarily associated with these. We neglect rotary inertia. The equations of motion take the well-known forms of plate theory

$$\frac{\partial Q_1}{\partial x_1} + \frac{\partial Q_2}{\partial x_2} + \sigma_{11} h \frac{\partial^2 w}{\partial x_1^2} + \sigma_{22} h \frac{\partial^2 w}{\partial x_2^2} = \rho h \frac{\partial^2 w}{\partial t^2}$$

$$Q_1 = \frac{\partial M_{11}}{\partial x_1} + \frac{\partial M_{12}}{\partial x_2} \quad Q_2 = \frac{\partial M_{22}}{\partial x_2} + \frac{\partial M_{12}}{\partial x_1}$$

where ρ means density.

By elimination of Q_1 , Q_2

$$\frac{\partial^2 M_{11}}{\partial x_1^2} + 2 \frac{\partial^2 M_{12}}{\partial x_1 \partial x_2} + \frac{\partial^2 M_{22}}{\partial x_2^2} + \sigma_{11} h \frac{\partial^2 (w + w_0)}{\partial x_1^2} + \sigma_{22} h \frac{\partial^2 (w + w_0)}{\partial x_2^2} = \rho h \frac{\partial^2 w}{\partial t^2} \quad (3.32)$$

In this we now use (3.31) for M_{11} , M_{22} , (3.28) for M_{12} , and convert it to a differential equation for w alone to obtain

$$\frac{h^2}{24\lambda} \left\{ \left(\frac{2\sigma_{22} - \sigma_{11}}{\sigma} \right)^2 \frac{\partial^5 w}{\partial t \partial x_1^4} + \left(\frac{2\sigma_{11} - \sigma_{22}}{\sigma} \right)^2 \frac{\partial^5 w}{\partial t \partial x_2^4} - \left[2 \frac{(2\sigma_{11} - \sigma_{22})(2\sigma_{22} - \sigma_{11})}{\sigma^2} \right. \right.$$

$$\left. - 4 \right] \frac{\partial^5 w}{\partial t \partial x_1^2 \partial x_2^2} \Big\} + \frac{h^2 H'}{6} \left\{ \frac{\sigma_{11}}{\sigma} \left(\alpha + \frac{1}{2} \beta \right) \frac{\partial^4 w}{\partial x_1^4} + \frac{\sigma_{22}}{\sigma} \left(\beta + \frac{1}{2} \alpha \right) \frac{\partial^4 w}{\partial x_2^4} \right.$$

$$\left. + \left[\frac{\sigma_{11}}{\sigma} \left(\beta + \frac{1}{2} \alpha \right) + \frac{\sigma_{22}}{\sigma} \left(\alpha + \frac{1}{2} \beta \right) \right] \frac{\partial^4 w}{\partial x_1^2 \partial x_2^2} \right\} - \sigma_{11} \frac{\partial^2 (w + w_0)}{\partial x_1^2} - \sigma_{22} \frac{\partial^2 (w + w_0)}{\partial x_2^2}$$

$$= -\rho \frac{\partial^2 w}{\partial t^2} \quad (3.33)$$

All the coefficients are constants, except for $\dot{\lambda}$ in the first line. As we have observed in Section 3.1, $\dot{\lambda}$ must be specified, and this is equivalent to specifying imposed strain rates $\dot{\epsilon}_{11}$, $\dot{\epsilon}_{22}$ as well as imposed stresses σ_{11} , σ_{22} . Since we have postulated slight strain hardening, it is reasonable to treat σ_{11} , σ_{22} as constant throughout the flow. We now postulate further that the imposed strain rates are to be constant, and therefore $\dot{\lambda}$ will also be constant. Now (3.32) is a linear equation with constant coefficients. The solution for a rectangular plate with simply supported edges is examined in Section 3.5 below.

Since from (3.22)

$$\frac{\sigma_{11}}{\sigma} = 2\alpha + \beta, \quad \frac{\sigma_{22}}{\sigma} = \alpha + 2\beta$$

we can rewrite (3.33) as

$$\begin{aligned} \frac{h^2}{24\lambda} \left\{ \left(\frac{2\sigma_{22} - \sigma_{11}}{\sigma} \right)^2 \frac{\partial^5 w}{\partial t \partial x_1^4} + \left(\frac{2\sigma_{11} - \sigma_{22}}{\sigma} \right)^2 \frac{\partial^5 w}{\partial t \partial x_2^4} - \left[\frac{2}{\sigma^2} (2\sigma_{11} - \sigma_{22})(2\sigma_{22} - \sigma_{11}) \right] \right. \\ \left. - 4 \left[\frac{\partial^5 w}{\partial t \partial x_1^2 \partial x_2^2} \right] \right\} + \frac{h^2 H'}{12} \left\{ \frac{\sigma_{11}^2}{\sigma^2} \frac{\partial^4 w}{\partial x_1^4} + \frac{\sigma_{22}^2}{\sigma^2} \frac{\partial^4 w}{\partial x_2^4} + 2 \frac{\sigma_{11} \sigma_{22}}{\sigma^2} \frac{\partial^4 w}{\partial x_1^2 \partial x_2^2} \right\} \\ - \sigma_{11} \frac{\partial^2 w}{\partial x_1^2} - \sigma_{22} \frac{\partial^2 w}{\partial x_2^2} + \rho \frac{\partial^2 w}{\partial t^2} = \sigma_{11} \frac{\partial^2 w_0}{\partial x_1^2} + \sigma_{22} \frac{\partial^2 w_0}{\partial x_2^2} \quad (3.34) \end{aligned}$$

If the compressive flow and the buckling are occurring slowly, the inertia term may be negligible. But it is not evident that the first line of terms may be dropped, since $\dot{\lambda}$ appears in the denominator and is small for a small flow rate. The magnitudes of the time derivatives of w will evidently depend on the initial displacement and velocity.

3.5 THE SIMPLY SUPPORTED RECTANGULAR PLATE

We take $\sigma_{11} = -\sigma_0$, $\sigma_{22} = 0$, corresponding to uniaxial compressive flow. Then $\sigma^2 = \sigma_{11}^2$. The differential equation (3.34) reduces to

$$\begin{aligned} & \frac{h^2}{24\lambda} \frac{\partial^5 w}{\partial t \partial x_1^4} + 4 \frac{\partial^5 w}{\partial t \partial x_2^4} + 8 \frac{\partial^5 w}{\partial t \partial x_1^2 \partial x_2^2} \\ & + \frac{1}{12} h^2 H' \frac{\partial^2 w}{\partial x_1^4} + \sigma_0 \frac{\partial^2 w}{\partial x_1^2} + \rho \frac{\partial^2 w}{\partial t^2} = -\sigma_0 \frac{\partial^2 w_0}{\partial x_1^2} \end{aligned} \quad (3.35)$$

If

$$w_0 = \sum \sum a_{mn} \sin \frac{m\pi x_1}{a} \sin \frac{n\pi x_2}{b} \quad (3.36)$$

we may take

$$w = \sum \sum W_{mn}(t) \sin \frac{m\pi x_1}{a} \sin \frac{n\pi x_2}{b} \quad (3.37)$$

This makes M_{11} , M_{22} in (3.31) zero at the edges $x_1 = 0, a$; $x_2 = 0, b$, so the edges are simply supported. Then (3.35) requires

$$\begin{aligned} & \frac{h^2}{12\lambda} \left[\left(\frac{m\pi}{a} \right)^4 + 4 \left(\frac{n\pi}{b} \right)^4 + 8 \left(\frac{m\pi}{a} \right)^2 \left(\frac{n\pi}{b} \right)^2 \right] \dot{W}_{mn} \\ & + \left(\frac{m\pi}{a} \right)^2 \left[\frac{1}{12} h^2 H' \left(\frac{m\pi}{a} \right)^2 - \sigma_0 \right] W_{mn} + \rho \ddot{W}_{mn} = \sigma_0 a_{mn} \left(\frac{m\pi}{a} \right)^2 \end{aligned} \quad (3.38)$$

For suitably limited initial deflection w_0 and velocity $\dot{w}(x_1, x_2, 0)$ the time derivatives of W_{mn} can be very small. These would be the

circumstances of a "static" test with σ_o increasing rather slowly to a critical value. The result

$$W_{mn} = \frac{\sigma_o a_{mn}}{\frac{1}{12} h^2 H' \left(\frac{m\pi}{a} \right)^2 - \sigma_o} \quad (3.39)$$

then indicates a critical compressive stress

$$\sigma_o = \frac{1}{12} h^2 H' \left(\frac{m\pi}{a} \right)^2 \quad (3.40)$$

It is remarkable that this is independent of b/n , the half-wavelength in the direction transverse to the load. For $m = 1$ it is the simple tangent modulus formula.

The same critical condition is obtained from (3.35) if we take w in the form

$$w = W_m \sin \frac{m\pi x_1}{a} \quad (3.41)$$

i.e., independent of x_2 .

Since $\sigma_{22} = 0$, the value of M_{22} given by (3.30) consists of the directional part only, and is therefore very small in the "static" test, for (3.37) or for (3.41).

Returning to the dynamical problem of the simply supported plate with the deflection (3.36), we suppose that the imposed strain rate $\dot{\epsilon}_{11}$ is large compared with any additional strain rates introduced by w . Then the directional moments in (3.31) could be neglected compared with the strain-hardening moments. The first line of (3.34), and that of (3.38), disappear.

Considering an imposed σ_0 much larger than the statical critical value (3.39), we shall have (3.38) in the form

$$\ddot{W}_{mn} - \frac{1}{\rho} \left(\frac{m\pi}{a} \right)^2 \left[\sigma_0 - \frac{1}{12} h^2 H' \left(\frac{m\pi}{a} \right)^2 \right] W_{mn} = \frac{\sigma_0}{\rho} a_{mn} \left(\frac{m\pi}{a} \right)^2 \quad (3.42)$$

It is convenient now to change to a dimensionless deflection coefficient w_{mn} , a dimensionless time τ , and to introduce a dimensionless constant s^2 , defined by

$$w_{mn} = \frac{W_{mn}}{h}, \quad \tau = \frac{\pi^2 h}{a^2} \sqrt{\frac{H'}{12\rho}} \cdot t, \quad s^2 = \frac{12\sigma_0 a^2}{\pi^2 H' h^2} \quad (3.43)$$

Then (3.42) becomes

$$\frac{d^2 w_{mn}}{d\tau^2} - m^2 (s^2 - m^2) w_{mn} = s^2 m^2 \frac{a_{mn}}{h} \quad (3.44)$$

For $m < s$ the solution will contain hyperbolic functions of time which may become large during the motion.

For a plate initially perfectly flat we have $a_{mn} = 0$, and any deflection is due to initial lateral velocity. Then if

$$w(x_1, x_2, 0) = 0, \quad \frac{1}{h} w_\tau(x_1, x_2, 0) = v_0 \sum \sum \beta_{mn} \sin \frac{m\pi x_1}{a} \sin \frac{n\pi x_2}{b} \quad (3.45)$$

the result obtained after integrating (3.44) is

$$\begin{aligned} \frac{1}{h} w(x_1, x_2, t) = v_0 \left\{ \sum_{n=1}^{\infty} \sum_{m=1}^r \frac{1}{p_m} \beta_{inn} \sinh p_m \tau \cdot \sin \frac{m\pi x_1}{a} \cdot \sin \frac{n\pi x_2}{b} \right. \\ \left. + \sum_{n=1}^{\infty} \sum_{m=1}^r \frac{1}{p_m} \beta_{mn} \sin p_m \tau \cdot \sin \frac{m\pi x_1}{a} \cdot \sin \frac{n\pi x_2}{b} \right\} \quad (3.46) \end{aligned}$$

where

$$p_m > 0, \quad p_m^2 = |m^2 (s^2 - m^2)|, \quad r < s < r+1 \quad (3.47)$$

This shows that the series for the deflection at time t is obtained from the series in (3.45) for the initial velocity by applying to each coefficient a magnification factor (but for a constant) which is either $p_m^{-1} \sinh p_m \tau$ or $p_m^{-1} \sin p_m \tau$, the former being potentially the greater. Examining it further we observe that if s^2 is suitably large compared with unity, p_m^2 as a function of m will be small for $m = 1$ and for m close to s (i.e., $m = r$), but will have a maximum at $m = s/\sqrt{2}$, with the value $p_{m \max}^2 = s^2/2$. The hyperbolic magnification factor itself, as a function of m , also has a maximum for the same m , and this maximum is

$$(p_m^{-1} \sinh p_m \tau)_{\max} = \frac{2}{s} \sinh \frac{1}{2} s^2 \tau \quad (3.48)$$

This can become very large as τ increases. If it does, there is conspicuous magnification of harmonics having m in the neighborhood of $s/\sqrt{2}$, regardless of n .

To illustrate the magnitudes involved, we consider an aluminum alloy with

$$\sigma_0 = 2.5 \times 10^4 \text{ psi}, \quad H' = 1.3 \times 10^5 \text{ psi} \quad (3.49)$$

Then from (3.43)

$$s^2 = \frac{1}{4.3} \cdot \frac{a^2}{h^2}, \quad s = \frac{1}{2.07} \cdot \frac{a}{h}, \quad m_1 = \frac{s}{\sqrt{2}} = \frac{1}{2.94} \cdot \frac{a}{h} \quad (3.50)$$

Evidently there are hyperbolic terms in (3.46) when a/h is greater than 2.07 (i.e., $s > 1$). Much larger values of a/h can allow conspicuous magnification of harmonics if (3.48) can become much larger than unity. This of course depends on the duration, the range of τ in which the compressive flow stress σ_0 is maintained and no strain-rate reversal has yet occurred. The most magnified harmonic has m close to m_1 as given in (3.50), and the corresponding half-wavelength is

$$\frac{a}{m_1} = 2.94 h \quad (3.51)$$

The bar problem analogous to the present plate problem was treated earlier [3.2]. The most magnified wavelength for a bar of rectangular section of thickness h is the same as (3.51). Thus, the hinges on the boundary conditions do not affect the wavelength.

If the initial velocity is zero, any deflection is due to initial deflection w_0 . Taking w_0 in the form (3.36), we have again (3.42) for W_{mn} in (3.36), or equivalently (3.44) for w_{mn} in (3.43). The appropriate solution is now

$$w(x_1, x_2, t) = s^2 \sum_{m=1}^{\infty} \sum_{n=1}^{\infty} \frac{a_{mn}}{s^2 - m^2} [\cosh p_m \tau - 1] \sin \frac{m\pi x_1}{a} \sin \frac{n\pi x_2}{b} \quad (3.52)$$

where \cosh is read for $m < s$, \cos for $m > s$.

The magnification factor applicable to the mn term of w_0 is now

$$\frac{s^2}{s^2 - m^2} (\cosh p_m \tau - 1) \quad (3.53)$$

This factor has occurred previously in the treatment of the bar [3.2]. Its discussion is repeated here for convenience. Supposing that s is so large that there are several hyperbolic terms, we consider (3.53) as a function of m^2 . It has a maximum where

$$\frac{s^2}{2m^2} - 1 = - \frac{\cosh p_m \tau - 1}{p_m \tau \sinh p_m \tau} \quad (3.54)$$

Conspicuous magnification depends on $\cosh p_m \tau$ becoming much larger than unity. But in this case $\sinh p_m \tau$ has an approximately equal value. Replacing the right-hand side of (3.54) by $-1/p_m \tau$, we may then observe that $p_m \tau$ must be considerably larger than unity, so $1/p_m \tau$ is small. Consequently (3.54) will require a value of m^2 slightly greater than $s^2/2$. Taking $s^2/2$ as an approximation, the

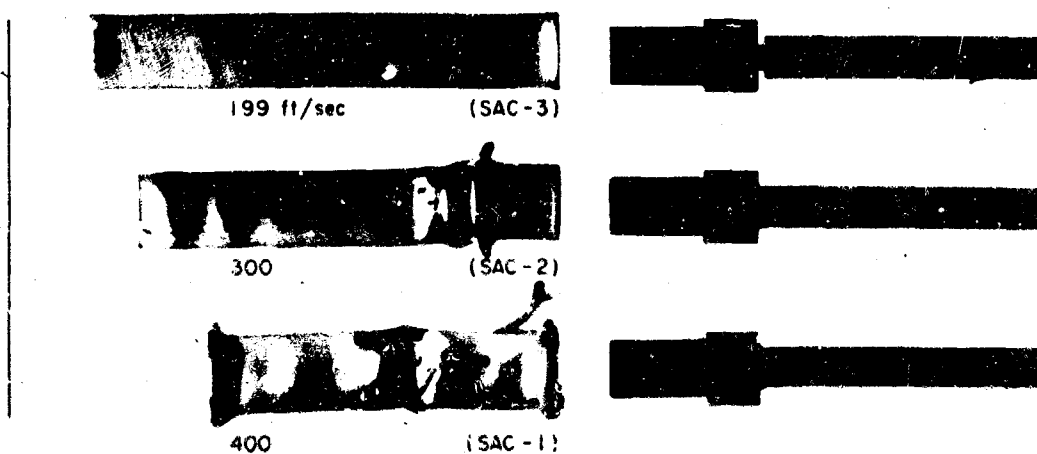
greatest magnification factor (3.53) becomes approximately $2 \cosh 1/2 s^2 \tau$. As was shown in [3.2], this in fact becomes large in durations of the order of $100 \mu\text{sec}$.

Since the magnification factor is greatest for m close to $s/\sqrt{2}$, the most magnified wavelength is the same as in the case of initial velocity perturbations.

3.6 COMPARISON WITH EXPERIMENT

Experiments were undertaken in which square tubes of aluminum (6063-T5) were projected end-on against a massive steel plate. Each side of the tube behaved as a plate in uniaxial compression. To facilitate acceleration of the tubes, they were mounted on round rods which could be fired from a standard rifle. Several specimens are shown in Figs. 3.2 to 3.9. As indicated in the figures, several combinations of boundary conditions were used.

The half-wavelengths from the specimens of Figs. 3.2 to 3.9 are listed in Tables 3.1 - 3.4. The 1/16-inch-thick plates (Tables



GP-4999 22

FIG. 3.2 1/16-INCH WALL BY 5/8-INCH-SQUARE ALUMINUM TUBING BUCKLED BY AXIAL IMPACT WITH A MASSIVE STEEL PLATE AT THE INDICATED VELOCITIES

3.1 - 3.3) show a variation in half-wavelength with boundary condition from 0.26 inch for 1/2-inch-wide plates, hinged or clamped on the long edges (depending on the response of the adjoining plates), to 0.61 inch for plates which are free on the long edges. As indicated by the large buckles in the second and third specimens of Fig. 3.2, the wavelength does not appear to depend significantly on whether the long edge is hinged or clamped. The 1/8-inch-thick plates were tested with hinged or clamped boundaries only on the long edges and show a half-wavelength of about 0.45 inch. From (3.43) the theoretical half-wavelength λ corresponding to the most magnified harmonic $m_1 = \sqrt{2}$ is

$$\lambda = \frac{a}{m_1} = \frac{\pi}{\sqrt{6}} \sqrt{\frac{H'}{\sigma_0}} h \quad (3.55)$$

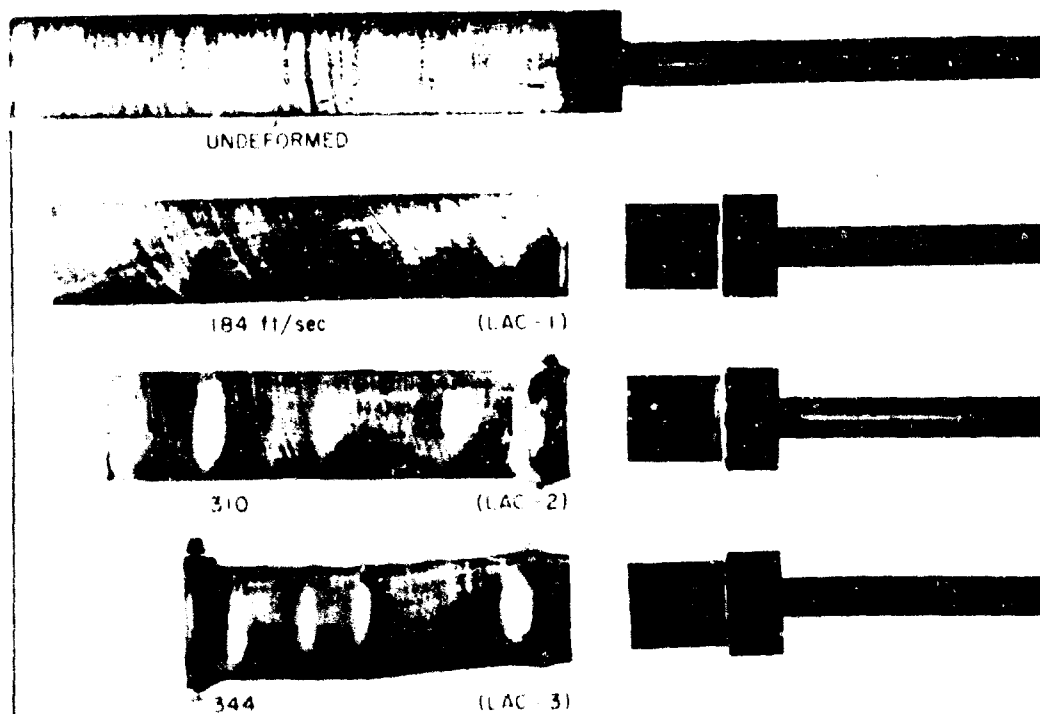
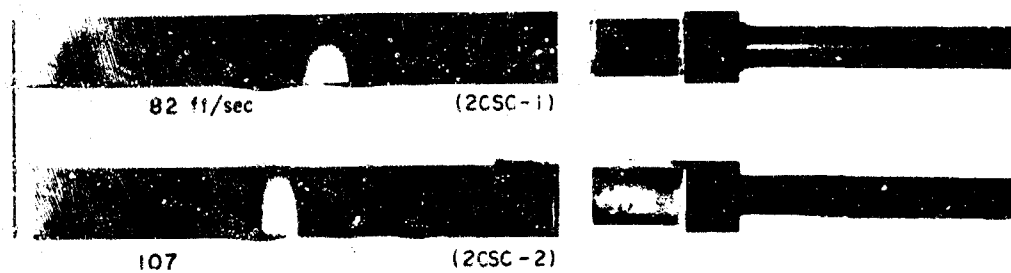
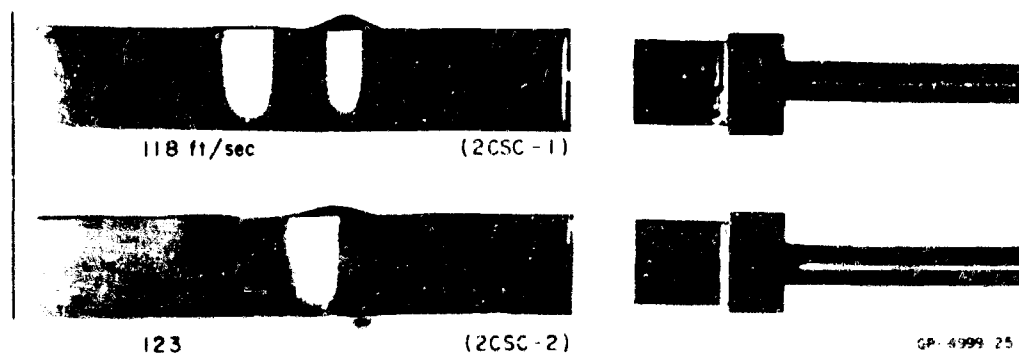


FIG. 3.3 1/16-INCH WALL BY 7/8-INCH-SQUARE ALUMINUM TUBING BUCKLED BY AXIAL IMPACT WITH A MASSIVE STEEL PLATE AT THE INDICATED VELOCITIES



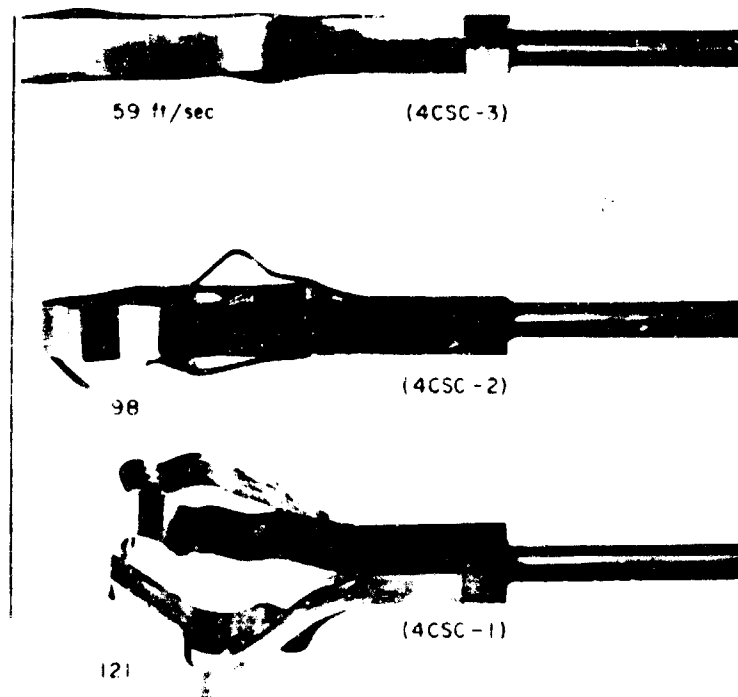
GP-4999 24

FIG. 3.4 1/16-INCH WALL BY 5/8-INCH-SQUARE ALUMINUM TUBING,
WITH TWO OPPOSITE CORNERS CUT, BUCKLED BY AXIAL IMPACT
WITH A MASSIVE STEEL PLATE AT THE INDICATED VELOCITIES



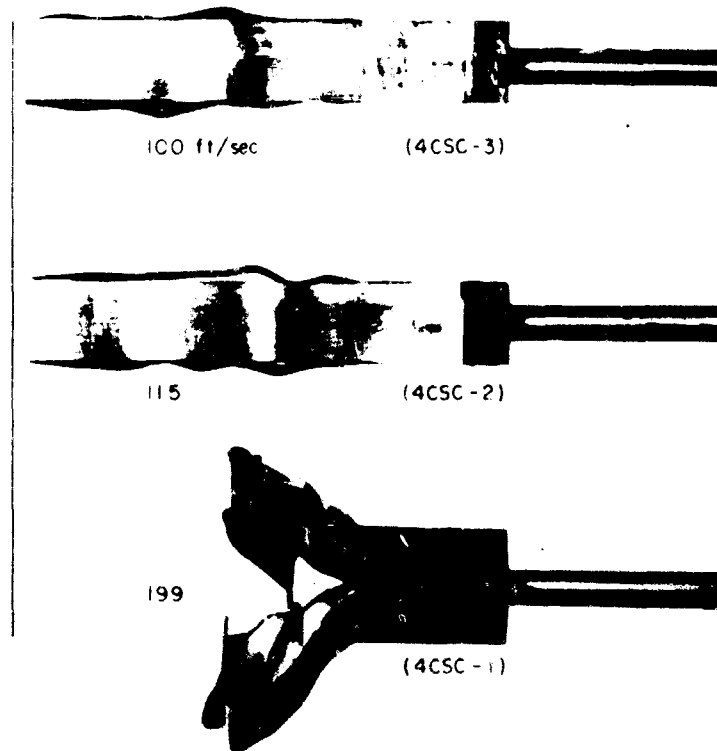
GP-4999 25

FIG. 3.5 1/16-INCH WALL BY 7/8-INCH-SQUARE ALUMINUM TUBING,
WITH TWO OPPOSITE CORNERS CUT, BUCKLED BY AXIAL IMPACT
WITH A MASSIVE STEEL PLATE AT THE INDICATED VELOCITIES



GP-4999 26

FIG. 3.6 1/16-INCH WALL BY 5/8-INCH-SQUARE ALUMINUM TUBING,
WITH FOUR CORNERS CUT, BUCKLED BY AXIAL IMPACT
WITH A MASSIVE STEEL PLATE AT THE INDICATED VELOCITIES



GP-4999-27

FIG. 3.7 1/16-INCH WALL BY 7/8-INCH-SQUARE ALUMINUM TUBING,
WITH FOUR CORNERS CUT, BUCKLED BY AXIAL IMPACT
WITH A MASSIVE STEEL PLATE AT THE INDICATED VELOCITIES

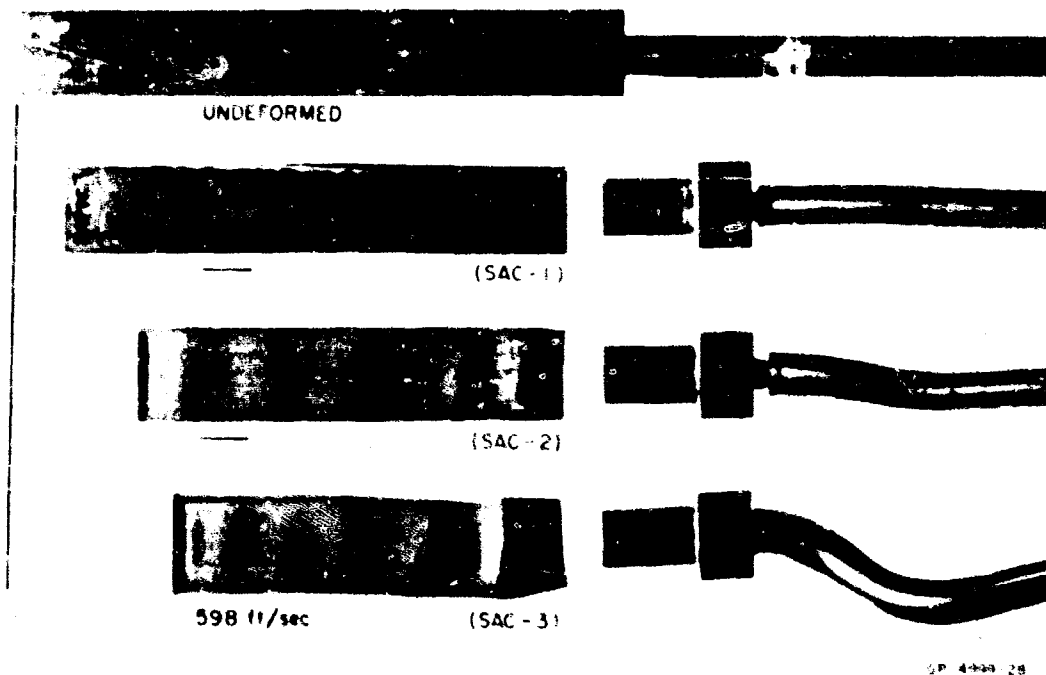


FIG. 3.8 1.8-INCH WALL BY 3 4-INCH-SQUARE ALUMINUM TUBING BUCKLED BY AXIAL IMPACT WITH A MASSIVE STEEL PLATE AT THE INDICATED VELOCITIES

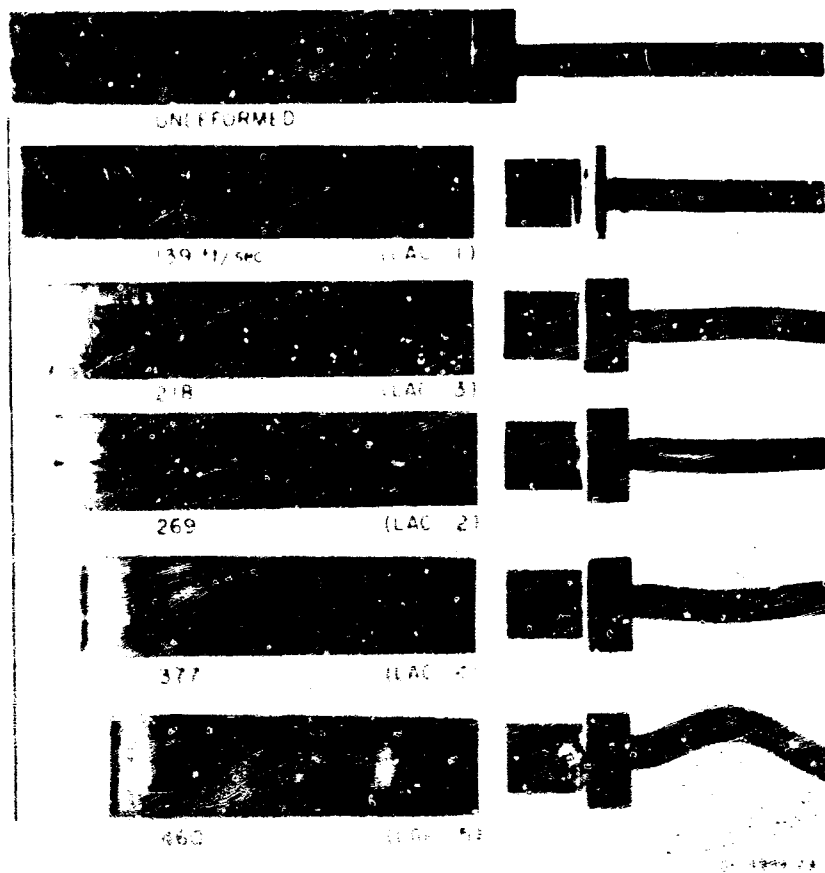


FIG. 3.9 1.8-INCH WALL BY 1-INCH-SQUARE ALUMINUM TUBING BUCKLED BY AXIAL IMPACT WITH A MASSIVE STEEL PLATE AT THE INDICATED VELOCITIES

Table 3.1

OBSERVED HALF-WAVELENGTHS FOR 1/16-INCH-THICK PLATES

Specimen	Plate Width (inch)	Impact Velocity (ft/sec)	Axial Shortening (%)	Side	Half-Wavelength (inch)										Overall Average	
					λ_1	λ_2	λ_3	λ_4	λ_5	λ_6	λ_7	λ_8	λ_9	λ_{10}		$\bar{\lambda}$
SAC-3 (Fig. 3.2)	1/2	199	10	1	.24	.15	.22	.27							.22	.26
				2	.31	.23	.30	.35							.30	
				3	.23	.21	.19	.19	.13	.19	.24	.48	.24	.11	.22	
				4	.32	.31	.45	.25	.35	.26					.32	
SAC-2 (Fig. 3.2)	1/2	300	23	1	.26	.29	.24	.26	.21	.27	.29				.26	.26
				2	.23	.35	.27	.25	.19	.30	.21				.26	
				3	.25	.32	.37	.27	.23	.21					.27	
				4	.26	.31	.31	.33	.28	.19	.20	.19	.22		.25	
SAC-1 (Fig. 3.2)	1/2	400	36	1	.30	.32									.31	.31
				2	.30	.31									.30	
				3	.28	.35	.27	.24	.44						.32	
				4	.31	.32									.32	
LAC-1 (Fig. 3.3)	3/4	184	7	1	.32	.37	.36	.40	.37	.34	.32				.35	.38
				2	.38	.41	.29	.37	.28						.48	
				3	.43	.52									.39	
				4	.36	.41	.41	.39	.45	.33					.42	
LAC-2 (Fig. 3.3)	3/4	310	16	1	.46	.47	.33	.36	.48	.41					.41	.41
				2	.42	.46	.37	.40	.46	.40	.35				.39	
				3	.39	.39	.34	.42	.43						.43	
				4	.47	.44	.42	.42	.49	.44	.33				.38	
LAC-3 (Fig. 3.3)	3/4	344	30	1	.43	.37	.32	.37	.38	.31	.52	.34			.38	.36
				2	.31	.38	.44	.44	.48	.32	.24	.27	.35		.36	
				3	.52	.37	.47	.40	.34	.25	.35	.34			.38	
				4	.43	.36	.32	.45	.29	.30	.27	.28	.35		.34	

Table 3.2

OBSERVED HALF-WAVELENGTHS FOR 1/16-INCH-THICK PLATES WITH ONE FREE EDGE

Specimen	Plate Width (inch)	Impact Velocity (ft/sec)	Axial Shortening (%)	Side	Half-Wavelength (inch)							Overall Average	
					λ_1	λ_2	λ_3	λ_4	λ_5	λ_6	$\bar{\lambda}$		
2CSC-1 (Fig. 3.4)	1/2	82	2	1	.46	.50	.52					.49	.43
				2	.48	.42	.44	.45			.45		
				3	.46	.34	.45				.42		
				4	.36	.32	.40	.39			.37		
2CSC-2 (Fig. 3.4)	1/2	107		1	.47	.47	.38	.57			.47	.39	
				2	.49	.41	.42	.37	.41		.42		
				3	.31	.33	.41	.35	.40		.36		
				4	.41	.28	.24	.33	.40	.37	.34		
2CSC-1 (Fig. 3.5)	3/4	118	4	1	.45	.43					.44	.50	
				2	.47	.44					.46		
				3	.60	.67	.49				.59		
				4	.51	.48					.50		
2CSC-1 (Fig. 3.5)	3/4	123	1	1	.47	.45					.46	.48	
				2	.47	.42	.39				.43		
				3	.43	.45	.42	.51			.45		
				4	.58	.54	.59				.57		

Table 3.3

OBSERVED HALF-WAVELENGTHS FOR 1/16-INCH-THICK PLATES
WITH TWO FREE EDGES

Specimen	Plate Width (inch)	Impact Velocity (ft/sec)	Axial Shortening (%)	Side	Half-Wavelength (inch)								Overall Average
					λ_1	λ_2	λ_3	λ_4	λ_5	λ_6	λ_7	$\bar{\lambda}$	
4CSC-3 (Fig. 3.6)	~ 1/2	59	1	1	.57	.53	.65					.58	.61
				2	.61	.69						.65	
				3	.67	.57	.51					.58	
				4	.71	.64	.61	.60				.64	
4CSC-3 (Fig. 3.7)	~ 3/4	100	3	1	.38	.52	.67	.43	.56			.51	.51
				2	.48	.62	.61	.54				.56	
				3	.35	.34	.35	.66	.65			.47	
				4	.58	.51	.51	.41				.50	
4CSC-2 (Fig. 3.7)	~ 3/4	115	3	1	.60	.59	.49	.60				.57	.48
				2	.51	.40	.46	.44				.45	
				3	.58	.61	.43	.39	.42			.49	
				4	.50	.42	.43	.45	.38	.35	.50	.43	

Table 3.4

OBSERVED HALF-WAVELENGTHS FOR 1/8-INCH-THICK PLATES

Specimen	Plate Width (inch)	Impact Velocity (ft/sec)	Axial Shortening (%)	Side	Half-Wavelength (inch)									Overall Average
					λ_1	λ_2	λ_3	λ_4	λ_5	λ_6	λ_7	λ_8	λ_9	
SAC-1 (Fig. 3.8)	1/2		9											.41
SAC-2 (Fig. 3.8)	1/2		23	1	.45	.47	.54	.45	.47	.40	.38			.45
				2	.35	.45	.44	.40	.32					.39
				3	.31	.28	.54	.49	.40	.43	.44	.34		.40
				4	.35	.45	.49	.38	.42	.38	.32	.31		.39
SAC-3 (Fig. 3.8)	1/2	578	29	1	.49	.44	.42	.43	.46	.35	.28			.41
				2	.55	.37	.45	.24	.35	.20	.28			.35
				3	.31	.42	.42	.38	.34	.23	.24	.22	.36	.32
				4	.41	.48	.38	.52	.59	.30				.45
LAC-1 (Fig. 3.9)	3/4	139	2											.37
LAC-3 (Fig. 3.9)	3/4	218	7											
LAC-2 (Fig. 3.9)	3/4	269	8											.37
LAC-4 (Fig. 3.9)	3/4	377	15	1	.34									.34
				2	.36	.34	.37	.36						.36
				3	.36									.36
				4	.42	.43								.42
LAC-5 (Fig. 3.9)	3/4	460	20	1	.49	.49								.49
				2	.45	.40	.62	.47	.38					.46
				3	.58	.48								.53
				4	.64	.53	.41	.39						.49

As indicated in Fig. 3.10, the factor $\sqrt{H'/\sigma_0}$ varies considerably from 1 to 10 percent strain, decreasing as strain increases. Thus, (3.55) indicates that the half-wavelength should decrease as strain increases. This expectation is borne out by the data, as may be seen by comparing Tables 3.1 - 3.3. The effect of freeing the long edges appears to be to increase the instability so that buckling occurs at lower axial strains.

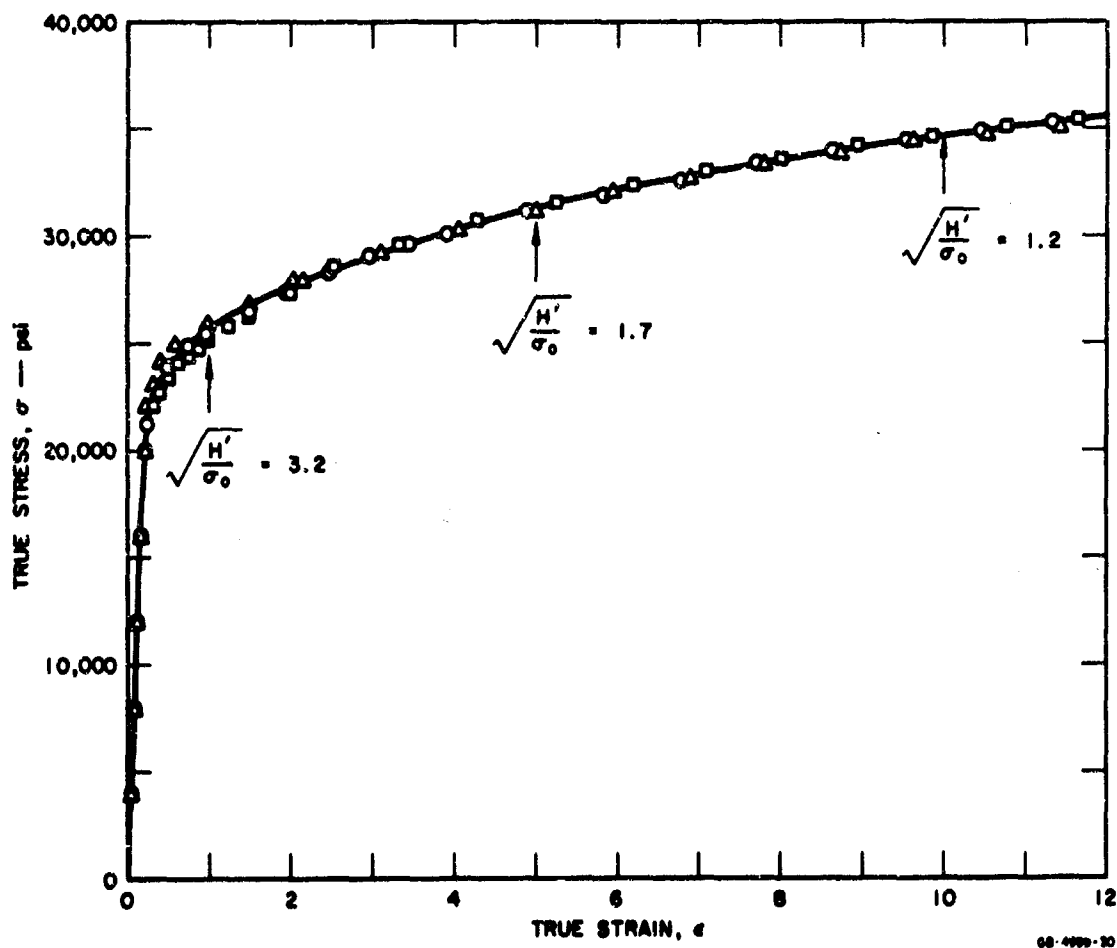


FIG. 3.10 STRESS-STRAIN CURVE FOR TUBING MATERIAL (Aluminum 6063-T5)

In Table 3.5 theoretical half-wavelengths are given for values of $\sqrt{H'/\sigma_0}$ corresponding to strains in the region of interest. For the 1/16-inch-thick plates the predicted half-wavelengths for strains of 1 and 5 percent are 0.26 and 0.14 inch. The observed half-wavelengths vary from 0.26 to 0.61 inch. The difference is attributed to the effects of early elastic deformations on the subsequent plastic deformation [3.4]. For the 1/8-inch-thick plates the predicted half-wavelengths for strains of 1, 5, and 10 percent are 0.52, 0.27, and 0.19 inch. The observed half-wavelengths (Table 3.4) fall within the values for 1 and 5 percent strain.

The agreement between theoretical and experimental wavelengths is reasonable, indicating that the theory describes the mechanics fairly well. The largest factor yet to be accounted for in the theory is the variation in H'/σ_0 with strain.

Table 3.5
CALCULATED HALF-WAVELENGTHS

h (inch)	Assumed Buckling Strain (%)	$\frac{\sigma_0}{H'}$	$\frac{\lambda}{h}$	λ (inch)
0.062	1	0.096	4.13	0.26
	5	0.35	2.17	0.14
0.125	1	0.096	4.13	0.52
	5	0.35	2.17	0.27
	10	0.69	1.54	0.19

REFERENCES

- 3.1 Abrahamson, G. R. and J. N. Goodier, "Dynamic Plastic Flow Buckling of a Cylindrical Shell under Uniform Radial Impulse," Proceedings of the 4th U.S. National Congress of Applied Mechanics, Berkeley, June 18-21, 1962.
- 3.2 Abrahamson, G. R. and J. N. Goodier, "Dynamic Flexural Buckling of Rods Within an Axial Plastic Compression Wave," presented at West Coast Conference on Applied Mechanics, U. C. L. A., August 30, 1965, (to be published in J. Appl. Mech.).
- 3.3 Hill, R., Plasticity, Oxford University Press, New York, 1950.
- 3.4 Shanley, F. R., "Inelastic Column Theory," J. Aero. Sci. Vol. 14, 1947, pp. 261-268.
- 3.5 Pearson, C. E., "Bifurcation Criterion and Plastic Buckling of Plates and Columns," J. Aero. Sci. Vol. 17, 1950, pp. 417-424.

4. DYNAMIC BUCKLING OF A THIN CYLINDRICAL SHELL UNDER AXIAL IMPACT

4.1 INTRODUCTION

Experimental investigations by Coppa [4.1] and others have shown that thin cylindrical shells subjected to axial impact can buckle dynamically into the familiar diamond pattern of large deflection static buckling. The diamonds in the dynamically buckled shells, however, are smaller than in the static pattern because higher modes respond faster than lower ones and soon predominate the motion. Dynamic buckling into very high-order modes (short wavelength) has also been observed in cylindrical shells under impulsive radial pressure [4.2] and in thin bars under axial impact [4.3]. In these latter problems, the very short wavelengths can be attributed directly to the very high thrusts compared to those in static buckling. In cylindrical shells under dynamic axial thrust, however, the thrust does not have to be greater than the classical static buckling load to produce wavelengths shorter than those observed in large deflection static buckling. Using high-speed photography of a shell buckling elastically under static thrust, Almroth, Holmes, and Brush [4.4] showed that the shell initially deformed into diamonds of roughly half the size of those in the final buckled shape. In other experiments, by placing a rigid mandrel inside the shell to limit the amplitude of post-buckling deformation, they were able to keep the shell buckled in the shorter wavelength pattern. Thus, in a cylindrical shell under dynamic axial thrust, the modes of deformation can be expected to depend in general upon the amplitude of deformation as well as upon the magnitude of the thrust.

These complications in the cylindrical shell have led theoretical investigations of dynamic buckling toward a large deflection theory as was found to be required for static buckling. The general procedure has been to assume axial and circumferential buckle wavelengths and to numerically integrate equations derived from large deflection shell theory. The coefficients of a few terms giving roughly the diamond buckle shape are taken as generalized coordinates and the Galerkin procedure is used to derive equations governing these coefficients. Buckling is said to occur when the deflections increase abruptly with load or end shortening. The procedure is repeated over a range of axial and circumferential wavelengths to find the combination that gives the lowest buckling load. Coppa and Nash [4.5] used a two-degree-of-freedom system, taking the end shortening to increase linearly with time. Roth and Klosner [4.6] used a four-degree-of-freedom system and a step pressure. No comparison of these theories with experiment was made.

The drawback of the above procedure is that two of the essential unknowns of the problem, the axial and circumferential wavelengths of the buckles, must be assumed at the outset of the integration. To determine the wavelengths into which the shell actually buckles, the procedure must be repeated over and over for many combinations of axial and circumferential wavelengths. For buckling in which the impact stress is greater than the static classical buckling stress, this shortcoming is overcome in the present paper by using linear theory to study the wave selection process in the early motion while the deflections are still small. This allows application of the analytical procedure used in the beam under axial impact [4.3]. The buckled form is not specified a priori; instead the motion is expanded into the linear vibration modes of the shell so that it is free to deform into its own "preferred" shape. Initial imperfections are taken in the form of white noise and a statistical analysis gives the expected values for the axial and circumferential wavelengths. If the initial imperfections are sufficiently small, the ratio of amplitudes of the preferred modes to the amplitudes of the imperfections can become quite large within the applicability of small deflection

theory, and this dominance of the preferred linear wavelengths could carry over into the large deflection motion.

Experiments are presented which give final buckled forms very close to those predicted by the theory. Very high-speed motion pictures (240,000 frames per sec) show buckles forming during the elastic and plastic motion and demonstrate that the time scale of the buckle formation also agrees with the theory. The axial wavelengths are much shorter than in static buckling and the observed aspect ratios (circumferential to axial) are much larger, averaging about 3 compared to 1 in static buckling. This varied considerably and in many experiments nearly symmetric (very large aspect ratio) buckling was observed.

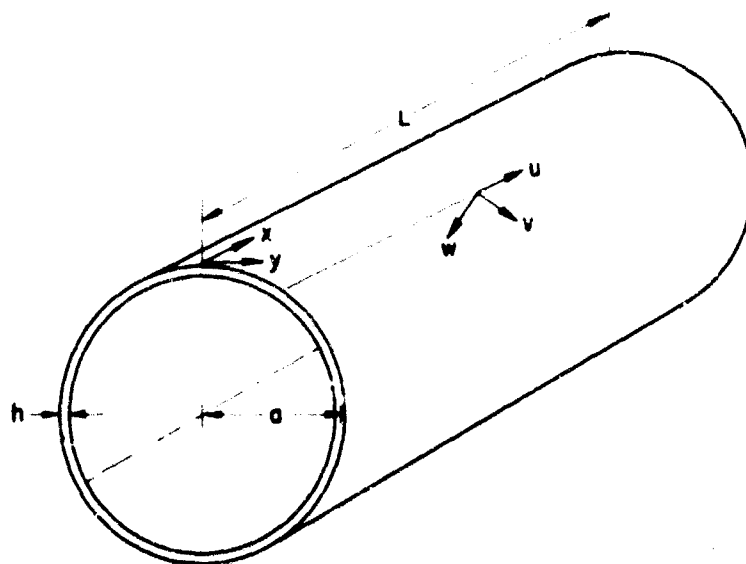
4.2 RESPONSE OF THE NORMAL MODES

In the experiments, cylindrical shells are impacted at one end by a massive ring which sends a step axial stress wave down the shell. The shell buckles before any signal is received from the opposite (free) end so that in the theory the shell is taken arbitrarily long. Also, the thrust is assumed uniform throughout the length of the shell, thus neglecting any effects of the moving axial stress front. This was shown to be a reasonable assumption for the axially impacted strip [4.3], and appears to be valid here also, since as shown below, the axial wavelengths and formation times of the buckles in the strip and cylinder are quite similar. Thus, we consider a long, thin cylindrical shell subjected to a suddenly applied constant compressive force.

To study the small early displacements, it is sufficient to use a small deflection linear theory. It can be further shown that simplified Donnell-type equations give satisfactory accuracy for the present problem.

* If more complete equations, such as given in [4.8], are used, the final equation (12) here results if terms multiplying the axial strain $\epsilon = N/Eh$ and terms containing $(h/a)^2$ are omitted as small compared to terms without these small multipliers.

Denoting time by t and axial force per unit arc length by N , and taking, as shown in Fig. 4.1, x and y to be the axial and circumferential



m = NUMBER OF AXIAL HALF-WAVES
 n = NUMBER OF CIRCUMFERENTIAL WAVES

FIG. 4.1 COORDINATES AND SHELL NOMENCLATURE

coordinates, and w to be the radially inward displacement measured from the initial perturbed displacement w_0 , these equations become

$$D \nabla^4 w + N \frac{\partial^2}{\partial x^2} (w + w_0) + \rho h \frac{\partial^2 w}{\partial t^2} - \frac{h}{a} \frac{\partial^2 F}{\partial x^2} = 0 \quad (4.1)$$

$$\nabla^4 F + \frac{E}{a} \frac{\partial^2 w}{\partial x^2} = 0 \quad (4.2)$$

where F is Airy's stress function for mid-surface stresses produced by the buckling, a is the shell radius, h is the thickness, ρ is the density, $D = Eh^3/12(1-\nu^2)$ is the flexural stiffness and ∇^4 is the operator $(\partial^2/\partial x^2 + \partial^2/\partial y^2)^2$. These are equations (3) and (4) from [4.7] with terms appropriate to the present problem retained.

Using non-dimensional variables

$$\xi = x \sqrt{\frac{N}{D}}, \quad \eta = y \sqrt{\frac{N}{D}}, \quad \tau = \frac{N}{\sqrt{chD}} t \quad (4.3)$$

equations (4.1) and (4.2) become

$$\nabla^4 w + \frac{\partial^2}{\partial \xi^2} (w + w_0) + \ddot{w} - \frac{h}{aN} \frac{\partial^2 F}{\partial \xi^2} = 0 \quad (4.4)$$

$$\nabla^4 F + \frac{ED}{aN} \frac{\partial^2 w}{\partial \xi^2} = 0 \quad (4.5)$$

where the operator ∇^4 is now $(\partial^2/\partial \xi^2 + \partial^2/\partial \eta^2)^2$, and $(\cdot) = \partial/\partial \tau$.

To simplify the mathematics, the shell will be considered simply supported. The edge condition at the impacted end of the shells in the experiments is more closely approximated by a clamped boundary, but the experiments indicate that this boundary condition does not significantly affect the buckling. The conditions of simple support are satisfied by

$$w(\xi, \eta, \tau) = \sum_{m=1}^{\infty} \sum_{n=1}^{\infty} W_{mn}(\tau) \sin \alpha_m \xi \sin \beta_n \eta \quad (4.6)$$

$$F(\xi, \eta, \tau) = \sum_{m=1}^{\infty} \sum_{n=1}^{\infty} F_{mn}(\tau) \sin \alpha_m \xi \sin \beta_n \eta \quad (4.7)$$

where

$$\alpha_m = \frac{m\pi}{L} \sqrt{\frac{D}{N}}, \quad \beta_n = \frac{n\pi}{a} \sqrt{\frac{D}{N}} \quad (4.8)$$

and L is the length of the shell. The initial displacement w_0 is also expanded into a Fourier series:

$$w_0(\xi, \eta) = \sum_{m=1}^{\infty} \sum_{n=1}^{\infty} a_{mn} \sin \alpha_m \xi \sin \beta_n \eta \quad (4.9)$$

Equation (4.7) is now substituted into (4.5) and the result is substituted with (4.6) into (4.4) to give the following equation for the amplitudes W_{mn} of the normal modes.

$$\ddot{W}_{mn} + [(\alpha_m^2 + \beta_n^2)^2 - \alpha_m^2 + \frac{EDh}{a^2 N^2} \frac{\alpha_m^4}{(\alpha_m^2 + \beta_n^2)^2}] W_{mn} = \alpha_m^2 a_{mn} \quad (4.10)$$

In the limit as $L \rightarrow \infty$, α_m becomes a continuous variable and, for convenience, β_n will also be treated as a continuous variable so that in the following $W_{mn}(\tau)$ is replaced by $W(\alpha, \beta, \tau)$ and the subscripts on α and β are dropped. Noting further that

$$\frac{EDh}{a^2 N^2} = \frac{1}{4} \left(\frac{\sigma_{cl}}{\sigma} \right)^2$$

where

$$\sigma_{cl} = \frac{E}{\sqrt{3(1-\nu^2)}} \frac{h}{a} \quad (4.11)$$

is the classical static buckling stress, (4.10) can be written

$$\ddot{g} + k(\alpha, \beta) g = \alpha^2 \quad (4.12)$$

where

$$k(\alpha, \beta) = (\alpha^2 + \beta^2)^2 - \alpha^2 + \frac{1}{4} \left(\frac{\sigma_{cl}}{\sigma} \right)^2 \frac{\alpha^4}{(\alpha^2 + \beta^2)^2} \quad (4.13)$$

and

$$g(\alpha, \beta, \tau) = \frac{W(\alpha, \beta, \tau)}{a(\alpha, \beta)} \quad (4.14)$$

is the amplification function or "filter" characteristic of the shell under a given axial stress $\sigma = N/h$.

The solution to (4.12) subject to the initial conditions $g(\alpha, \beta, 0) = \dot{g}(\alpha, \beta, 0) = 0$ is

$$g(\alpha, \beta, \tau) = \frac{\alpha^2}{k(\alpha, \beta)} \left[1 - \frac{\cosh p\tau}{\cos p\tau} \right] \quad (4.15)$$

where

$$p = |k(\alpha, \beta)|^{1/2}$$

and the hyperbolic form is taken for $k(\alpha, \beta) < 0$. Figure 4.2 gives example plots of $g(\alpha, \beta, \tau)$ for $\tau = 4$ and $\tau = 8$. The dependence of these amplitudes on the axial wave number α is similar to that in the buckling bar, exhibiting a pronounced hump of "preferred" modes near $\alpha = 1/\sqrt{2}$. The circumferential wave number of the most amplified mode is $\beta = 0$, i.e., a symmetric mode, but there is an appreciable bandwidth of amplified modes in both the axial and circumferential directions. Comparing the curves for $\tau = 4$ and $\tau = 8$ we see that as the motion proceeds, the bandwidth in both directions decreases, tending in the limit to produce a fixed axial wavelength corresponding to the wavenumber $\alpha \approx 1/\sqrt{2}$, but tending toward longer wavelengths in the circumferential direction, ultimately approaching a simple symmetric pattern corresponding to $\beta = 0$ (i.e., $n = 0$). If the imperfections are large enough, however, non-linear effects would dominate before the symmetric mode is attained, producing final buckles with a finite wavelength in both directions. Buckling of both types were observed in the experiments described below.

From the definition of $k(\alpha, \beta)$ in (4.13) we see that the normalized amplification curves $g(\alpha, \beta, \tau)$ depend only on the ratio σ/σ_{cl} of the applied axial stress to the classical static buckling stress. Larger values give faster growth and narrower bandwidths, but the general shape of the amplification curves remains about the same for any $\sigma/\sigma_{cl} > 1$. In the next section it will be shown that the expected values of the buckle wavelengths are very nearly proportional to $\sqrt{\frac{N}{D}} = r/\sqrt{\epsilon}$, where $r = h/\sqrt{12(1-\nu^2)}$ and $\epsilon = \sigma/E$ is the strain from the axial thrust.

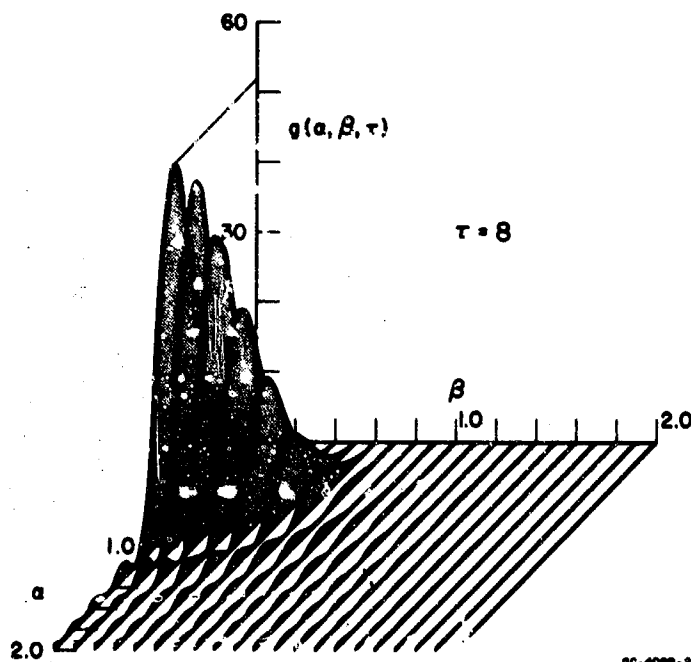
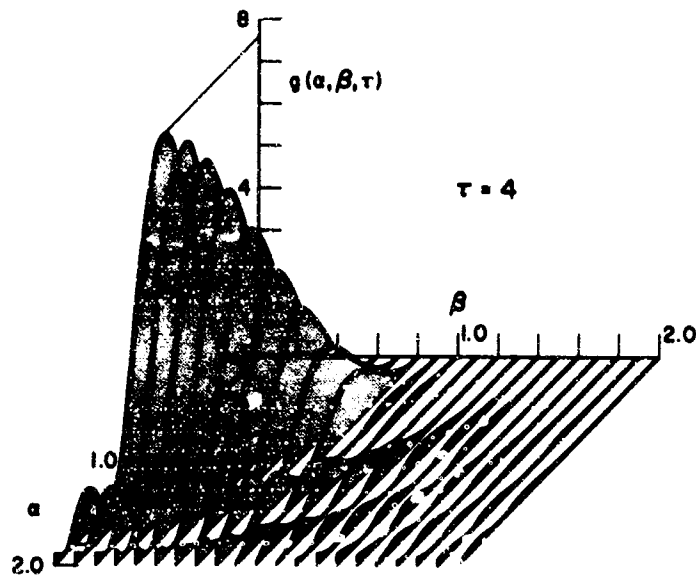


FIG. 4.2 AMPLIFICATION FUNCTION g vs. AXIAL AND CIRCUMFERENTIAL WAVE NUMBERS α AND β FOR $\sigma/\sigma_{cl} = 2.5$

Figure 4.3 gives a plot of the maximum value of g (at the peak of the hump in Fig. 4.2) plotted against time for several values of σ/σ_{cl} . As $a/h \rightarrow \infty$ we see from (4.11) that $\sigma_{cl} \rightarrow 0$ so that the curve for

$\sigma/\sigma_{cr} \rightarrow \infty$ is that for a buckling plate (or rectangular bar if the factor $1-\nu^2$ is omitted). For $\sigma/\sigma_{cr} > 2$ the time required to attain large amplification is only slightly greater than for the plate.

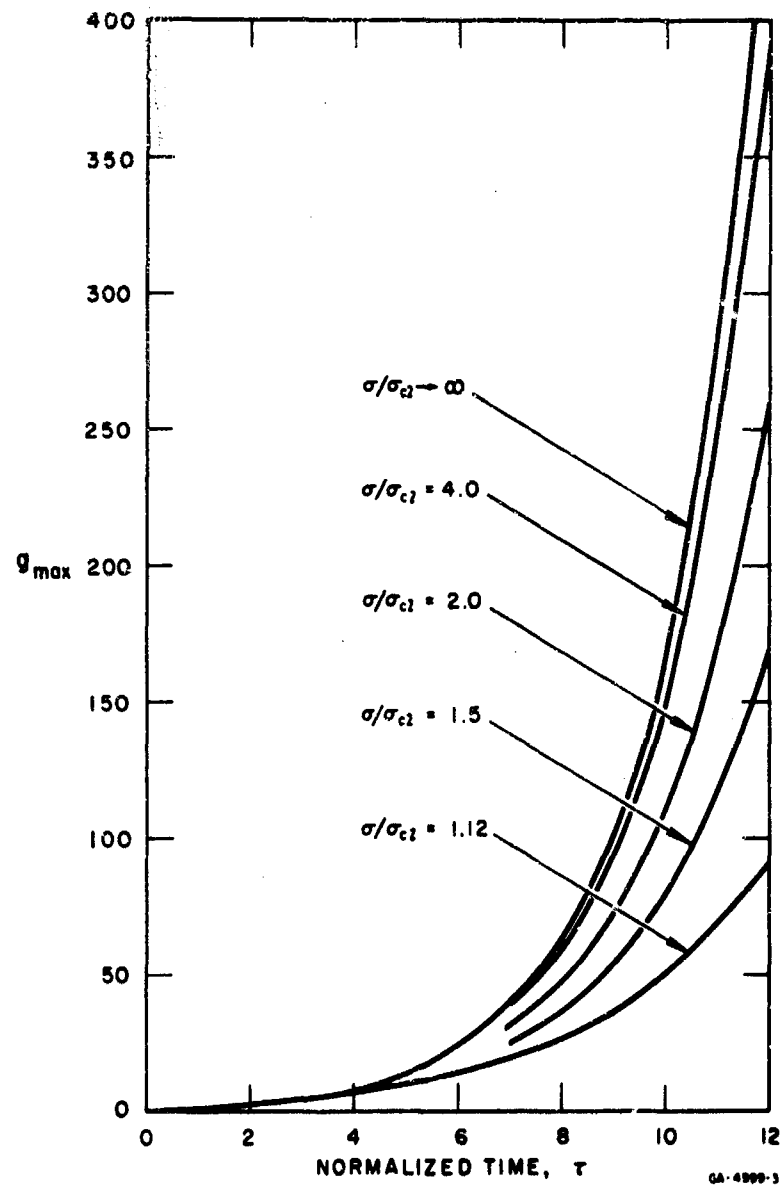


FIG. 4.3 GROWTH OF MAXIMUM AMPLIFICATION WITH TIME

4.3 BUCKLING FROM RANDOM IMPERFECTIONS

To compare theory with experiment, it is necessary to assume some form of imperfections in order to specify $a(\alpha, \beta)$ and hence to compute

$W(\alpha, \beta, \tau)$ from (4.14). Experiments on impact buckling of bars in [4.3] demonstrated that a good description of the observed buckles was obtained by assuming imperfections in the form of white noise. These allow the buckle wavelengths to be dictated by the magnitude of the thrust, giving a random scatter of wavelengths with a mean and standard deviation both inversely proportional to the square root of the thrust, in agreement with experimental observations. It is expected that such an assumption will also be reasonable in the present problem. Thus, we assume the $a(\alpha, \beta)$ are random normal with zero mean and constant variance over all α and β in the amplified band of interest. With this assumption, the power spectral density of the modal amplitudes $W(\alpha, \beta, \tau)$ is proportional to $g^2(\alpha, \beta, \tau)$.

Having the power spectral density, the statistics of the buckled shape can be computed. For the bar [4.3], complete statistics of the wavelengths were computed using a Monte Carlo technique. The simpler problem of determining the mean wavelengths can be solved analytically and will be undertaken here for the shell. From Rice [4.9] the expected number of zeros in an interval (s_1, s_2) of a random function $f = F(s)$ is

$$\int_{s_1}^{s_2} ds \int_{-\infty}^{\infty} |q| P(0, q; s) dq \quad (4.16)$$

where $P(f, q; s)$ is the probability density function for the variables

$$f = F(s)$$

$$q = \frac{dF}{ds}$$

For our problem we have then, that the expected number of zeros in the ξ direction in the interval $(0, l)$, for a specified value of η and τ is

$$R = \int_0^l d\xi \int_{-\infty}^{\infty} |z| P(0, z; \xi, \eta, \tau) dz \quad (4.17)$$

where $l = L\sqrt{\frac{N}{D}}$ and $P(w, z; \xi, \eta, \tau)$ is the probability density function of the variables

$$w = w(\xi, \eta, \tau)$$

$$z = \frac{\partial w}{\partial \xi}$$

and ξ, η, τ are carried along as parameters. Since it has been assumed that the initial imperfections have a Gaussian probability distribution (or, alternately, if we apply the central limit theorem for more general imperfection statistics) then the final buckled form will also have a Gaussian distribution. Thus, the distribution function has the form

$$P(w, z; \xi, \eta, \tau) = \frac{1}{2\pi(\mu_{11}\mu_{22} - \mu_{12}^2)^{1/2}} \cdot \exp \left\{ \frac{-\mu_{11}w^2 + 2\mu_{12}wz - \mu_{22}z^2}{2(\mu_{11}\mu_{22} - \mu_{12}^2)} \right\} \quad (4.18)$$

where

$$\mu_{11} = \langle w^2 \rangle$$

$$\mu_{22} = \langle z^2 \rangle$$

$$\mu_{12} = \langle wz \rangle$$

and $\langle \rangle$ indicates ensemble average.

Our results are simplified if it is assumed that the imperfections and final buckled form are stationary (in space) so that in place of (4.6) we can write

$$w(\xi, \eta, \tau) = \sum_{m=1}^{\infty} \sum_{n=1}^{\infty} W_{mn}(\tau) \sin(\alpha_m \xi - \varphi_m) \sin(\beta_n \eta - \theta_n) \quad (4.19)$$

where the φ_m and θ_n are each uniformly distributed over the interval $(0, 2\pi)$. With this assumption the statistics of the buckled form are independent of ξ and η , which we would expect to be justifiable for waves at a sufficient distance from the ends of the cylinder. In fact, the results of a Monte Carlo computation including end effects for the bar [4.3], which is similar in form to the cylinder, indicate satisfactory agreement with the stationary process assumption even for the first wave from the simple support.

Using (4.19) it can be easily shown that

$$\mu_{11} = \langle w^2 \rangle = \int_0^{\infty} \int_0^{\infty} W^2(\alpha, \beta, \tau) d\alpha d\beta = \sigma^2 \int_0^{\infty} \int_0^{\infty} g^2(\alpha, \beta, \tau) d\alpha d\beta \quad (4.20a)$$

$$\mu_{22} = \langle z^2 \rangle = \int_0^{\infty} \int_0^{\infty} a^2 W^2(\alpha, \beta, \tau) d\alpha d\beta = \sigma^2 \int_0^{\infty} \int_0^{\infty} a^2 g^2(\alpha, \beta, \tau) d\alpha d\beta \quad (4.20b)$$

$$\mu_{12} = \langle wz \rangle = 0 \quad (4.20c)$$

where

$$\sigma^2 = \langle a^2(\alpha, \beta) \rangle = \text{constant}$$

and the sums have been replaced by integrals.

Making use of $\mu_{12} = 0$ from (4.20c) in (4.18) and substituting the resulting expression in (4.17) gives the expected number of zeros in the length l ,

$$R = \frac{l}{\pi} \left(\frac{\mu_{22}}{\mu_{11}} \right)^{1/2} \quad (4.21)$$

The mean wavelength, as measured between alternate zero crossings, is simply

$$\lambda_{\xi} = \frac{2l}{R} = 2\pi \left(\frac{\mu_{11}}{\mu_{22}} \right)^{1/2} \quad (4.22)$$

or, upon using (4.20)

$$\lambda_{\xi} = 2\pi \left[\frac{\int_0^{\infty} \int_0^{\infty} g^2(\alpha, \beta, \tau) d\alpha d\beta}{\int_0^{\infty} \int_0^{\infty} \alpha^2 g^2(\alpha, \beta, \tau) d\alpha d\beta} \right]^{1/2} \quad (4.23)$$

The mean wavelength in the circumferential direction can similarly be shown to be

$$\lambda_{\eta} = 2\pi \left[\frac{\int_0^{\infty} \int_0^{\infty} g^2(\alpha, \beta, \tau) d\alpha d\beta}{\int_0^{\infty} \int_0^{\infty} \beta^2 g^2(\alpha, \beta, \tau) d\alpha d\beta} \right]^{1/2} \quad (4.24)$$

Equations (4.23) and (4.24) were integrated numerically over the area $0 \leq \alpha \leq 2$, $0 \leq \beta \leq 2$ of significant amplification and the results are presented in Fig. 4.4. In Fig. 4.4(a) the variation of λ_{ξ} and λ_{η} with τ is shown. Bands have been drawn which contain the curves for σ/σ_{cl} in the range from 1.12 to 4.0. The narrowness of these bands indicates that the most significant parameters affecting wavelength are those given in the normalization in (4.3).

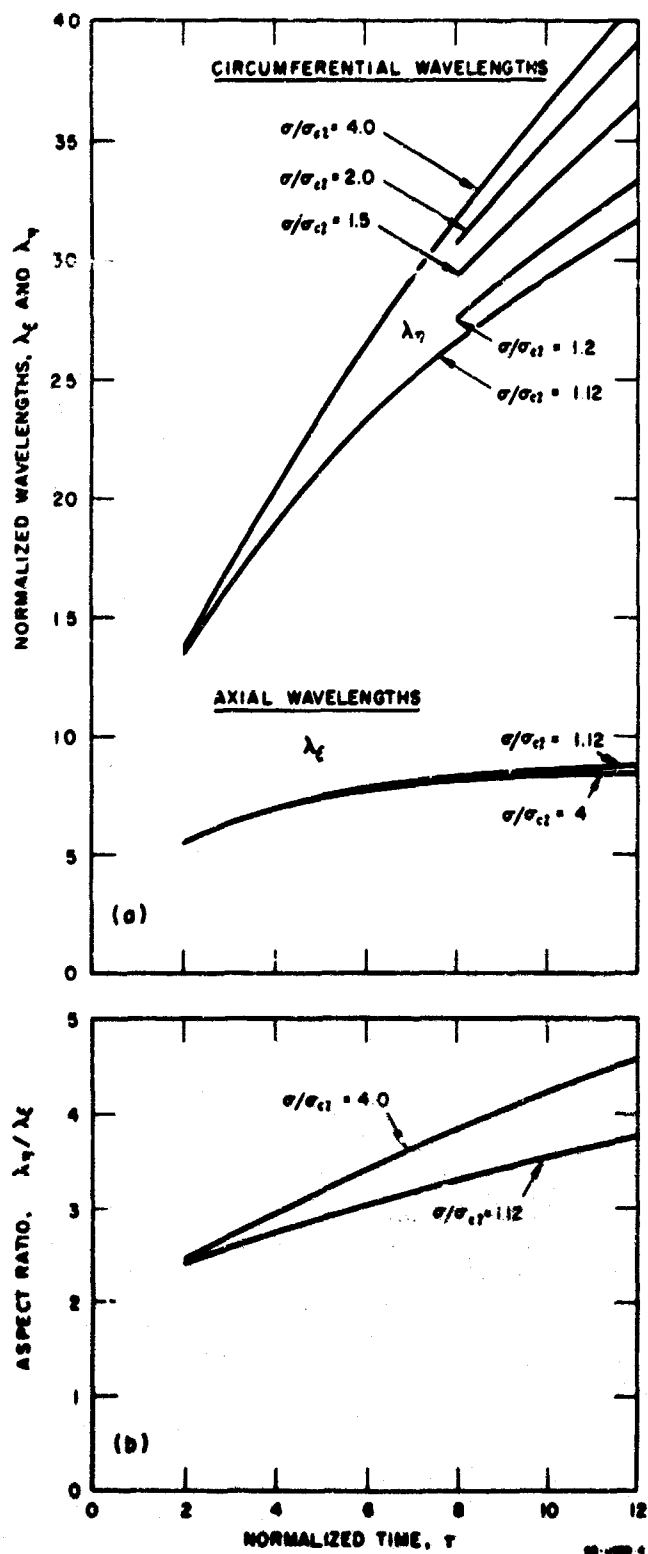


FIG. 4.4 AXIAL AND CIRCUMFERENTIAL MEAN WAVELENGTHS vs. TIME

Also from Fig. 4.4(a), we see that the mean axial wavelength increases only slightly with τ for $\tau > 4$ and quickly approaches a "preferred" wavelength. For ratios of σ/σ_{cl} nearing unity the preferred wavelength becomes the classical static wavelength $\lambda_F = 2\sqrt{2}\pi$. The mean circumferential wavelength, however, increases with τ without approaching an asymptotic value. Thus, as discussed in the previous section, the mean circumferential wavelengths actually observed in large deflection buckling will probably depend on the magnitude of the initial imperfections, which determines the duration for which this small deflection theory is applicable. Smaller imperfections can grow for a longer time and from Fig. 4.4(a) we would expect to see longer circumferential wavelengths.

Figure 4.4(b) gives a plot of the aspect ratio λ_r/λ_θ . If nonlinear effects begin to dominate at, say $\tau = 7$, and subsequent buckling proceeds with a fixed pattern (one would expect a fixed pattern to be eventually established, as confirmed in the experiments), Fig. 4.4(b) indicates that the aspect ratio would be about 3.3. This is discussed again in reference to the experiments.

4.4 EXPERIMENTS

A small-deflection linear theory applied to the static buckling of cylindrical shells under end load is notoriously inadequate to predict experimental buckling loads except for very nearly perfect shells. Also, the shells ultimately buckle into a form very different from the buckling mode of the small-deflection theory. It is not obvious, then, that the simple linear theory given here should reasonably predict the large deflection dynamic buckling of such a shell. It was thought however, that the small-deflection theory would give promise for the dynamic problem because, once started in the linear theory pattern, the shell would continue to deform in this pattern and not have time to convert to another pattern. The experiments described here were run simultaneously with the theoretical investigation to determine whether such a theory should be pursued at all.

Previous experimentors reported only the final shapes (diamond buckles) after very severe and prolonged buckling, and showed high-speed (about 15,000 frames/sec) motion pictures which were nevertheless at a speed too slow to show the early buckling process. In order to record the early motion, the present experimental arrangement, shown in Fig. 4.5, incorporated three unique features: (1) the shells were free at the end opposite the impact so that the compressive impact stress would have a duration (at the impacted end) of, at most, equal to the transit time $2L/c$ of the longitudinal stress wave up and down the shell. This allowed terminal observation of early permanent buckling not obliterated by later folding. (2) The impacted end was bonded with epoxy cement to a relatively massive inside ring, and to a thin outside ring to provide a clamped boundary to the shell. Without these rings severe crimping at the end rapidly lowered the thrust and made comparison to theory impossible. (3) The massive end ring was accelerated explosively so that the time and simultaneity of impact could be controlled to within about 2 microseconds. This allowed the use of a Beckman-Whitley framing camera running at 240,000 frames/sec, fast enough to see the details of early wave formation.

Test shells were made from 0.0027-inch-thick 5052-H19 aluminum sheet rolled to a three-inch diameter with a lapped seam held with cloth tape. The steel ring at the lower end of each shell served as the "impacting" mass and weighed 12 times the weight of the shell so that its change in velocity during the impact, and hence the change in impact stress, was small. The ring was accelerated by placing it on the heavy steel anvil bar and detonating a sheet explosive charge on the opposite end of the anvil. The explosive sent a steep-fronted shock

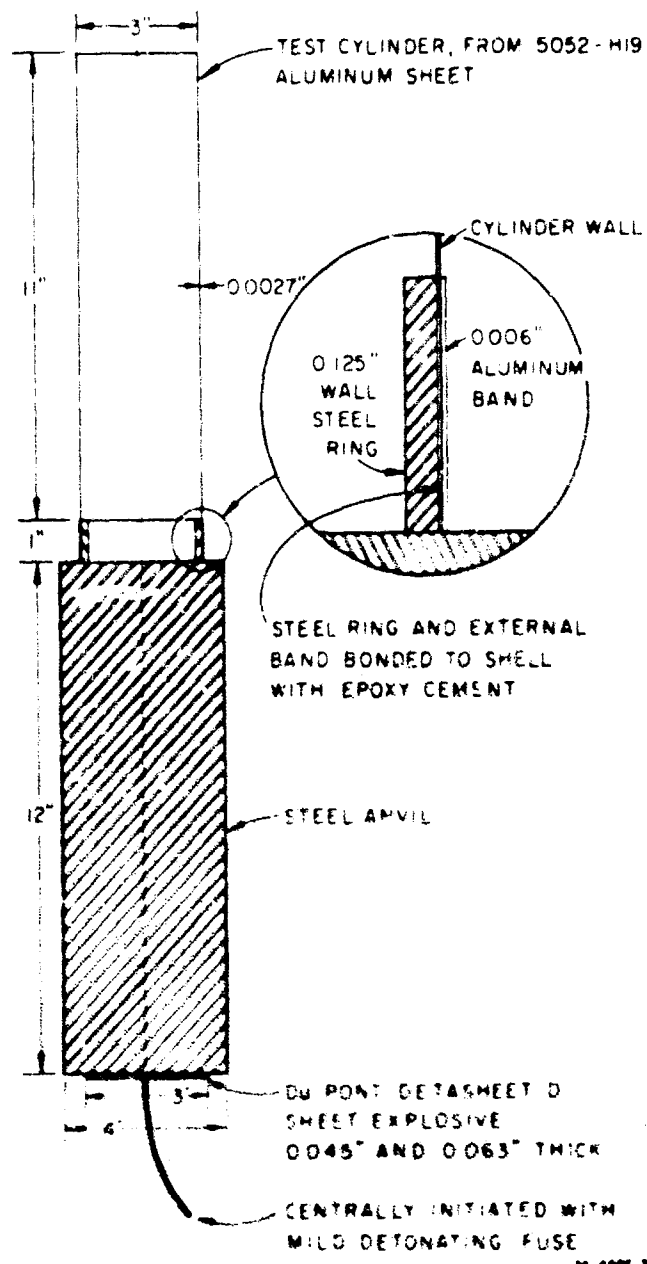


FIG. 4.5 EXPERIMENTAL ARRANGEMENT

into the anvil which entered the ring and bounced it off in much the same way as are the end pellets from a Hopkinson bar [4.10]. The pressure gradient behind the shock was sufficiently shallow that the reverberating stresses in the ring were small and it is assumed that the ring was stress-free when it "impacted" the cylinder. To insure good transmission of the shock from the anvil to the ring, the contact surfaces were lapped.

The ring velocity from various thicknesses of sheet explosive was determined in a separate series of experiments. Since the ring is very massive compared to the shell, the impact stress in the shell is assumed to be $\rho c v$, where ρc is the acoustic impedance of aluminum shell, and v is the velocity of the steel ring. The axial strain corresponding to this stress is

$$\epsilon = \frac{\rho c v}{E} = \frac{v}{c}$$

where c is the axial wave speed in the shell.

Figure 4.6 shows a sequence of framing camera pictures taken in an experiment in which $v = 340$ in/sec which, with $c = 200,000$ in/sec, gives $\epsilon = 0.0017$. Substituting $a/h = 1.50/0.0027 = 555$ into (4.11) yields $\epsilon_{cl} = 0.00109$ so that $\epsilon/\epsilon_{cl} = 1.56$. Thus, the impact stress is 1.56 times the classical static buckling stress. Only alternate frames from the original record are shown, giving 8.33 μ sec between frames and an exposure time of about 1.4 μ sec. Normalized time τ can be computed from (4.3) which yields $\tau = (c\epsilon/r)t = 0.38t$. On the original record, very tiny displacements could be discerned at $t = 7$ μ sec ($\tau = 2.6$). At $t = 11.2$ μ sec ($\tau = 4.2$) in Fig. 4.6, small wrinkles near the bottom of the shell are clearly visible. By $t = 27.8$ μ sec ($\tau = 10.6$) these wrinkles

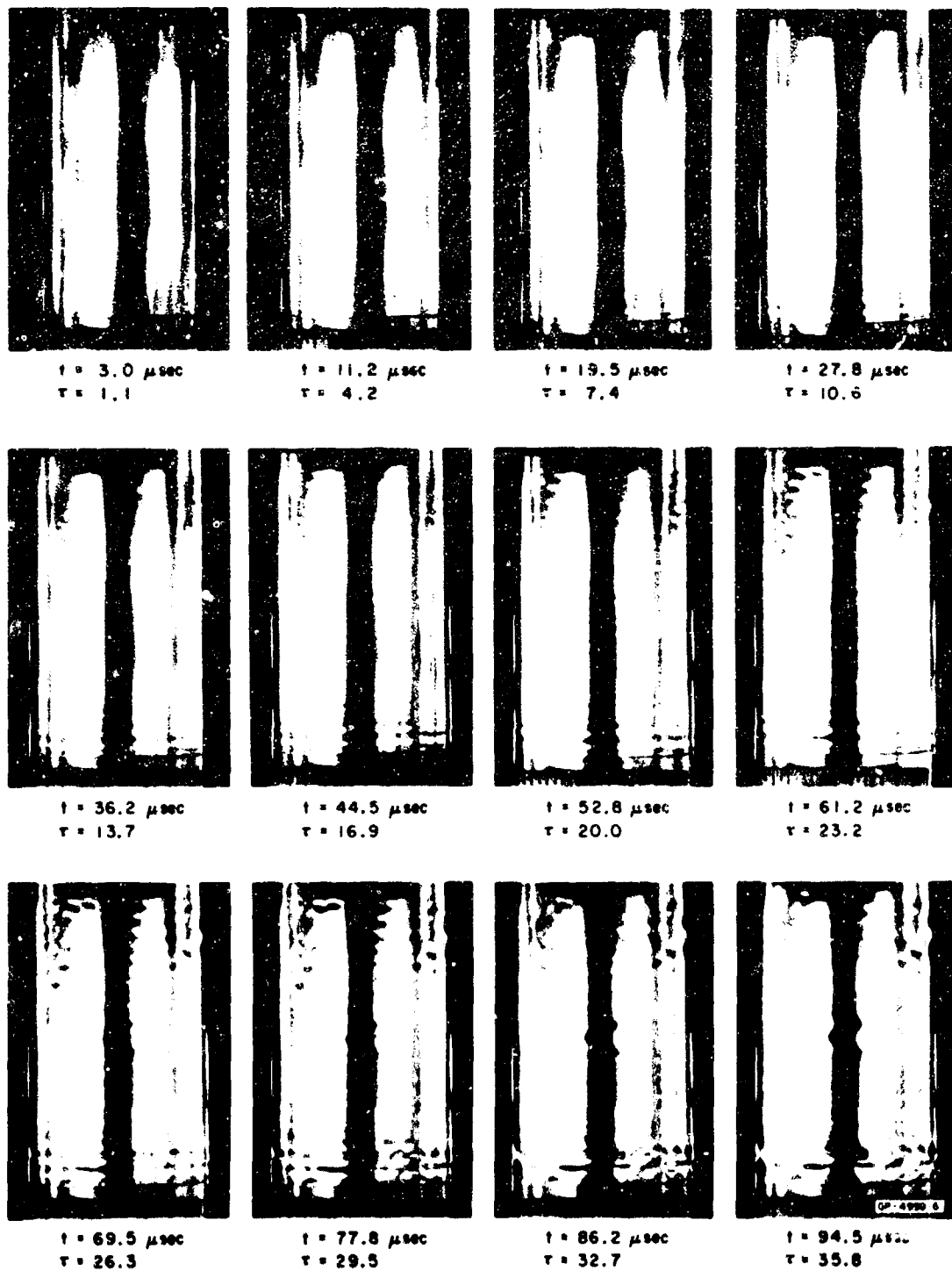


FIG. 4.6 AXIALLY IMPACTED CYLINDRICAL SHELL
Time is from initial impact at lower end

are definitely taking on the diamond pattern, indicating that nonlinear effects are predominating. Thus, from $\tau = 2.6$ to $\tau = 10.6$ the displacements grow from being just visible to amplitudes so large that nonlinear effects dominate. This agrees very well with the period of first rapid growth given by the theory. From Fig. 4.3 at $\sigma/\sigma_{cl} = 1.5$ we see that the amplification grows from $g_{\max} = 3$ at $\tau = 2.6$ to $g_{\max} = 100$ at $\tau = 10.6$. It is probable, as discussed later, that nonlinear effects begin to dominate at an intermediate time of about $\tau = 7$.

At frame $t = 27.8 \mu\text{sec}$, the beginning of buckling farther up the shell is evident. In the following frames these buckles stay fixed in position and grow in amplitude. Other buckles appear at areas in between, at which initial imperfections were probably smaller. The tiny ripples just above the buckles at the lower end characteristically appeared in all of the experiments. These are most visible at $t = 44.5 \mu\text{sec}$.

To compare the wavelengths in Fig. 4.6 with theory, the expected value of the axial wavelength is determined by substituting $\lambda_{\xi} = 8.9$ from Fig. 4.4 into (4.3), which yields

$$\lambda_x = \sqrt{\frac{D}{N}} \quad \lambda_{\xi} = \frac{r}{\sqrt{\epsilon}} \quad \lambda_{\xi} = 8.9 \frac{r}{\sqrt{\epsilon}}$$

Using $\epsilon = 0.0017$ and $h = 0.0027$ inch gives $\lambda_x = 0.18$ inch. From Fig. 4.6, the average length from 15 waves is $\lambda_x = 0.20$ inch, only 10% greater than the theoretical mean.

The permanent buckles remaining in several shells after impact are shown in Fig. 4.7. Figure 4.7(a) is of the same shell as in Fig. 4.6 and it is apparent that all but the lower few buckles in Fig. 4.6 were elastic. Most of the kinks away from the end in Fig. 4.7(a) were the result of difficulties in retrieving the shell (it was projected 12 feet into the air). In general, permanent buckles were confined to the area close to the impacted end as seen in all the shells in Fig. 4.7. The most striking feature of these buckles is their very small size and large aspect ratio as compared to static buckles. For comparison, Fig. 4.8 shows a statically buckled shell of the same material, wall thickness and diameter



(a) $\sigma/\sigma_{cl} = 1.56$



(b) $\sigma/\sigma_{cl} = 1.56$



(c) $\sigma/\sigma_{cl} = 1.20$



(d) $\sigma/\sigma_{cl} = 1.20$

FIG. 4.7 PERMANENT BUCKLES FROM
AXIAL IMPACT (opposite end
was free)



FIG. 4.8 STATIC BUCKLING OF
ON IDENTICAL SHELL

as those in Figs. 4.6 and 4.7. The circumferential and axial wavelengths are about 1.3 inches, giving an aspect of unity. The dynamic buckles in Fig. 4.7 have a mean aspect ratio of 3.3 and axial wavelengths of only 0.18 inch. Several shells are shown to illustrate the wide range of aspect ratio observed. There is little doubt that the shape of the buckles was strongly influenced by large elastic and plastic deformations, but it is significant that the large aspect ratio is suggested by the linear theory of the preceding sections.

Circumferential wavelengths were measured from the permanent buckles in these and two other shells and the results are summarized in Fig. 4.9. Aspect ratio is plotted rather than wavelength to emphasize the difference between these buckled forms and static buckles. The values range from 2.2 to 7.1 with a mean of 3.3. These are much larger

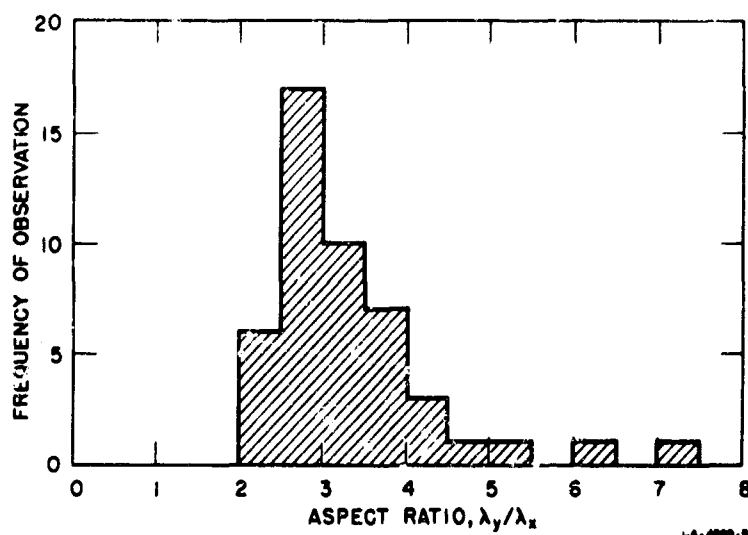


FIG. 4.9 HISTOGRAM OF OBSERVED ASPECT RATIOS

than the static ratio of about 1. It is difficult to compare these wavelengths with the linear theory because, as shown in Fig. 4.4, the theoretical wavelengths continually increase with time. However, from Fig. 4.4(b), the ratio of the theoretical average circumferential wavelength to the average axial wavelength is 3.3 at $\tau = 7$. Also, the photographs in Fig. 4.6 show that this is about the time at which the buckling amplitude becomes large.

This excellent agreement between theoretical and observed axial wavelengths, aspect ratios, and buckling times, confirms our original premise that early small deflection buckling dictates the pattern into which large deflection buckles form. If more details of the buckling are desired, displacements in the "preferred" wavelengths from the linear theory could be used as initial conditions in a large deflection theory. For calculating the threshold of buckling from axial impact, it may be sufficient to merely define some magnitude of the linear amplification function as indicative of buckling.

Crumpling of cylindrical shells used as an energy absorbing mechanism presents a much more complicated theoretical problem in which the final buckling may be in a mode much different from that observed here. This occurs because deformation in the very short axial wavelengths discussed here becomes so large that severe crumpling

occurs at one or both ends (the duration of the initial thrust is longest at one end because of the finite speed of axial propagation). This greatly reduces the thrust and subsequent buckling in the remainder of the shell probably occurs at a fluctuating thrust which depends on the buckling itself. An example of such buckling is given in Fig. 4.10.

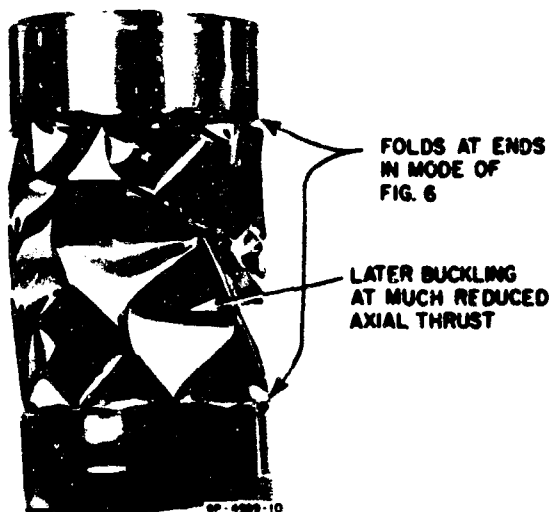


FIG. 4.10 BUCKLING WITH A HEAVY MASS
ON BOTH ENDS, $\sigma/\sigma_{cl} = 1.56$
AT INITIAL IMPACT

The impact velocity and shell parameters are the same as in Fig. 4.6, but now rigid masses are attached at both ends so that buckling proceeds for a longer time. Buckling away from the ends bears little resemblance to the impact buckling in Figs. 4.6 and 4.7, and in fact, is strikingly similar to the static buckling in Fig. 4.8. However, the crimping near each end in Fig. 4.10 is of the same form as the impact buckling in Figs. 4.6 and 4.7. Thus, the present theory predicts the early phase of buckling and suggests that away from the ends the transition to the final buckled state is very complex and can be studied only by including the interaction between the buckling and axial thrust.

REFERENCES

- 4.1 Coppa, A. P., "On the Mechanism of Buckling of a Circular Cylindrical Shell under Longitudinal Impact," General Electric Report R60SD494, presented at Tenth International Congress of Applied Mechanics, Stresa, Italy, Aug 31 - Sept 7, 1960.
- 4.2 Abrahamson, G. R. and J. N. Goodier, "Dynamic Plastic Flow Buckling of a Cylindrical Shell from Uniform Radial Impulse," Proceedings of the Fourth U.S. National Congress of Applied Mechanics, 1962, Vol. 2, pp. 939-950.
- 4.3 Lindberg, H. E., "Impact Buckling of a Thin Bar," West Coast Conference on Applied Mechanics, U. of Colorado, Boulder, Colorado, June 1964; to be published in Journal of Applied Mechanics.
- 4.4 Almroth, B. O., A. M. C. Holmes, and D. O. Brush, "An Experimental Study of the Buckling of Cylinders under Axial Compression," Experimental Mechanics, Vol. 4, No. 9, pp. 263-270, Sept 1964.
- 4.5 Coppa, A. P. and W. A. Nash, "Dynamic Buckling of Shell Structures Subject to Longitudinal Impact," General Electric Report ASD-TDR-62-774, prepared for Wright-Patterson Air Force Base, Dec 1962.
- 4.6 Roth, R. S. and J. M. Klosner, "Nonlinear Response of Cylindrical Shells with Initial Imperfections Subjected to Dynamic Axial Loads," AIAA Journal, Vol. 2, No. 10, pp. 1788-1794, Oct 1964.
- 4.7 Batdorf, S. B., "A Simplified Method of Elastic-Stability Analysis for Thin Cylindrical Shells," NACA Report No. 874, 1947.
- 4.8 Timoshenko, S. P. and J. M. Gere, Theory of Elastic Stability, McGraw-Hill Book Co., N.Y., pp. 457-468, 1961.
- 4.9 Rice, S. O., "Mathematical Analysis of Random Noise," in N. Wax, Selected Papers on Noise and Stochastic Processes, Dover Publications, Inc., New York, pp. 133-294, 1954.
- 4.10 Kolsky, H., Stress Waves in Solids, Dover Publications, Inc., New York, pp. 87-91, 1963.

APWL-TR-65-136

This page intentionally left blank.

5. DYNAMIC BUCKLING OF A CYLINDRICAL SHELL OF A STRAIN-RATE SENSITIVE MATERIAL

5.1 INTRODUCTION

In this section the dynamic flow buckling of a cylinder subjected to a uniform inward radial impulse for the case of a material which does not exhibit strain hardening but is strain-rate sensitive is investigated. Cylinders of fully annealed 1015 steel, a material known to be strain-rate sensitive [5.1, 5.2, 5.3, 5.4], were subjected to impulsive loads which produced final wrinkled forms similar to that shown in Fig. 5.1 with average wavelengths that were quite reproducible.

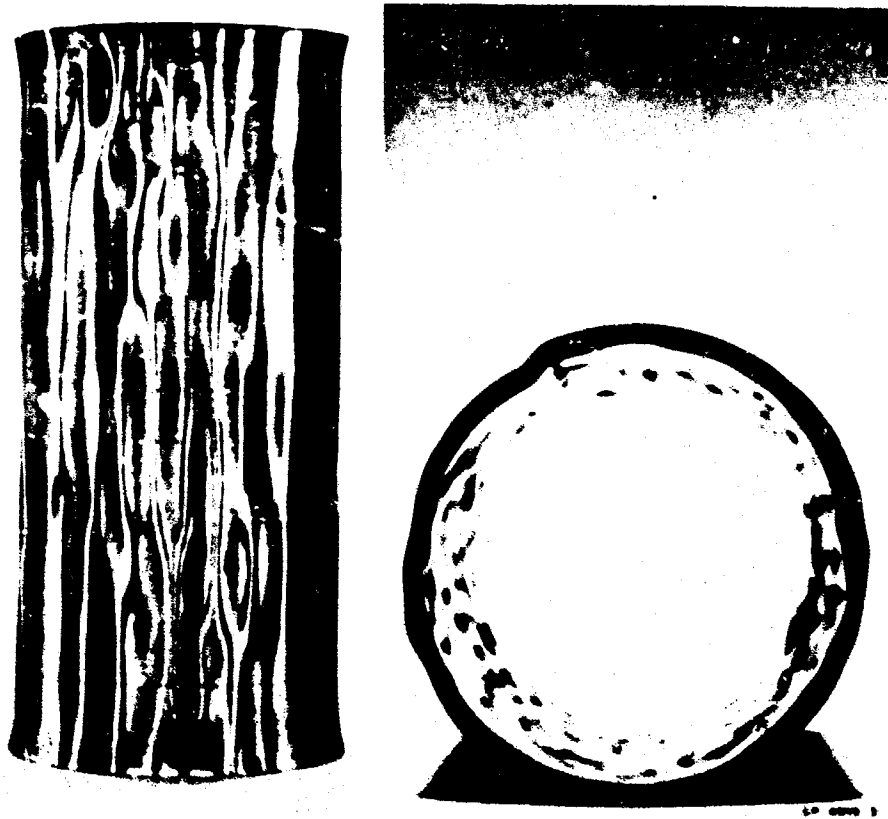


FIG. 5.1 TYPICAL BUCKLED SHAPE OF CIRCULAR CYLINDRICAL SHELL
OF FULLY ANNEALED 1015 STEEL — CYLINDER NO. 16

These wavelengths are compared with the predictions of a theory of flow buckling which assumes that the material is linearly visco-plastic. The reasonably good correlation suggests that this behavior could account for the formation of the final buckled shape.

Abrahamson and Goodier [5.5] proposed a theory of the formation of the wrinkled shape based on the dynamics of a metal shell which deforms plastically with linear strain hardening. This latter property is crucial to the theory because without it divergent series result. Experimental and predicted numbers of waves were in good agreement. Goodier and McIvor [5.6] gave a similar theoretical treatment for a material which exhibited both linear strain hardening and linear strain-rate sensitivity. In particular, theoretical results are given for linear strain-rate dependency with no strain hardening (visco-plastic), which is the behavior assumed here. An outline of the derivation of the equations of motion and their solutions is given later.

5.2 DYNAMIC FLOW BUCKLING

When the elements of a perfect cylindrical shell simultaneously receive the same large initial inward radial velocity the material flows into a uniform cylindrical shell of smaller radius and thicker wall until the initial kinetic energy has been converted into plastic work. Inevitable small imperfections, such as in the uniformity of the initial velocity, cause perturbations from this uniform converging motion. Departures from the circular form are amplified by the action of the compressive circumferential stress. These departures are considered small enough to regard the compressive circumferential strain as increasing throughout the motion. Thus at two points A and B, on the outside and inside respectively, as shown in Fig. 5.2, the circumferential strain increases but more rapidly at B than A due to the slight curvature perturbation.

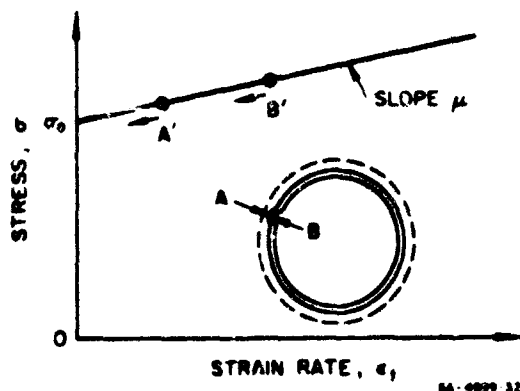


FIG. 5.2 IDEALIZED STRESS, STRAIN-RATE LAW

On the stress vs. strain-rate diagram in Fig. 5.2 the representative points A' and B' are both moving to the left with B' lagging behind A'. The strain-rate law is taken as

$$\sigma = \sigma_0 + \mu \epsilon_t \quad (5.1)$$

where σ and ϵ_t are the stress and the strain rate (subscripts t denote partial differentiation with respect to time) and μ is the slope of the straight line. Owing to the difference of circumferential stress between A' and B' there is a bending moment M in the section AB of the shell. For a unit axial length of cylinder regarded as a ring, integrating (5.1) over the cross section, with the assumption that plane sections remain plane, gives

$$M = \mu I \kappa_t, \quad I = h^3/12 \quad (5.2)$$

in which I is the second moment of area, h the wall thickness, and κ is the curvature. If the cylinder radius is a and the radial inward displacement is $w(\theta, t)$

$$\kappa = (w_{\theta\theta} + w)/a^2 \quad (5.3)$$

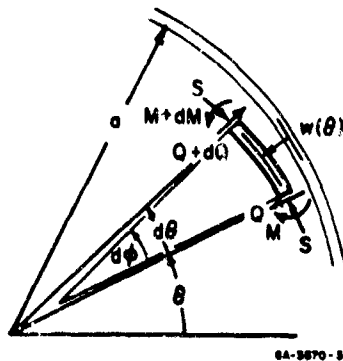
in which the subscripts θ denote partial differentiation with respect to the angular coordinate θ . The final inward displacement is considered small enough to allow the use of the initial values of the radius and thickness.

The lack of uniformity around the ring of the mean circumferential stress is neglected. Also, it is assumed that the slope μ

of the stress vs. strain-rate line is small so that the mean circumferential stress may be considered independent of time. Consequently, a constant circumferential force S is taken throughout the inward motion.

5.3 EQUATIONS OF MOTION

From Fig. 5.3, which shows an element of the ring with its attending forces and moments, the equations of equilibrium or motion (neglecting rotary inertia) may be written as



$$Q = M_{\lambda} \quad (5.4)$$

and

$$Q_{\lambda} + S\varphi_{\lambda} = -mw_{tt} \quad (5.5)$$

FIG. 5.3 NOTATION. ELEMENT OF SHELL IN MOTION

in which Q is the shear force, $d\lambda$ the arc element corresponding to $d\theta$ but now subtending an angle $d\varphi$, m the mass per unit run of circumference, and the subscripts denote partial differentiation. φ_{λ} is the curvature and is given by

$$\varphi_{\lambda} = 1/a + \kappa \quad (5.6)$$

Combining Eqs. (5.4) and (5.6) and performing the operations necessary to eliminate Q , M and κ yields the following equation for w :

$$\mu I (v_{\theta\theta\theta\theta} + w_{\theta\theta})_t / a^4 + S [1/a + (w_{\theta\theta} + w)/a^2] = -mw_{tt} \quad (5.7)$$

It is convenient to introduce the dimensionless displacement and time variables

$$u = w/a, \quad \tau = \mu I t / m a^4 \quad (5.8)$$

and the dimensionless constant

$$s^2 = Sma^6/\mu^2 I^2 = 144\sigma_0 \rho a^6/\mu^2 h^4 \quad (5.9)$$

where ρ is the cylinder material density.

Then (5.10) can be written in the form

$$u_{\tau\tau} + (u_{\theta\theta} + u)_{\theta\theta\tau} + s^2(u_{\theta\theta} + u) = -s^2 \quad (5.10)$$

5.4 SOLUTION

A particular solution u_p of (5.10) may be obtained by assuming that the dimensionless displacement is independent of θ . It represents the unperturbed motion and is a solution of the equation

$$u'' + s^2 u = -s^2 \quad (5.11)$$

where the primes denote differentiation with respect to τ .

Let V_0 be the initial impulsive velocity. Then $w_t(\theta, 0) = V_0$ and

$$u_\tau(\theta, 0) = V_0 ma^3/\mu I = v_0 \quad (5.12)$$

With the initial conditions $u_p(0) = 0$ and $u_p'(0) = v_0$ the solution of (5.11) is

$$u_p(\tau) = -1 + \cos s\tau + (v_0/s) \sin s\tau \quad (5.13)$$

This unperturbed motion ceases when $u_p'(\tau) = 0$. Hence its duration is given by the smallest root of

$$\tan s\tau = v_0/s \quad (5.14)$$

It is an approximation to the duration when slight wrinkling occurs since the plastic work done in shortening the circumference is not influenced to the first order by the slight wrinkling.

A slightly nonuniform initial velocity may be represented in the form

$$\begin{aligned} w_t(\theta, 0) &= V_0 \left[1 + \sum_{n=2}^{\infty} (\alpha_n \cos n\theta + \beta_n \sin n\theta) \right] \\ u_\tau(\theta, 0) &= V_0 \left[1 + \sum_{n=2}^{\infty} (\alpha_n \cos n\theta + \beta_n \sin n\theta) \right] \end{aligned} \quad (5.15)$$

Terms with $n=1$ are omitted since they do not contribute to the deformation of the circular shape.

The solution of the reduced form of (5.10) may be taken in the form

$$u = \sum_{n=2}^{\infty} [f_n(\tau) \cos n\theta + g_n(\tau) \sin n\theta] \quad (5.16)$$

where f_n must satisfy the equation

$$f_n'' + n^2(n^2 - 1)f_n' - (n^2 - 1)s^2 f_n = 0$$

The function g_n must satisfy the same differential equation.

The appropriate solutions for f_n and g_n are

$$f_n = B_n e^{\lambda_n^+ \tau} + C_n e^{\lambda_n^- \tau} \quad (5.17)$$

$$g_n = D_n e^{\lambda_n^+ \tau} + E_n e^{\lambda_n^- \tau} \quad (5.18)$$

where

$$\begin{aligned}\lambda_n^+ &= [n^2(n^2 - 1)/2] \left[(1 + 4s^2 / \left\{ n^4(n^2 - 1) \right\})^{1/2} - 1 \right] \\ \lambda_n^- &= [n^2(n^2 - 1)/2] \left[(1 + 4s^2 / \left\{ n^4(n^2 - 1) \right\})^{1/2} + 1 \right]\end{aligned}\quad (5.19)$$

The constants in (5.17) and (5.18) are obtained from the initial conditions $u(\theta, 0) = 0$ and $u_\tau(\theta, 0)$ given by (5.15). When the resulting functions f_n and g_n are substituted into (5.16) and the resulting complementary solution added to the particular solution (5.13) the final solution is

$$u = -1 + \cos s\tau + (v_0/s)\sin s\tau + v_0 \sum_{n=2}^{\infty} A_n(\tau)(\alpha_n \cos n\theta + \beta_n \sin n\theta) \quad (5.20)$$

where

$$A_n(\tau) = (e^{\lambda_n^- \tau} - e^{\lambda_n^+ \tau}) / (\lambda_n^- - \lambda_n^+) \quad (5.21)$$

λ_n^- and λ_n^+ being given by (5.19).

From a comparison of the expressions (5.15) and (5.20) it can be seen that $A_n(\tau)$ may be considered as an amplification factor which depends on the harmonic and time. Knowing $A_n(\tau)$ determines the effect of the initial velocity perturbations on the motion. One important property of the amplification factor is that it tends to zero as n increases. In fact for n large enough $A_n \sim 1/n^4$. This ensures the convergence of the series representation (5.20) and shows that the higher harmonics in the velocity perturbation will have little influence on the final wrinkled state.

5.5 STRAIN REVERSAL

The foregoing theory is valid until strain reversal begins. For points on the outside and inside surfaces the circumferential

compressive strain is

$$(1 - h/2a)(w/a - hw_{\theta\theta}/2a^2) \text{ and } (1 + h/2a)(w/a + hw_{\theta\theta}/2a^2)$$

and strain reversal begins when one of these reaches a maximum positive value and then decreases. When this occurs the strain rate at the inner or outer fiber is zero. The second factors in the above expressions, in dimensionless terms, are $u + hu_{\theta\theta}/2a$, and from (5.20) are representable in the form

$$\begin{aligned} u + hu_{\theta\theta}/2a = & -1 + \cos \tau (v_o/s) \sin \tau \\ & + v_o \sum_{n=2}^{\infty} (1 \pm \frac{h}{2a} n^2) A_n(\tau) \cdot (\alpha_n \cos n\theta + \beta_n \sin n\theta) \end{aligned} \quad (5.22)$$

the strain history is thus determined by (5.22).

5.6 RANDOM VELOCITY PERTURBATIONS

From (5.15) the perturbation of the initial velocity is

$$\tilde{u}_\tau(\theta, 0) = \sum_{n=2}^{\infty} (a_n \cos n\theta + b_n \sin n\theta) = \sum_{n=2}^{\infty} c_n \cos(n\theta - \theta_n) \quad (5.23)$$

where

$$a_n = v_o \alpha_n, \quad b_n = v_o \beta_n, \quad \text{and} \quad c_n^2 = v_o^2 (\alpha_n^2 + \beta_n^2)$$

It can be seen from (5.20) that if $\tilde{u}_\tau(\theta, 0)$ is given, the final wrinkled shape is known. With a statistical approach, Lindberg [5.7, 5.8] demonstrated that, in the case of the impact buckling of thin bars and cylinders, the assumption of imperfections in the initial displacements of the white noise type (displacements composed of harmonics of equal amplitude, random phase and with a uniform spectral density) led to

a good description of experimentally observed wavelengths. Here, a similar assumption will be made concerning the perturbation of the initial velocity. The random process will be considered stationary and ergodic. In order to bring out the analogy between the present problem and the relevant parts of the article of Rice [5.9] on random noise currents the following change of variable and substitutions are made in (5.23)

$$\theta = 2\pi\varphi/\varphi$$

where

$$0 \leq \varphi \leq \varphi, \quad f_n = n/\varphi \quad \text{and} \quad \omega_n = 2\pi f_n$$

then (5.23) becomes

$$\tilde{u}_\tau(\theta, 0) = \sum_{n=2}^{\infty} c_n \cos(\omega_n \varphi - \theta_n) \quad (5.24)$$

Now the kinetic energy associated with the perturbed initial velocity is

$$\frac{1}{2} m a \int_0^{2\pi} \tilde{u}_\tau^2(\theta) d\theta = \frac{1}{2} (2\pi a m) \frac{1}{\varphi} \int_0^{\varphi} \tilde{u}_\tau^2(\varphi) d\varphi = \frac{1}{2} (2\pi a m) \frac{1}{2} \sum_{n=1}^{\infty} c_n^2$$

and that associated with the n -th component is proportional to $c_n^2/2$.

Defining $w(f_n)$ as a kinetic energy density (power spectral density) it follows that $w(f_n)\Delta f = c_n^2/2$ where Δf is the "bandwidth" associated with the n -th component of \tilde{u}_τ so that

$$\Delta f = f_{n+1} - f_n = 1/\varphi$$

For a white noise velocity perturbation $c_n = c$, a constant, and the kinetic energy density is uniform at $w(f_n) = c^2 \varphi/2$. Also the phase angles θ_n in (5.24) are randomly distributed between 0 and 2π .

It follows from (5.20) that the perturbed deformation is

$$\tilde{u}(\theta, \tau) = c \sum_{n=1}^N \frac{A_n(\tau)}{2} \cos(\omega_n \varphi - \theta_n) \quad (5.25)$$

where N is large enough to consider A_n negligible ($A_n \sim 1/n^4$ for large n and shows a behavior analogous to a filter).

Applying now the theorem of Rice [5.9] for the expected number of zeros per unit angle φ and converting this to the number of waves N_λ for θ in $(0, 2\pi)$ gives

$$N_\lambda = \left[\frac{\int_0^\infty n^2 A_n^2 d_n}{\int_0^\infty A_n^2 d_n} \right]^{1/2} \quad (5.26)$$

5.7 NUMERICAL ANALYSIS AND EXPERIMENTAL RESULTS

Figure 5.4 is a stress-strain diagram obtained from a static tensile test on one of several specimens of fully annealed 1015 steel which were cut from cylinders. It demonstrates the lack of strain hardening below about 3 percent strain. According to the experimental results of Manjoine [5.1] the material is extremely sensitive to the rate of strain; both the length of the horizontal or ideally plastic portion of the stress-strain curve and the yield stress increase with strain rate. Based on these results an empirical relation between yield stress σ and strain-rate ϵ_t has been suggested by Symonds and Bodner [5.9] in the form

$$\sigma/\sigma_y = 1 + (\epsilon_t/D)^{1/p} \quad (5.27)$$

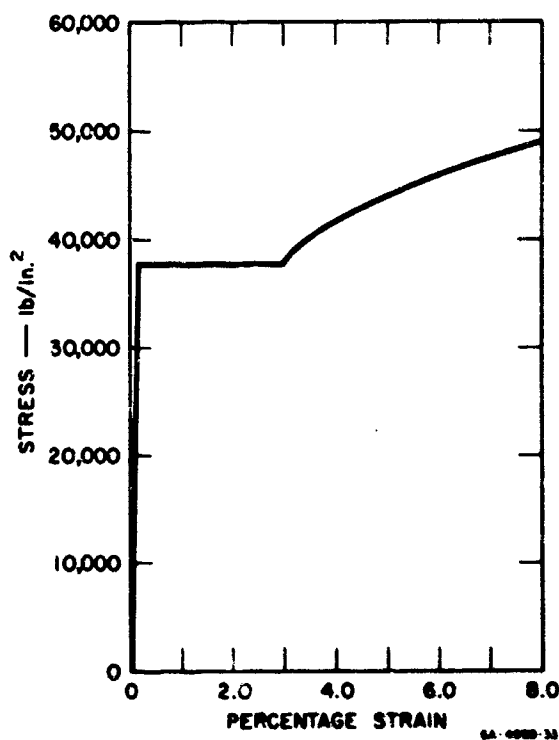


FIG. 5.4 STATIC STRESS-STRAIN DIAGRAM
FOR FULLY ANNEALED
1015 STEEL

where σ_y is the static yield stress, and p and D are empirical constants. For mild steel these are taken as $\sigma_y = 30,000 \text{ lb/in}^2$, $p = 5$, and $D = 40.4 \text{ sec}^{-1}$.

The curve (5.27) is shown in Fig. 5.5. In the development of the theory the linear strain-rate law (5.1) was used and this is here taken as the equation of the tangent to the curve (5.27) at the point corresponding to the value of the initial strain-rate $\epsilon_t(0)$. An example of such a tangent is shown in Fig. 5.5.

The slope of the tangent is

$$\mu = \sigma_y / (pD^{1/p} \epsilon_t^{1-1/p}) \quad (5.28)$$

and the value of σ_0 is given by the point of intersection of the tangent with the axis $\epsilon_t = 0$.

All numerical cases correspond to experiments that are described later and the main results are listed in Table 5.1. The initial velocities V_0 are obtained from impulse calibration experiments for the explosive used in similar configurations. The sequence of operations for finding the predicted number of waves around the cylinder is as follows. From the value of V_0 the initial strain-rate $\epsilon_t(0) = V/a$ is found and hence from (5.27), (5.28), and (5.1), σ_0 and μ are found. Next, the dimensionless constants S and V_0 are determined by (5.9) and (5.12). Equation (5.14) can now be solved for τ which represents the duration of motion; then (5.8) gives the actual

approximate duration. The spectrum of the amplification factor $A_n(\tau)$ follows from (5.21). Finally, the expected number of waves N_λ is computed from (5.26).

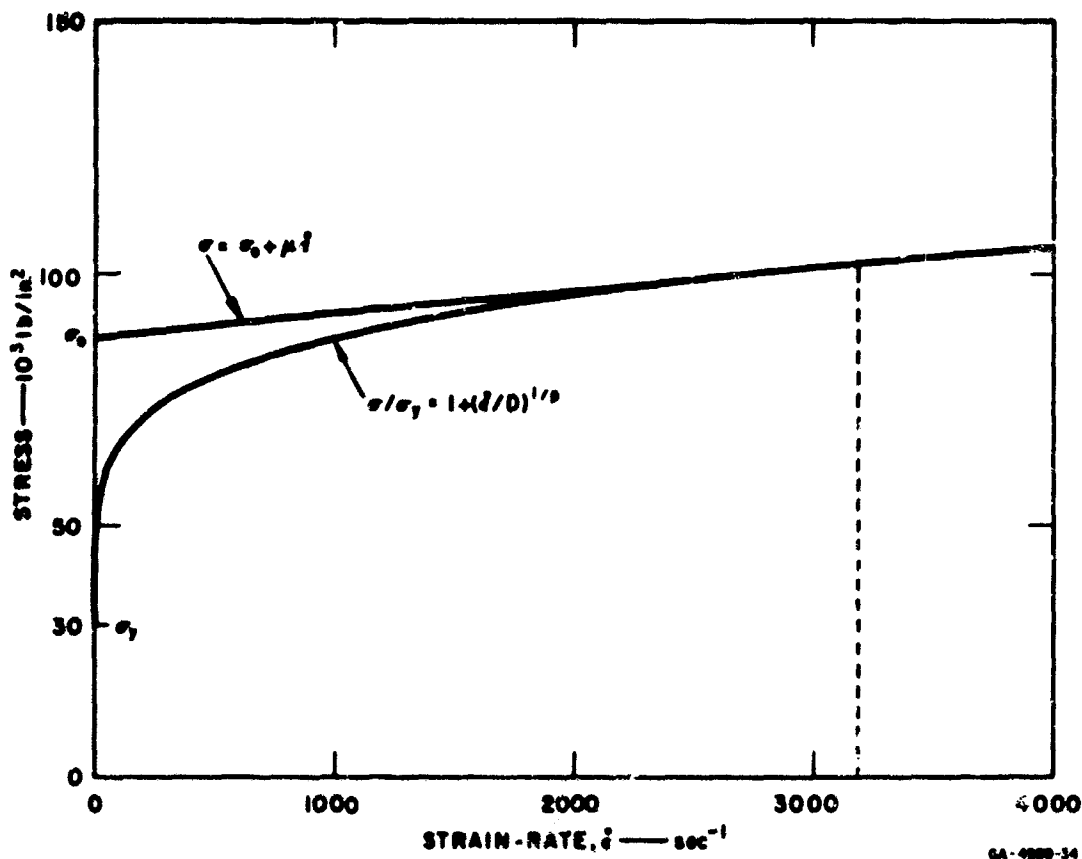


FIG. 5.5 STRAIN-RATE LAWS

Table 5.1 contains the values of n where A_n is a maximum at each quarter of the duration. It also contains the values of N_λ at these times. This is done to show the variation of the most amplified harmonic and the expected number of waves with time. In many cases the variation is not great. Figures 5.6 and 5.7 show the amplification spectra for the cylinders numbered 3a and 4a. For case 4a, it can be seen from Fig. 5.7 that there is a rapid growth of the amplification factors for harmonics about the value $n = 12$ and that above $n = 30$

Table 5.1
THEORETICAL AND EXPERIMENTAL RESULTS

Cylinder No.	Thickness h (in.)	Radius R (in.)	$\frac{A}{R}$	Initial Velocity V_0 (in/sec)	Initial Strain-Rate $\dot{\epsilon}(0)$ (sec ⁻¹)	σ_0^2 (lb/in ²)	μ (lb-sec/in ²)	Duration of Motion (msec)	Final Strain ($\times 10^{-5}$)	Theoret. Strain (%)	Exptim. Strain (%)	Most Amplified Harmonic — n				Expected No. of Waves — N_A				Exptim. N_A
												1/4	1/2	3/4	τ	1/4	1/2	3/4	τ	
1a	.042	1.494	35.6	4025	2694	85,593	5.2	49.2	1.024	6.9	9.9	21	25	27	27	22	25	27	28	26
1b				3450	2309	81,905	5.8	43.5	1.023	5.2	6.0	19	23	25	26	21	23	25	26	26
2a	.066	1.502	22.8	4574	3045	86,972	4.7	54.8	2.495	8.8	9.5	16	19	20	21	17	19	20	21	20
2b				4561	1704	80,734	7.4	34.2	2.479	3.0	4.4	10	13	15	16	15	15	15	16	23
2c				2196	1462	79,194	8.4	30.0	2.463	2.2	2.7	9	12	14	15	14	14	15	15	24
2d				2196	1462	79,194	8.4	30.0	2.463	2.2	2.7	9	12	14	15	14	14	14	15	23
3a	.089	1.488	16.7	4749	3191	87,508	4.5	56.0	4.621	9.4	9.3	12	15	16	17	14	15	16	17	13
3b				3528	2371	84,189	5.7	44.1	4.635	5.4	5.0	9	13	14	15	13	13	14	15	14
3c				2035	1368	78,544	8.9	27.9	4.548	1.9	1.5	6	8	10	11	12	11	11	11	16
3d				2707	1550	79,775	8.0	31.0	4.577	2.4	2.3	7	9	11	12	12	11	12	12	16
4a	.144	1.510	10.5	4780	3165	87,415	4.5	57.0	11.73	9.6	8.7	8	10	11	12	11	11	12	12	9
4b				2935	1944	82,079	6.7	38.6	11.73	3.8	4.3	5	7	8	9	10	9	9	10	9
4c				2180	1444	79,073	8.5	30.0	11.59	2.2	2.4	4	6	7	8	10	9	8	9	9
4d				2180	1444	79,073	8.5	30.0	11.59	2.2	2.4	4	6	7	8	10	9	8	9	9

Material: Fully annealed 10.5 steel
Mass Density = 0.000332 lb-sec²/in⁴

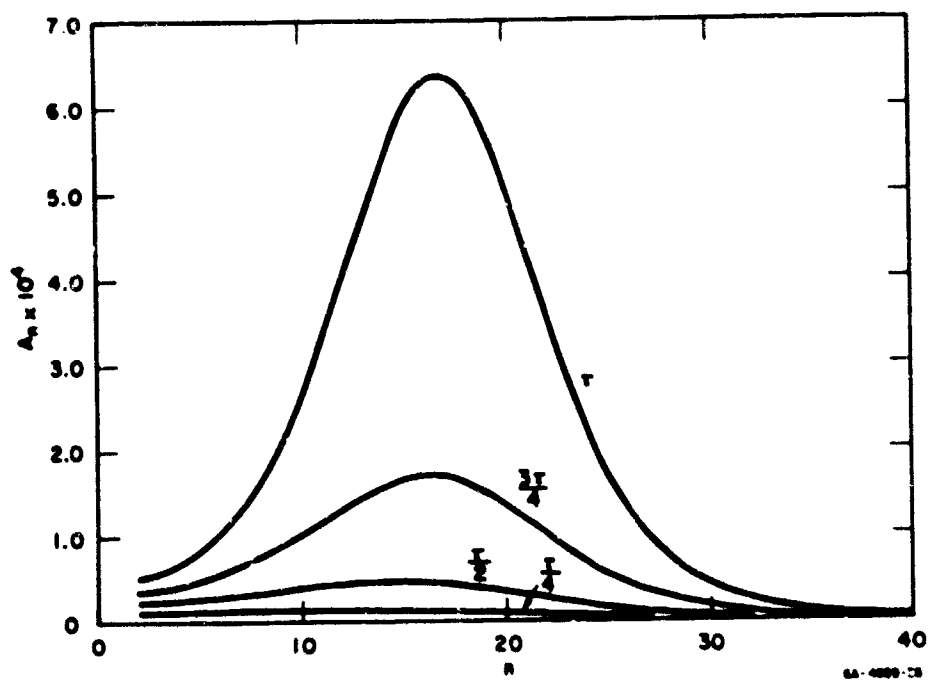


FIG. 5.6 AMPLIFICATION FUNCTION FOR CYLINDER 3a

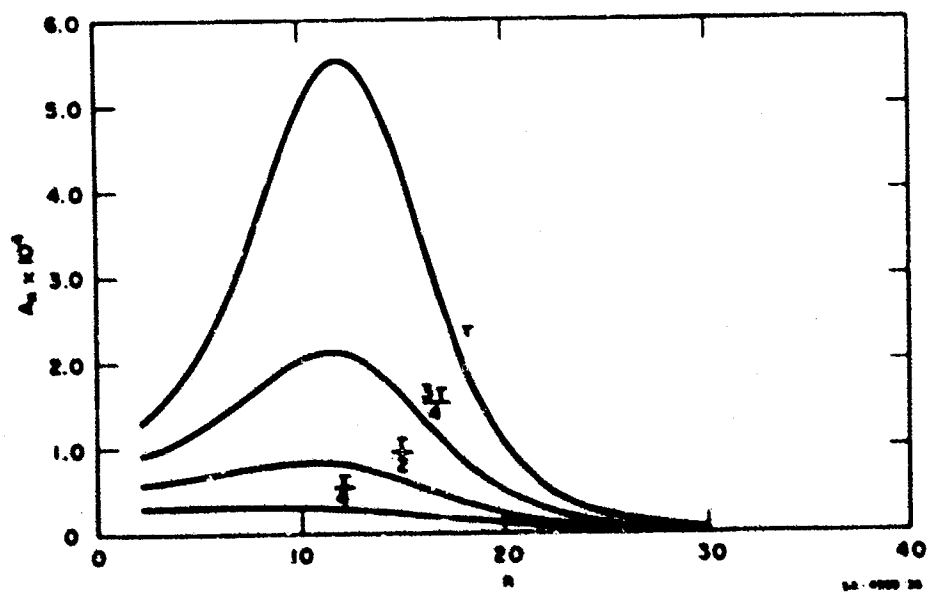


FIG. 5.7 AMPLIFICATION FUNCTION FOR CYLINDER 4a

virtually no amplification occurs ($A_n \sim 1/n^4$ for large n). During the final three-quarters of the duration of motion the values of n at peak A_n move from $n = 8$ to $n = 12$ while the expected number of waves N_λ moves only from $N_\lambda = 12$ to $N_\lambda = 14$. The magnification factor curves of Figs. 5.6 and 5.7 are quite typical and similar shifts in the most amplified harmonic and expected number of waves occur as deformation proceeds.

Again for cases 3a and 4a random initial velocity perturbations were considered. In case 3a, the first 50 harmonics of constant amplitude c and random phase (white noise) were employed in (5.23) and the representation is shown in Fig. 5.8(a). The resulting perturbed

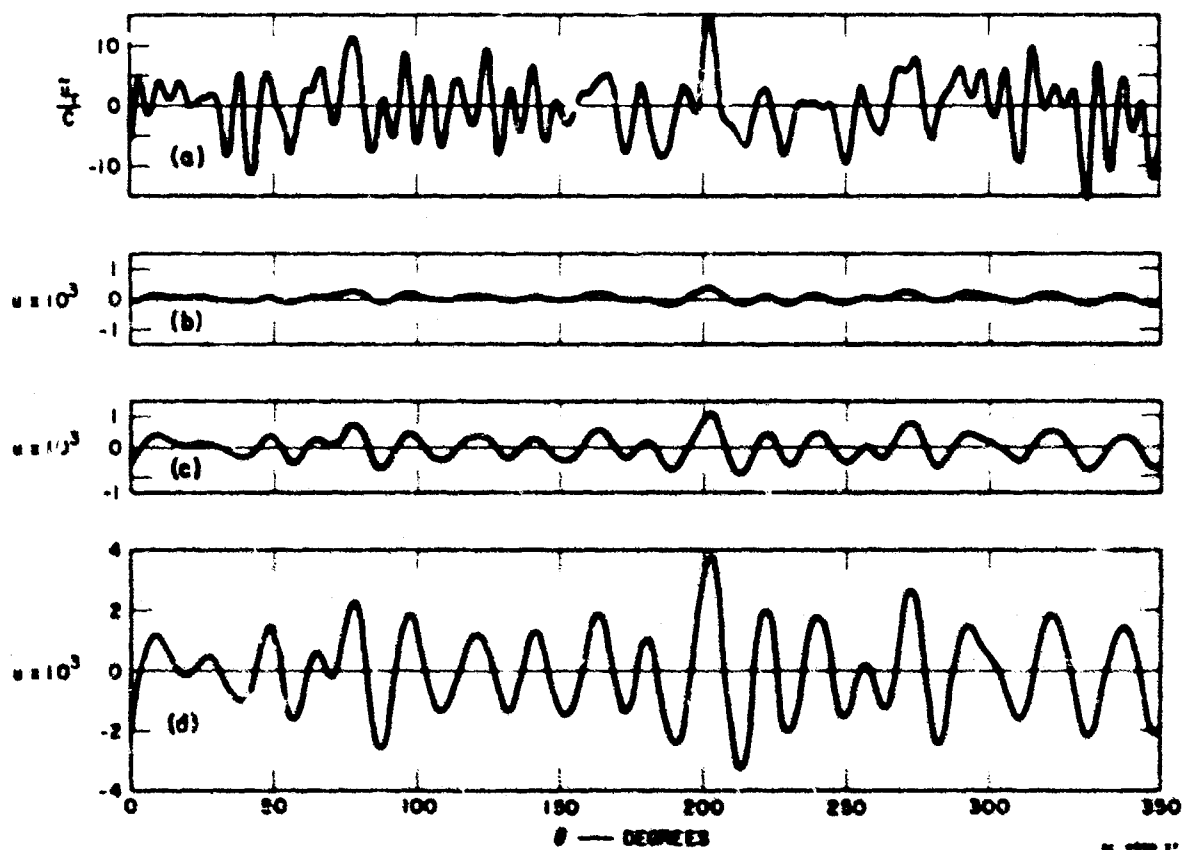


FIG. 5.8 RESPONSE OF CYLINDER 3a TO WHITE NOISE VELOCITY PERTURBATIONS
(a) Initial velocity perturbation, (b) Buckled form after 28 μ sec, (c) Buckled form after 42 μ sec, and (d) Buckled form after 56 μ sec

inward displacements in the form \tilde{u}/c were obtained from (5.25) at one-half, three-quarters, and at the whole of the duration of motion. They are shown in Figs. 5.8(b), (c), and (d), respectively and provide an illustration of the development of the buckled form. The higher harmonics in the initial velocity perturbation are filtered out because of the form of the spectrum of the amplification factor (Fig. 5.6). In the example of Fig. 5.8, a preferred wavelength exists corresponding to 18 waves around the cylinder, the expected number of waves if $N_\lambda = 14$, and one experiment gave 13 waves. For case 4a, Fig. 5.7(a) shows a perturbed initial velocity using the first 30 harmonics of equal amplitude and random phase. The development of the buckled form can be seen in Figs. 5.7(b), (c), and (d). The higher harmonics are filtered out, 15 waves develop around the cylinder, the expected number of waves is $N_\lambda = 14$, and the experimental number is 9 waves.

The amplitudes of the initial imperfections are considered small enough to avoid strain reversal. Experimental values for the number of waves comprise the right-hand column of Table 5.1 and can be compared with the expected number of waves of the most amplified harmonic, the former being more meaningful but the latter serving as an indicator. The degree of agreement lends credibility to the postulated mechanism, at least as a first-order description.

For cylinders 3a and 4a, Figs. 5.10 and 5.11 show the developed final shapes and can be compared with the predicted shapes of Figs. 5.8(d) and 5.9(d) respectively. Apart from the lower harmonics present in the experiments due to a slight lack of circularity of the cylinders the buckled forms are similar. For these two cylinder harmonic analyses (trigonometric interpolation) [5.10] of the experimental buckled forms were carried out and the results are shown in Figs. 5.12 and 5.13. The representation was taken in the form

$$u(\theta, \tau) = \sum_{n=0}^{\infty} c_n \cos(n\theta - \varphi_n)$$

with data recorded at every degree and the coefficients c_n plotted against n . The large coefficients for the lower harmonics are due to the initial lack of circularity of the cylinders. In case 3a peaks occur at $n = 6, 9, 11$, and 15 , and components above $n = 22$ are negligible. In case 4a peaks occur at $n = 7, 10$, and 13 , and components above $n = 16$ are negligible. No major conflict arises with the amplitude curves of Figs. 5.6 and 5.7.

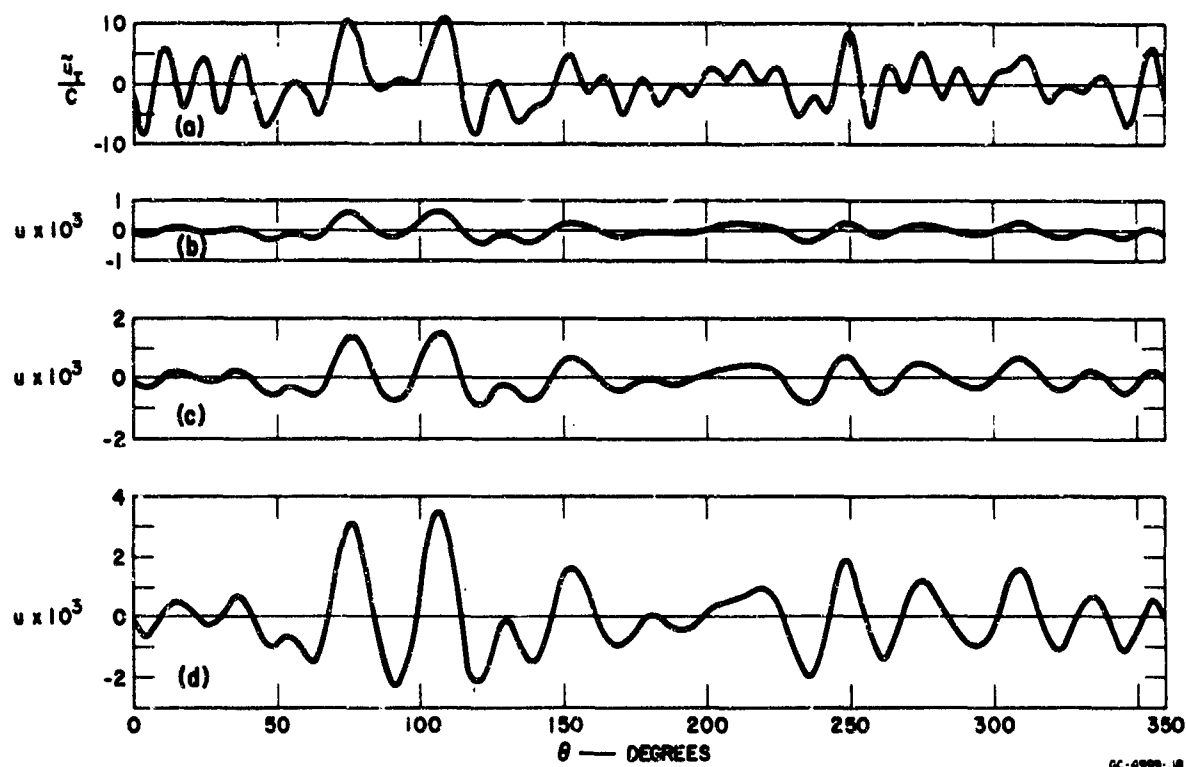


FIG. 5.9 RESPONSE OF CYLINDER 4a TO WHITE NOISE VELOCITY PERTURBATIONS (a) Initial velocity perturbation, (b) Buckled form after $28.5 \mu\text{sec}$, (c) Buckled form after $42.75 \mu\text{sec}$, and (d) Buckled form after $57 \mu\text{sec}$

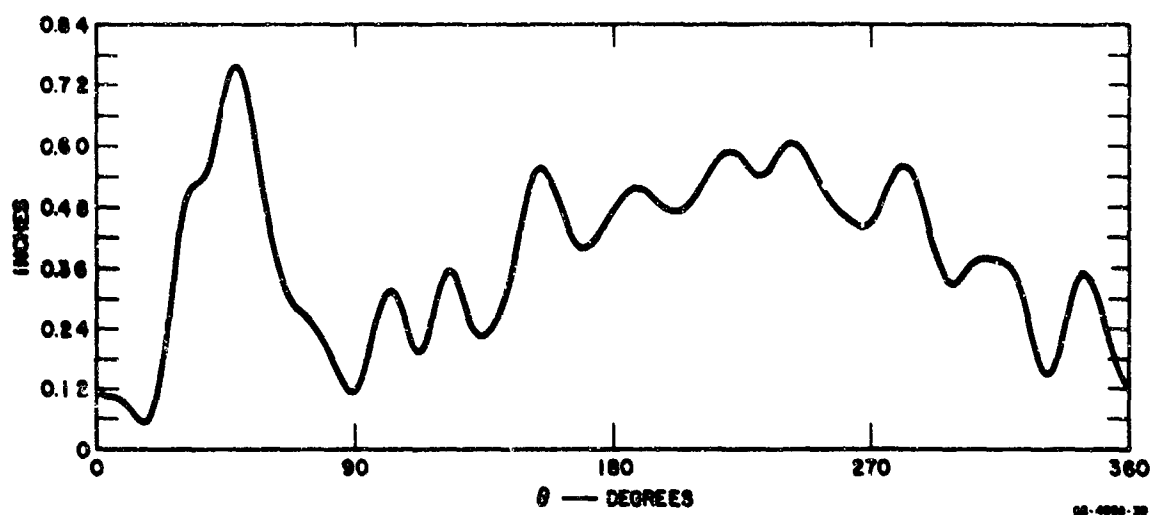


FIG. 5.10 BUCKLED FORM OF CYLINDER 3c

5.8 EXPERIMENTAL TECHNIQUES

The buckled cylinder of Fig. 5.1 was produced with the experimental arrangement shown in Fig. 5.14. Enclosing the cylinder is an attenuator of 1/4-inch-thick neoprene foam and a layer of explosive. The attenuator, which is necessary to prevent the cylinder from spalling, extends beyond the end of the cylinder to provide support for the explosive. The detonator starts from an electrical signal and is connected to the main charge by several strips of explosive. Detonation fronts initiated in the main charge by the strips of explosive expand from the initiation points and coalesce into a single ring-shaped detonation front in the "run-up" part of the main charge. The detonation front, which is of the order of a few mils wide, subsequently sweeps over the cylinder at a rate of 23,300 ft/sec.

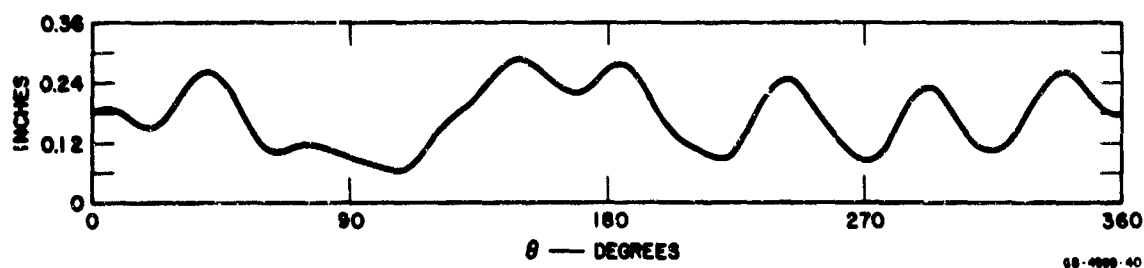


FIG. 5.11 BUCKLED FORM OF CYLINDER 4a

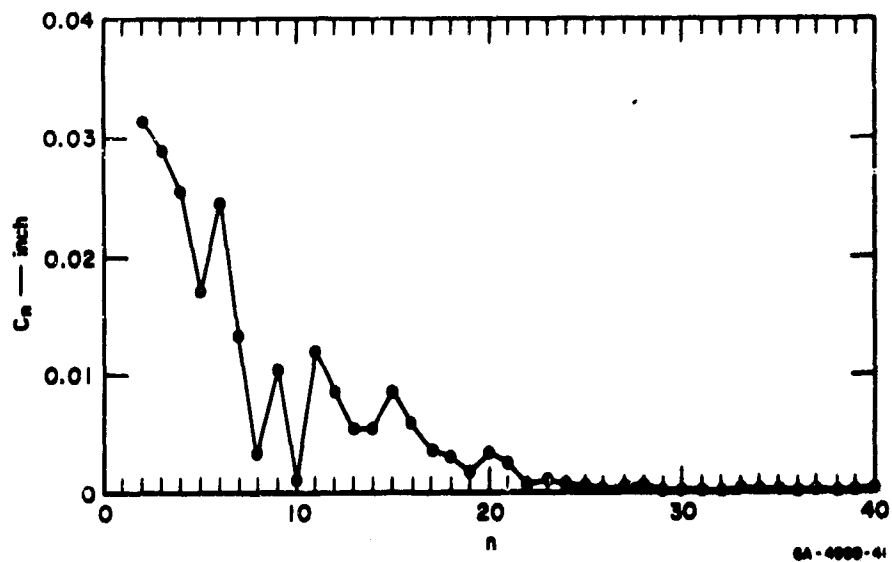


FIG. 5.12 RESULT OF HARMONIC ANALYSIS ON CYLINDER 3a

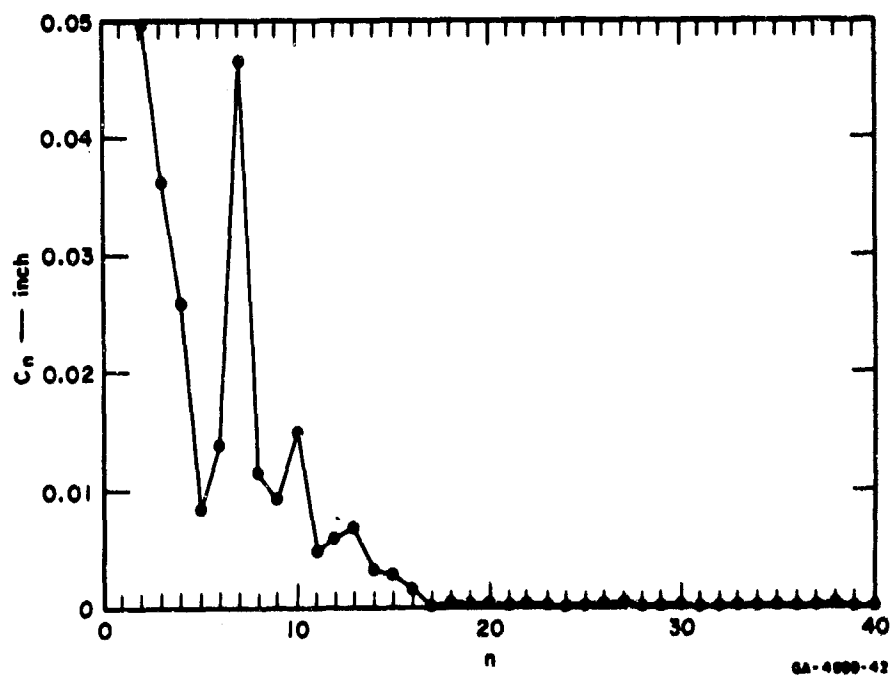


FIG. 5.13 RESULT OF HARMONIC ANALYSIS ON CYLINDER 4a

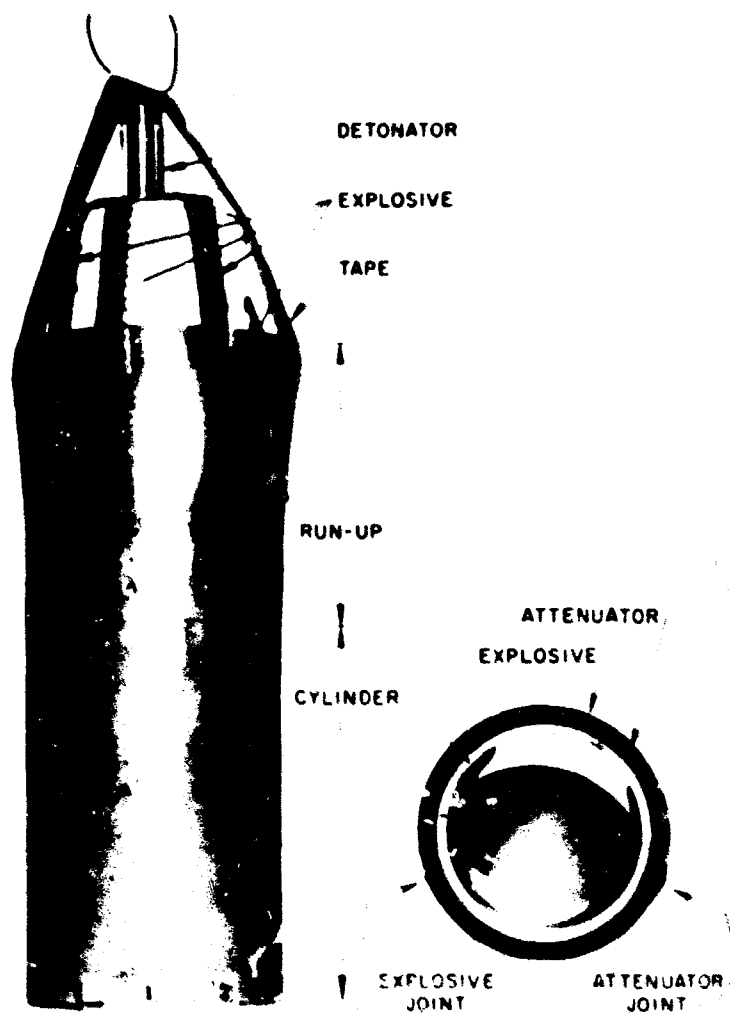


FIG. 5.14 EXPERIMENTAL ARRANGEMENT

A shock wave is induced in the attenuator by the detonation front and is transmitted from the attenuator to the cylinder, imparting an impulsive velocity V_0 (see Table 5.1).

Maximum variations in the thickness of the explosive are from 2 to 5 percent for charges from 12 to 57 mils thick, the larger variations going with the thinner charges. The variations in thickness are gradual except across joints. Variations in the thickness of the explosive and

the uncertainty in the impulse developed by the explosive combine to give an uncertainty of the order of 10 percent in the velocities imparted to the cylinders.

Table 5.1 gives the properties of the cylinders tested and the initial velocities V_0 were obtained by taking an impulse constant for the explosive-attenuator-target configuration of 2.4×10^5 dyne-sec/cm³.

5.9 CONCLUSIONS

In its present form the theory does a satisfactory job of predicting the buckled forms of cylinders of rate-sensitive material. There appear to be no major contradictions to the postulated mechanism of deformation although it would be desirable to have more experimental evidence and to look more thoroughly into other aspects of the problem such as the sensitivity of the solution to the strain-rate law and to the initial velocity, and strain reversal. The theory as it stands is somewhat idealized but seems adequately compensated by simplicity and usefulness.

REFERENCES

- 5.1 Manjoine, M. J., "Influence of Rate of Strain and Temperature on Yield Stresses in Mild Steel," J. Appl. Mech., Vol. 11, p. 211, 1944.
- 5.2 Campbell, J. D. and J. Duby, "The Yield Behavior of Mild Steel in Dynamic Compression," Proc. Roy. Soc. (London) A236, p. 24, 1956.
- 5.3 Campbell, J. D. and J. Harding, "The Effect of Grain Size, Rate of Strain, and Neutron Irradiation on the Tensile Strength of α -Iron," Response of Metals to High Velocity Deformation, Vol. 9, p. 51, Interscience Publishers. Edited by P. G. Shewmon and V. F. Zackay.
- 5.4 March, K. J. and J. D. Campbell, "The Effect of Strain Rate on the Post-Yield Flow of Mild Steel," J. Mech. and Phys. of Solids, Vol. 11, No. 1, p. 49, 1963.
- 5.5 Abrahamson, G. R. and J. N. Goodier, "Dynamic Plastic Flow Buckling of a Cylindrical Shell from Uniform Radial Impulse," Proc. of 4th U.S. National Congress on Applied Mechanics, Univ. of California, Berkeley, June 18, 1962.
- 5.6 Goodier, J. N. and I. K. McIvor, "Dynamic Stability and Non-linear Oscillations of Cylindrical Shells (Plane Strain), Subjected to Impulsive Pressure," Stanford University, Division of Engineering Mechanics Technical Report No. 132, June 1962, prepared under Office of Naval Research Contract Nonr 225(29) NR 064-241.
- 5.7 Lindberg, H. E., "Buckling of a Very Thin Cylindrical Shell Due to an Impulsive Pressure," J. Appl. Mech., Vol. 31, No. 2, p. 267, June 1964.
- 5.8 Lindberg, H. E., "Impact Buckling of a Thin Bar," J. Appl. Mech. Paper No. 64-APM-44.
- 5.9 Rice, S. O., Selected Papers on Noise and Stochastic Processes, Edited by N. Wax, p. 133, Dover Publications, Inc., New York, 1954.
- 5.10 Lanczos, C., Applied Analysis, Prentice Hall, Inc., Englewood Cliffs, N. J., 1956.

6. CORRELATION OF STRUCTURAL RESPONSE INFORMATION

6.1 INTRODUCTION

Over the past several years there have been many investigations of the failure of space-vehicle-type structures under suddenly applied external surface loads. It has been suggested that the results of these investigations be correlated to maximize their usefulness and indicate areas where further investigations are desirable.

The problem of correlating the results of structural response investigations has at least two aspects: (1) the development of a scheme for comparing the results, and (2) the incorporation of the results into the scheme. The following presentation is based on this division of the problem.

6.2 SCHEME FOR CORRELATING THE RESULTS OF STRUCTURAL RESPONSE INVESTIGATIONS

To facilitate the correlation of the results of structural response investigations it is highly desirable to have a simple and direct means of comparison. For static loads, results are usually summarized by giving the load magnitude which produces a critical stress, strain, or displacement in the structure. The same format appears suitable for dynamic loads.

Dynamic loads of the same spacial distribution and pulse shape (time variation) which produce the same critical stresses, strains, and/or displacements in a structure exhibit a simple relationship when plotted in the amplitude-impulse plane. Figure 6.1 illustrates the relationship between amplitude and impulse for rectangular pulses which produce the same maximum displacement of a linear oscillator. In the region where the curve approaches the vertical asymptote the load amplitude becomes unimportant and only the impulse is significant.

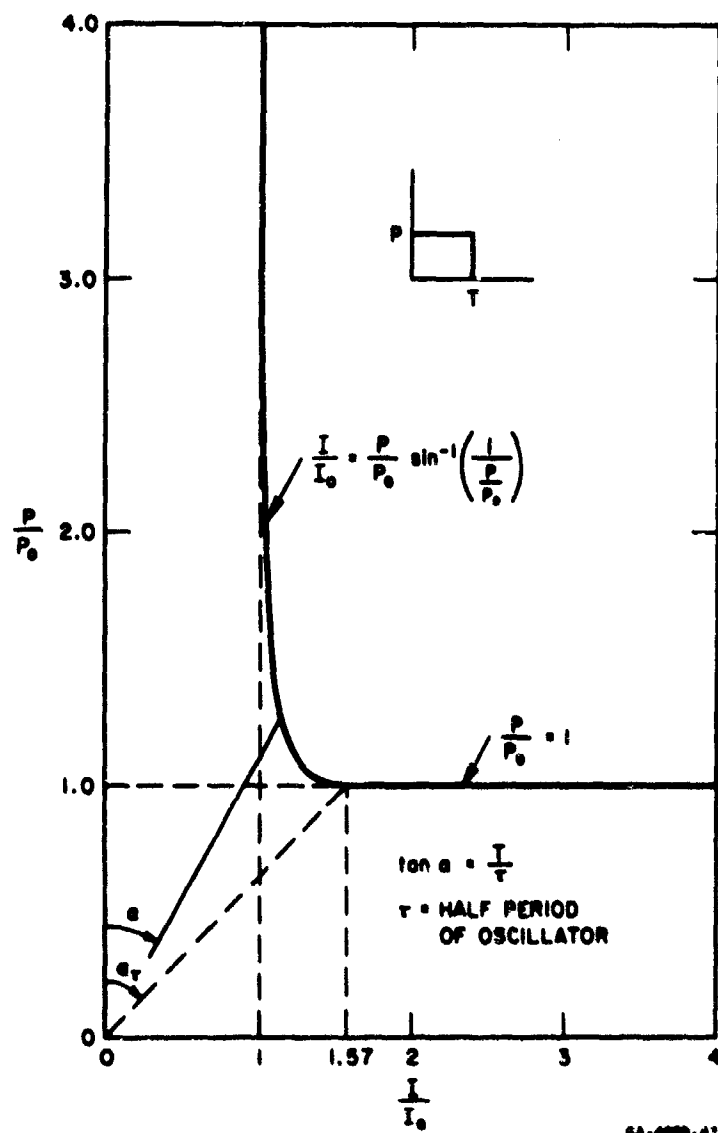


FIG. 6.1 AMPLITUDE-IMPULSE DIAGRAM FOR A LINEAR OSCILLATOR LOADED WITH A RECTANGULAR PULSE

In the region where the curve approaches the horizontal asymptote, the impulse becomes unimportant and only the amplitude is significant. In the intermediate region both amplitude and impulse are significant.*

Figure 6.2 shows the amplitude-impulse curves for rectangular and triangular pulses which produce the same displacement of a single-degree-of-freedom system of a rigid-plastic material. The curves have the same general shape as that of Fig. 6.1.

Tests of more complex systems such as cylindrical shells, which have a variation in response mode with load amplitude and impulse (for loads of the same spacial distribution and pulse shape), exhibit the same general relationship as that of Figs. 6.1 and 6.2 between the amplitude and impulse combinations which produce the same permanent displacement.

The response modes of the preceding examples are not sensitive to stress waves and are termed unitary modes. Loads which excite modes which are sensitive to stress waves, termed laminar modes, are also conveniently displayed in the amplitude-impulse plane.

* For a linear oscillator, the information given by the amplitude-impulse curve (Fig. 6.1) is related to that given by the shock spectrum [6.1]. For a load of given shape, the shock spectrum gives the response of a linear oscillator as a function of the frequency of the oscillator for a load of unit amplitude, while the amplitude-impulse diagram gives the amplitude and impulse combinations which evoke a given response from an oscillator of given frequency.

In a complex structure many modes are excited and a one-to-one correspondence between the amplitude-impulse diagram and the shock spectrum does not exist. For such structures, the amplitude-impulse diagram displays the loads which evoke a given peak response in the structure, including effects of all modes of deformation, even if the response is nonlinear and linear superposition is invalid. The shock spectrum gives the peak response of each mode, and in some cases (the response must be linear and the frequency spread must be limited) these can be superposed to determine an approximate peak response of the structure.

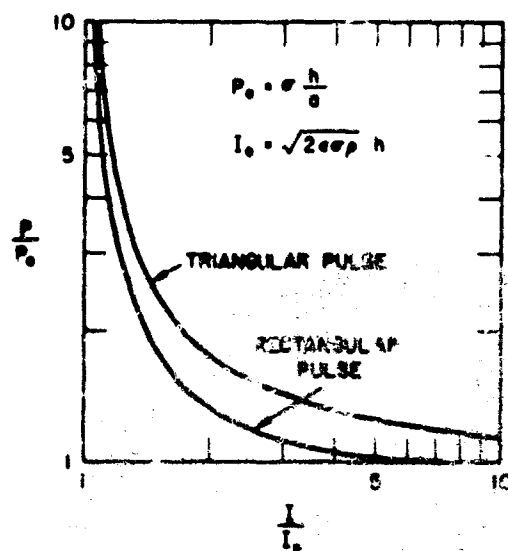


FIG. 6.2 AMPLITUDE-IMPULSE DIAGRAM FOR A ONE-DEGREE-OF-FREEDOM SYSTEM OF A RIGID PERFECTLY-PLASTIC MATERIAL. Here σ is yield stress, h is wall thickness, a is cylinder radius, ϵ is strain, and ρ is density.

Figure 6.3 shows schematically the amplitude-impulse diagram for the loads required to produce a given deformation of a thin cylindrical shell contained within a close-fitting sleeve which is loaded uniformly on the exterior. The impulse is constant (vertical part of curve) until the load duration exceeds twice the transit time through the inner shell. For monotonically decreasing pulses, at longer durations the amplitude decreases and approaches a limiting value.

Figure 6.4 shows the amplitude-impulse curve for uniform loads of rectangular shape required to produce cracking (from hoop tension) of a thin cylindrical shell by rebound from an internal mandrel. The jagged nature of the curve is due to peculiarities associated with the rapid decay of rectangular pulses.

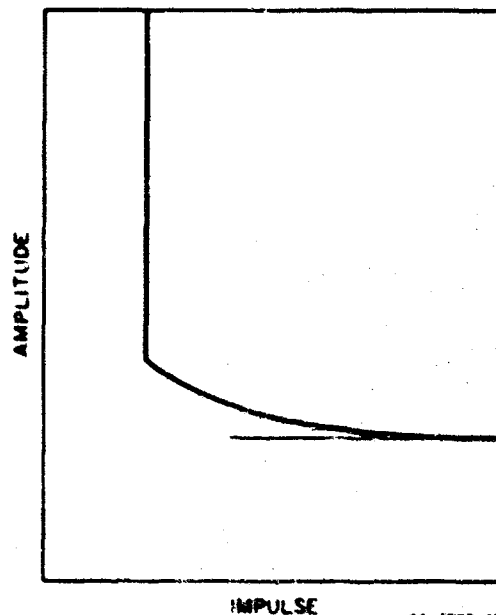


FIG. 6.3 SCHEMATIC AMPLITUDE-IMPULSE DIAGRAM FOR A THIN CYLINDRICAL SHELL CONTAINED WITHIN A CLOSE-FITTING SLEEVE LOADED ON THE EXTERIOR

From the foregoing, it appears that amplitude-impulse diagrams afford a convenient basis for comparison of the results of structural response investigations having the ultimate objective of predicting failure loads. A particularly desirable feature is that the asymptotes of the amplitude-impulse curves, which correspond to short-duration and long-duration loads, are generally the easiest part of the curves to establish theoretically and experimentally. Also, for most structures, the general shape of the curve will be similar to that of Figs. 6.1 to 6.4, and hence interpolation is simple. Another desirable feature is that amplitude and impulse are easily related to weapon yield and range.

With this approach, to completely describe the failure loads for a given structure with a given failure criteria requires a set of amplitude-impulse curves, one curve for each load distribution and pulse shape. Such a set of curves would appear to satisfy the needs of

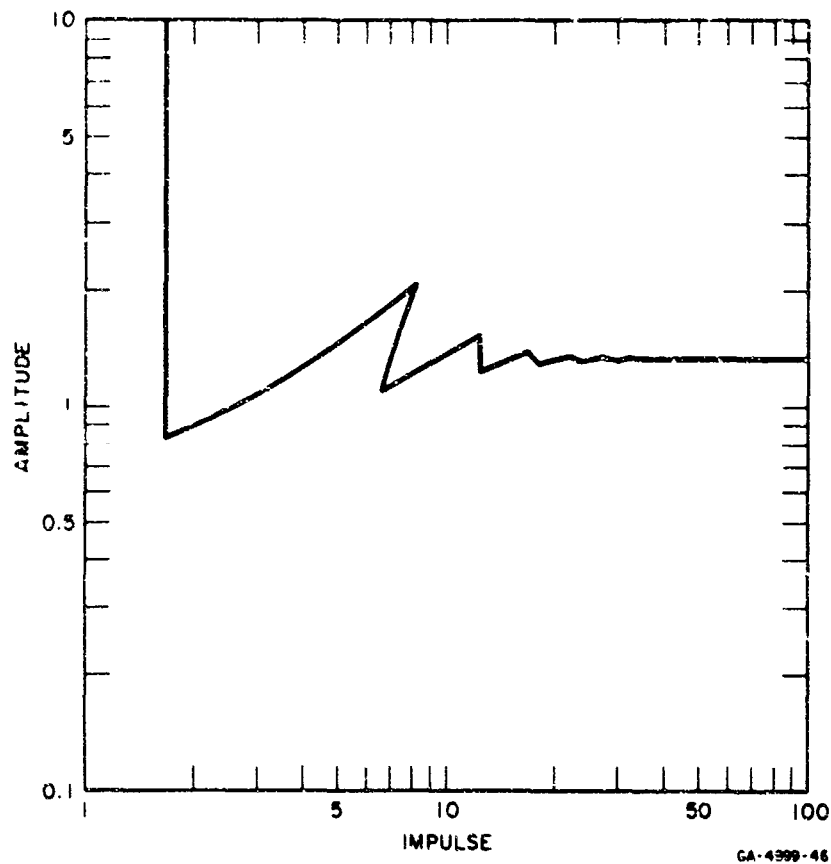


FIG. 6.4 SCHEMATIC AMPLITUDE-IMPULSE DIAGRAM FOR RECTANGULAR PULSES TO PRODUCE CRACKING (from hoop tension) OF A THIN CYLINDRICAL SHELL BY REBOUND FROM AN INTERNAL MANDREL

the designer, who must design structures to carry certain loads, and of the analyst, who must determine the failure loads of given structures.

6.3 CORRELATION OF THE RESULTS OF STRUCTURAL RESPONSE INVESTIGATIONS

Of the vast amount of structural response information available, only a very small part is relevant to the problem of determining failure loads of space-vehicle-type structures under suddenly applied external surface loads. Most of the available structural response information is for linear elastic systems and is of secondary importance

for the present application since, for the structures of greatest interest, failure generally involves significant permanent deformation. Moreover, of the available information on permanent deformation of structures, most is for static loads.

Information on permanent deformation of space-vehicle-type structures under suddenly applied external surface loads appears to stem from three main sources: (1) investigations of effects of air blasts on airplane structures, (2) investigations of the effects of underwater blasts on ship and submarine hulls, and (3) recent investigations on the effects of suddenly applied external surface loads on space-vehicle-type structures. The results of the investigations on aircraft are of some interest for lightweight satellites, but are of very limited use for the relatively thick-walled structures of re-entry vehicles. The results of investigations on ship and submarine hulls should provide significant information on re-entry vehicle structures. Unfortunately, this information has been inaccessible. Therefore, the following discussion is based on the recent investigations undertaken specifically to obtain additional information on the response of space-vehicle-type structures under suddenly applied external surface loads.

The basic structural element of space vehicles in general is the cylindrical shell, or conical shell of small angle. The first known attempt to determine bounds on a wide range of suddenly applied external surface loads which produce a given permanent deformation of a cylindrical shell is that described in [6.2], and was concerned with smoothly varying load distributions. The bounding curves found are shown in Fig. 6.5. The upper bound, shown for rectangular and triangular pulse shapes, are the loads which produce 10 percent deformation of a uniformly loaded cylindrical shell of a rigid-plastic material which responds in uniform radial motion (i.e., buckling is excluded). Since in this mode the maximum amount of energy is absorbed in plastic work per unit deformation, and no actual load could produce such an idealized response, this is an absolute upper bound on actual loads which produce the same deformation, for any cylindrical shell.

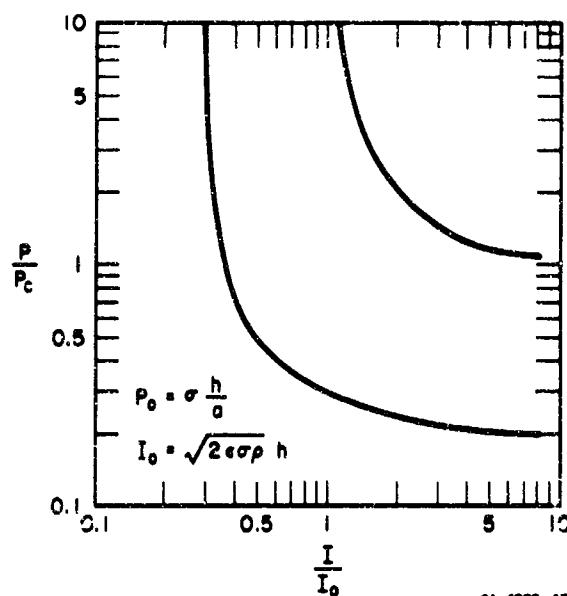


FIG. 6.5 BOUNDING CURVES ON SUDDENLY-APPLIED EXTERNAL SURFACE LOADS OF SMOOTHLY VARYING DISTRIBUTION TO PRODUCE 10 PERCENT DEFORMATION OF A CYLINDRICAL SHELL. (See Caption to Fig. 6.1 for definitions.)

The lower bound is based on limited experimental results [6.3], [6.6], and in view of the extensive effort being made to obtain additional information on failure loads of cylindrical shells, should be regarded as tentative.

The effort alluded to above is that being undertaken at SRI under Contract P. O. 24-14517 under AF 61(694)-655 with Lockheed Missiles and Space Company for the Air Force. This is a combined experimental and theoretical effort with the objective of establishing the amplitude-impulse curves for suddenly applied external surface loads of smoothly varying distribution which produce 10 percent deformation of monocoque cylindrical shells and multilayer cylindrical shells typical of space vehicles. The experiments thus far have shown that buckling is a predominant failure mechanism over the entire load range. The theory which is being developed is based on this mechanism. A report on this work is expected to be available in late 1965.

Except for the extensive experimental effort by BRL [6.6], the results of which were included in determining the lower bound shown in Fig. 6.5, the results of other investigations on cylinders have not yet been cast in the form of amplitude-impulse diagrams.

Other structural elements of interest for space vehicles are spherical shells, beams, and plates. For spherical caps, an upper bound can be obtained on the same basis as that for cylindrical shells. The resulting curve is given by Fig. 6.5 with $\rho_0 = 2\sigma h/a$ and $I_0 = \sqrt{4\epsilon\sigma\rho} h$. No data or theory are known which would establish a curve of load amplitude and impulse to produce a given permanent deformation of spherical shells.

In a recently submitted report [6.4], theoretical amplitude-impulse curves are presented for rigid-plastic beams and plates under a variety of boundary conditions and loads. However, the curves depart by factors of 3 to 10 from experimental results. Considerable more work is needed to refine the amplitude-impulse curves for beams and plates.

Amplitude-impulse curves for failure (in hoop tension) of a thin cylindrical shell by rebound from an internal sleeve for uniformly distributed pulses of rectangular form are given in [6.5]. This work will be extended in the near future for uniformly distributed pulses of triangular and exponential forms.

6.4 CONCLUSIONS

Amplitude-impulse diagrams appear to offer a meaningful and convenient way to represent dynamic failure loads. If this scheme is adopted, amplitude-impulse curves should be established for failure loads for all important structural elements of space vehicles.

Presently available theoretical and experimental information for establishing failure loads of space-vehicle-type structures is severely limited. Investigations now underway should significantly improve this situation.

REFERENCES

- 6.1 Fung, Y. C. and M. V. Barton, "Some Shock Spectra Characteristics and Uses," J. Appl. Mech. Paper No. 58-APM-5, presented at the West Coast Conference on Applied Mechanics, Los Angeles, Calif., September 8-10, 1958.
- 6.2 Abrahamson, G. R. and H. E. Lindberg, "Estimated Bounds on Suddenly Applied Surface Loads Required to Destroy Reentry Vehicles (U)," Journal of Missile Defense Research, Limited Distribution Supplement to Vol. II, No. 1, Summer 1964, JMDR-64-2S, (SRD).
- 6.3 Abrahamson, G. R., "On Suddenly Applied Surface Loads Required to Damage Re-Entry Vehicles (U)," Stanford Research Institute Interim Final Report, Contract No. AF 29(601)-6251, November 30, 1964, (SRD).
- 6.4 Florence, A. L., "Development of Long-Duration Explosive Loading Techniques and Response of Simple Structures to Pulse Loads," Stanford Research Institute Final Report, Contract AF 29(601)-6364, April 15, 1965.
- 6.5 Bungay, R. W., "Estimated Bounds on Suddenly Applied Loads Required to Damage the Heat Shield on a Hardened Re-Entry Vehicle (U)," Stanford Research Institute Semiannual Technical Summary Report No. 1, Contract No. AF 29(601)-6251, July 30, 1964, (SRD).
- 6.6 Schuman, W. J., Jr., "The Response of Cylindrical Shells to External Blast Loading," Ballistics Research Laboratory Memo Report No. 1461, March 1963.

7. OTHER INVESTIGATIONS

7.1 INTERACTION OF SHOCK EFFECTS AND STRUCTURAL EFFECTS

When a shell structure is exposed to an external impulsive surface load a shock wave is generated which propagates in from the exposed surface. If the load is sufficiently intense, the structure will be destroyed.

Two basic types of damage from impulsive surface loads have been identified; shock damage and structural damage. Shock damage is that due to stress wave interactions and generally occurs on the first or second transit of the stress wave through the wall of the structure, and, for common space vehicles, this is usually within a few micro-seconds after the application of the load. Structural damage is that due to the average velocity of the shell of the structure and generally occurs 50 μ sec or more after the application of the load, for common space vehicle structures.

In investigating the response of space vehicle structures to impulsive surface loads, it has become common practice to study shock effects and structural effects separately. This division is certainly valid for shock effects, which occur too early to be influenced by structural action. However, shock effects may influence structural effects.

The division of the response problem into shock effects and structural effects is based on the vastly different time scales of the two phenomena. Except for obvious interaction effects such as spalling, cracking, etc., this division assumes that the stress waves have subsided to insignificant amplitudes before structural deformation becomes significant.

For two-layered structures of nonmetallic heat shield and metal base structure, it has been shown [7.1] that for elastic stresses, about five wave transits through the layers is sufficient to attenuate the stress amplitude of the stress waves to about 20 percent or less of the initial amplitude. For common space vehicles, this requires less than 50 μ sec. Hence for such structures the separation of the response into shock effects and structural effects is valid.

The attenuation of stress waves in single-layer structures depends on details of the equation of state of the material. This was not investigated on the present contract.

7.2 PREDICTION OF ACCELERATIONS FROM SHOCK LOADING

Accelerations from suddenly applied surface loads can produce accelerations which damage internal components of space vehicles. It would be highly desirable to have a means of predicting the accelerations from a given load. However, experiments on a mocked-up satellite vehicle undertaken on Contract AF 29(601)-6435 indicate that internal accelerations are very sensitive to the local construction, so much so that it appears unlikely that a useful general method of predicting accelerations even for simple structures can be expected.

REFERENCES

- 7.1 Abrahamson, G. R. and W. Stuver, "Effects of Pulse-Spreading Countermeasures on Structural Response of Re-Entry Vehicles (U)," Stanford Research Institute Final Report, Contract AF 29 (601)-4745, February 28, 1964, (SRD).

Unclassified

Security Classification

DOCUMENT CONTROL DATA - R&D		
(Security classification of title, body of abstract and indexing annotation must be entered when the overall report is classified)		
1. ORIGINATING ACTIVITY (Corporate author) Stanford Research Institute Menlo Park, California		2a. REPORT SECURITY CLASSIFICATION Unclassified
		2b. GROUP
3. REPORT TITLE INVESTIGATION OF RESPONSE OF SIMPLIFIED ICBM-TYPE STRUCTURES TO IMPULSIVE LOADING		
4. DESCRIPTIVE NOTES (Type of report and inclusive dates) Final Report 16 March 1964 to 15 March 1965		
5. AUTHOR(S) (Last name, first name, initial) Abrahamson, G. R.; Florence, A. L.; Lindberg, H. E.		
6. REPORT DATE November 1966	7a. TOTAL NO. OF PAGES 126	7b. NO. OF REFS 37
8a. CONTRACT OR GRANT NO. AF29(601)-6360 b. PROJECT NO. 5710 c. Subtask No. 15.029 d.	8a. ORIGINATOR'S REPORT NUMBER(S) AFWL-TR-65-136 8b. OTHER REPORT NO(S) (Any other numbers that may be assigned this report) SRI Project GRU-4999	
10. AVAILABILITY/LIMITATION NOTICES This document is subject to special export controls and each transmittal to foreign governments or foreign nationals may be made only with prior approval of AFWL (WLRP), Kirtland AFB, N.M. 87117. Distribution of this document is limited because of the technology discussed.		
11. SUPPLEMENTARY NOTES	12. SPONSORING MILITARY ACTIVITY Air Force Weapons Laboratory (WLRP) Kirtland Air Force Base, New Mexico 87117	
13. ABSTRACT <p>Theoretical and experimental structural response investigations of space-vehicle-type structures under suddenly applied external surface loads are described. The simulation of a simultaneous impulsive load by a traveling load such as produced by an explosive is analyzed for the string and membrane. Three dynamic buckling problems are investigated: (1) dynamic plastic-flow buckling of flat plates due to in-plane flow, (2) dynamic elastic buckling of a thin cylindrical shell under axial impact, and (3) dynamic buckling of cylindrical shells of a strain-rate sensitive material. A scheme for correlating the results of structural response investigations concerned with dynamic failure loads of structures is presented and a brief review of available results is given.</p>		

DD FORM 1473

Unclassified

Security Classification

14 KEY WORDS	LINK A		LINK B		LINK C	
	ROLE	WT	ROLE	WT	ROLE	WT
Structural response Impulsive load Dynamic buckling						

INSTRUCTIONS

1. **ORIGINATING ACTIVITY:** Enter the name and address of the contractor, subcontractor, grantee, Department of Defense activity or other organization (corporate author) issuing the report.

2a. **REPORT SECURITY CLASSIFICATION:** Enter the overall security classification of the report. Indicate whether "Restricted Data" is included. Marking is to be in accordance with appropriate security regulations.

2b. **GROUP:** Automatic downgrading is specified in DoD Directive 5200.10 and Armed Forces Industrial Manual. Enter the group number. Also, when applicable, show that optional markings have been used for Group 3 and Group 4 as authorized.

3. **REPORT TITLE:** Enter the complete report title in all capital letters. Titles in all cases should be unclassified. If a meaningful title cannot be selected without classification, show title classification in all capitals in parentheses immediately following the title.

4. **DESCRIPTIVE NOTES:** If appropriate, enter the type of report, e.g., interim, progress, summary, annual, or final. Give the inclusive dates when a specific reporting period is covered.

5. **AUTHOR(S):** Enter the name(s) of author(s) as shown on or in the report. Enter last name, first name, middle initial. If military, show rank and branch of service. The name of the principal author is an absolute minimum requirement.

6. **REPORT DATE:** Enter the date of the report as day, month, year, or month, year. If more than one date appears on the report, use date of publication.

7a. **TOTAL NUMBER OF PAGES:** The total page count should follow normal pagination procedures, i.e., enter the number of pages containing information.

7b. **NUMBER OF REFERENCES:** Enter the total number of references cited in the report.

8a. **CONTRACT OR GRANT NUMBER:** If appropriate, enter the applicable number of the contract or grant under which the report was written.

8b, 8c, & 8d. **PROJECT NUMBER:** Enter the appropriate military department identification, such as project number, subproject number, system numbers, task number, etc.

9a. **ORIGINATOR'S REPORT NUMBER(S):** Enter the official report number by which the document will be identified and controlled by the originating activity. This number must be unique to this report.

9b. **OTHER REPORT NUMBER(S):** If the report has been assigned any other report numbers (either by the originator or by the sponsor), also enter this number(s).

10. **AVAILABILITY LIMITATION NOTICES:** Enter any limitations on further dissemination of the report, other than those

imposed by security classification, using standard statements such as:

- (1) "Qualified requesters may obtain copies of this report from DDC."
- (2) "Foreign announcement and dissemination of this report by DDC is not authorized."
- (3) "U. S. Government agencies may obtain copies of this report directly from DDC. Other qualified DDC users shall request through _____."
- (4) "U. S. military agencies may obtain copies of this report directly from DDC. Other qualified users shall request through _____."
- (5) "All distribution of this report is controlled. Qualified DDC users shall request through _____."

If the report has been furnished to the Office of Technical Services, Department of Commerce, for sale to the public, indicate this fact and enter the price, if known.

11. **SUPPLEMENTARY NOTES:** Use for additional explanatory notes.

12. **SPONSORING MILITARY ACTIVITY:** Enter the name of the departmental project office or laboratory sponsoring (paying for) the research and development. Include address.

13. **ABSTRACT:** Enter an abstract giving a brief and factual summary of the document indicative of the report, even though it may also appear elsewhere in the body of the technical report. If additional space is required, a continuation sheet shall be attached.

It is highly desirable that the abstract of classified reports be unclassified. Each paragraph of the abstract shall end with an indication of the military security classification of the information in the paragraph, represented as (TS), (S), (C), or (U).

There is no limitation on the length of the abstract. However, the suggested length is from 150 to 225 words.

14. **KEY WORDS:** Key words are technically meaningful terms or short phrases that characterize a report and may be used as index entries for cataloging the report. Key words must be selected so that no security classification is required. Identifiers, such as equipment model designation, trade name, military project code name, geographic location, may be used as key words but will be followed by an indication of technical content. The assignment of links, rules, and weights is optional.